Dissertation

Microstructural Modelling of Diffusional Creep in Polycrystals

Dipl.-Ing. Cornelia Pein

Institute for Materials Science and Welding

A Thesis Submitted to the Faculty of Mechanical Engineering
in Partial Fulfillment of the
Requirements for the Degree of
"Doktor der technischen Wissenschaften"

Graz University of Technology

Graz University of Technology

Institute for Materials Science and Welding

IWS MATERIALS IWS MODELLING IWS WELDING

Gewidmet – meiner Familie

Dem Mann an meiner Seite – MARTIN

Danke für all die Geduld und Deinen Beistand

Unseren Kindern – MARKUS und BIRGIT

Danke für die Erinnerung an andere so wichtige Seiten des Lebens

Meinen Schwiegereltern – CHRISTL und HEINZ

Danke für Eure so wertvolle Hilfe

Und insbesondere und vor allem meinen Eltern – ANNA und FRANZ

Danke für Alles - ohne Eure großartige Unterstützung wäre diese Arbeit niemals möglich gewesen!

Preface

This PhD thesis is submitted for the degree ‘Doktor der Technischen Wissenschaften’ at the Faculty of Mechanical Engineering at Graz University of Technology. The work was carried out between 2003 and 2010 under the supervision of Prof. Ernst Kozeschnik at the Institute for Materials Science and Welding and was part of the European research collaboration COST 536.

I declare that I have authored this thesis independently, that I have not used other than the declared sources / resources, and that I have explicitly marked all material which has been quoted either literally or by content from the used sources.

Cornelia Pein

Graz, May 2011

Acknowledgements

I would like to thank Prof. Ernst Kozeschnik for supervising this thesis - I did learn a lot from you in many ways.
I am very grateful to Em. Prof. Horst Cerjak for the kind possibility to work at the Institute of Materials Science and Welding at the Graz University of Technology. Furthermore, I would like to acknowledge Prof. Christof Sommitsch for the possibility to continue this work at the institute.
I would like to thank my colleagues from the Institute of Materials Science and Welding for the good collaboration throughout this work.
Finally I would like to thank my family and my friends – both living ones and those who already had to pass away – for your great support throughout the last years.

Ach, was muß man oft von bösen
Kindern hören oder lesen!
Wie zum Beispiel hier von diesen,
welche Stahl und Eisen hießen;
Spannung, Last und Hitze spüren
Kriechen, brechen, Form verlieren.
Zu wissen wo der Grund wohl liegt,
der Wissenschaft den Antrieb gibt.
Drum ist hier, was sie getrieben,
kalkuliert und aufgeschrieben.

(frei nach Max und Moritz von Wilhem Busch)

Contents

1 Abstract

Creep deformation of modern materials such as 9-12% Cr steels is of major importance in terms of long-term behaviour and component stability. Thus, modelling and simulation of this phenomenon is an important topic in the area of materials science. The influence of the materials microstructure on creep is complex, thus, the objective of this work is to simulate creep behaviour on a microstructural basis.

To do so, a model is set up which comprises the microstructure as distinct, spatially resolved elements which are described by different physical properties. The deformation process is implemented with a visco-plastic approach which is capable to describe both linear and non-linear behaviour. Out of the different physical mechanism operating during creep loading, Nabarro Herring creep is studied in this work.

As mathematical framework the Finite Element Method is used. For the numerical implementation of the presented model, the general-purpose, commercial software MATLAB® is utilized. The chosen numerical algorithm to analyse creep deformation is a robust and efficient method to calculate stress and strain response to given boundary conditions. A short overview on the mathematical framework and a description of the code implementation is given as well.

The model approach is used to simulate several microstructural configurations. The results indicate that the microstructural elements have a distinct influence on local creep behaviour of a creep loaded material.

2 Introduction

2.1 Motivation

Long term behaviour of materials due to mechanical and thermal load is an important topic in the field of material science in terms of structural stability, strength and deformation. Time-dependent deformation of a material under the influence of mechanical stress and elevated temperatures is defined as creep; creep is an essential topic concerning component safety and residual lifetime estimation.

In the last decades considerable effort has been taken to describe, understand and predict this phenomenon. First attempts consisted of simple parametric extrapolation, which turned out to be insufficient. Phenomenological approaches do not take any physical background into account as well, thus, any change in the underlying deformation mechanisms will lead to a very limited predictability in terms of deformation and creep straining. To overcome this deficiency statistical models have been established. These methods incorporate microstructural processes on a mean, statistical approach. Furthermore, they mostly focus on one distinct mechanism, thus denying possible interactions.

For a comprehensive approach for creep modelling, it is inevitable to improve and broaden these concepts. The heterogeneity of the affected microstructure has to be mapped explicitly, local effects have to be included and possible interactions have to be taken into account. To represent this complex long-term behaviour, a comprehensive model has to be set up on a spatially resolved basis. Different physical mechanisms and processes as diffusion of vacancies and the movement of dislocations have to be incorporated as well. Interactions of these mechanisms will be strongly dependent on this locally varying microstructure and its heterogeneous properties. Thus, a comprehensive understanding of these local microstructural processes and interactions in the dependence of this inhomogeneous microstructure is inevitable in order to give an accurate prediction of a materials' behaviour under creep conditions.

2.2 Objective

The objective of this work is to set up a spatially resolved microstructural model, which represents the materials microstructure by its heterogeneous components. These include the bulk material, grain boundaries and especially their connections in triple points, and the presence of particles and precipitates. The considered deformation mechanism for the presented studies is the diffusional flux of atoms through the bulk material (Nabarro-Herring creep). The model output is the local creep strain and the local internal stresses.

2.3 Methodology

To describe creep phenomena within crystalline structures, the Finite Elements Method is used within this project. With this methodology, it is possible to assess the physical parameters stress and strain in dependence of time and material parameters. The usage of a commercial Finite Element software package is disadvantageous in this case, because it is not possible to incorporate all mechanisms, especially some features of a spatially resolved microstructure, with locally differing characteristics. Therefore, the implementation of the model is realized in the multi-purpose mathematical software package MATLAB. This package is perfectly suitable for this type of modelling and it offers the additional advantage of ready-to-use graphical tools and other add-ons.

3 Creep in Poly-Crystalline Materials

This chapter gives an overview on creep phenomena and their classification. In the first part, the physical basis of creep is outlined; the second part reviews the fundamentals and current advances of creep modelling; in the third part, basics of creep modelling using the Finite Element Method are described.

3.1 Creep Phenomena in Materials

3.1.1 Phenomenological Description of Creep

A common definition is that creep is the plastic deformation proceeding at constant stress or constant load and constant temperature in time [1]. The experimentally observed time dependence of the creep strain can be graphically represented by a so-called creep curve. Usually, it consists of three stages in the most general form. A schematic example is shown in Fig. 1.

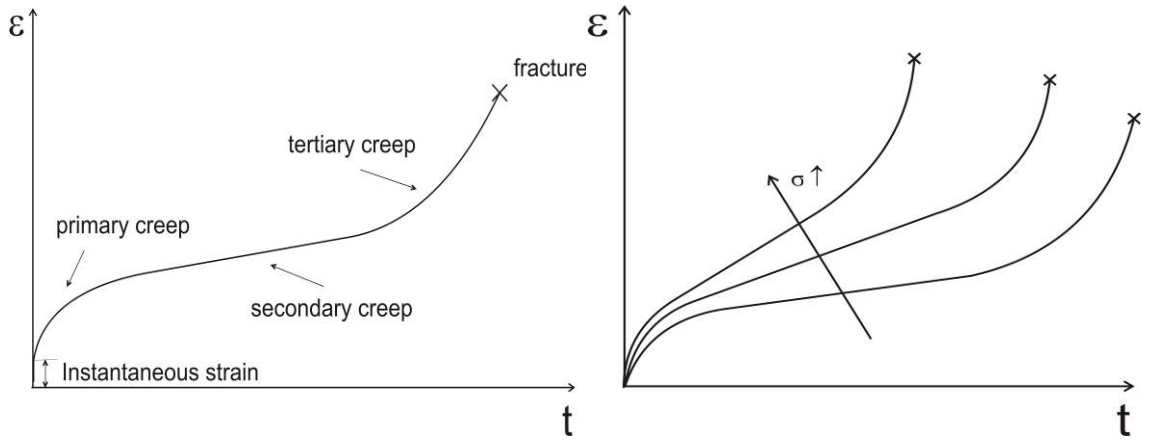

Fig. 1: (a) Schematic representation of a creep curve with three creep regimes. (b) Creep curves for different applied loads.

In the first stage, which is called primary or transient creep, the creep rate usually decreases in time, finally reaching a nearly constant value. The second stage is referred to as secondary or steady-state creep and it is characterized by a time-independent, constant creep rate. In the third stage, the creep rate increases with time. This stage finally terminates in fracture of the tested sample. Usually, the creep rate reaches its minimum in the steady state regime.
A creep curve as shown in Fig. 1 (a), usually, is valid for a certain temperature and a certain stress. For higher stresses, the creep rate is higher, creep strain will accumulate faster and the

specimen will rupture earlier. This trend is shown in Fig. 1 (b). Considerable effort has been spent to describe the time-dependence of creep curves. These approaches include empirical, phenomenological and physical methods [1].

Creep deformation is caused by different creep mechanisms. These include dislocation glide, non-conservative motion of dislocations (climb), grain boundary sliding and diffusion of vacancies. Depending on given conditions, such as stress, temperature or grain size, one of the mentioned creep mechanisms will dominate. This behaviour can be summarized in deformation mechanism maps, which were introduced by Ashby [2].

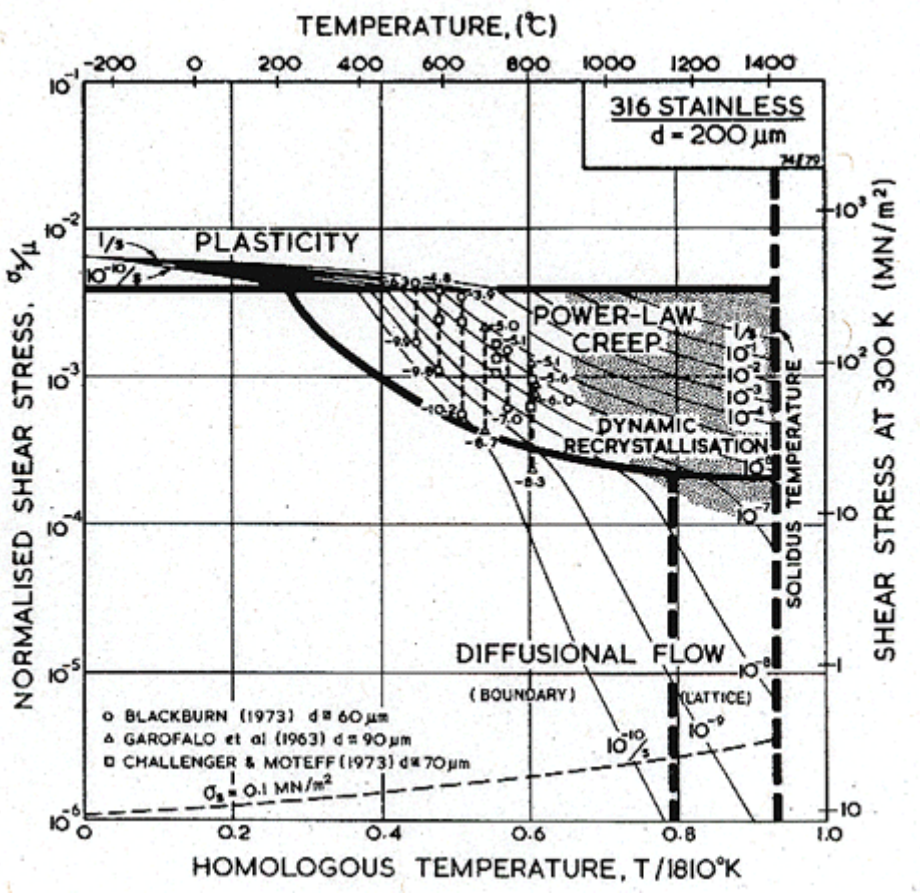

Fig. 2: Creep mechanism map for a stainless steel as originally published by Ashby [2]. The different fields and their dominating mechanism are outlined. Points, which are connected by thin, solid lines, have the same creep rate.

In the strict sense, not all creep processes are operating independently of each other, as frequently assumed [1]. Still, the construction of these diagrams relies on the simplifying assumption that all considered deformation mechanisms are working independently, and therefore can work in a parallel way. Moreover, creep mechanism maps do not include all

possible creep phenomena. Harper-Dorn creep, grain boundary sliding and Nabarro creep (non-conservative motion of edge dislocations) are often not considered [1].

Creep mechanism maps are divided into different sections. For each area in Fig. 2, the dominating mechanism is inscribed. The region denoted with plasticity is characterized by dislocation glide. Power law creep is a synonym for dislocation creep. Diffusional flow consists of diffusion of vacancies and atoms, either through grain boundaries or through the lattice. The axes represent the normalized shear stress σ/G, where G is the shear modulus and T/T_m is the homologous temperature and T_m is the melting temperature. Usually, the grain diameter plays an important role as well. Deformation mechanism maps are valuable in the analysis, which of the creep mechanisms is dominant for given conditions [1].

3.1.2 Diffusional Creep

3.1.2.1 The Phenomenological Laws of Diffusion

Diffusion is a process by which matter or energy is transported from one part of a system to another part. Diffusional creep, as a part of the field of material science, is related to a diffusional flux of material. The physical basics are random motions of structural lattice vacancies. The phenomenological theory of diffusion deals with this process on a macroscopic scale and is based on the assumption that the resulting flux of matter is proportional to the corresponding concentration gradient

$$J = -D\frac{\partial c}{\partial x} \tag{3.1}$$

where J is the diffusion flux, c the concentration, x the space coordinate measured normal to the section, and D is the diffusion coefficient. In general, D depends on temperature, pressure and concentration [3], but, in many cases, the diffusion coefficient can be taken as independent from the concentration. Eq. (3.1) is consistent only for an isotropic medium. It was first formulated by Fick (1855) and, therefore, is often referred to as Fick's first law [4].

The thermodynamic driving force for a flux can be written to be proportional to a gradient of a potential. In alloys, the gradient of a chemical potential acts as a driving force [5, 6, 7]. The velocity of the migration of a vacancy due to this force is proportional to the mobility of the specific moving species. Keeping in mind the Nernst-Einstein relation [7], which links the diffusion coefficient D with this mobility, the diffusive flux is given by

$$J = -D\frac{N_L}{kT}\nabla\mu \tag{3.2}$$

where N_L is the number of lattice sites per unit volume, k is Boltzmann's constant and T the temperature and $\nabla\mu$ the gradient of the corresponding chemical potential [5].

In a more general form, Svoboda et al [8] show that the diffusional fluxes for a multi-component crystalline system can be calculated using the thermodynamic extremal principle. These fluxes can be described using the chemical potentials of all system components linked by kinetic coefficients. These kinetic coefficients, in turn, depend on the diffusion coefficients of all species present in the system, the lattice site fraction of these species and their effective molar volumes. For a one-component system the diffusive flux can be expressed by

$$J = -\frac{N_0 N_1}{f N_0^{eq}\Omega}\frac{D}{kT}\nabla\mu_1 \tag{3.3}$$

where N_0 is the lattice site fraction for vacancies and N_0^{eq} the site fraction in equilibrium respectively, N_1 the fraction of the component, Ω the volume corresponding to one mole of lattice sites and f a geometric correlation factor depending on the crystalline structure.

3.1.2.2 Physical Basis of Diffusional Creep

Defects in Crystals

The physical basis of diffusional creep in crystalline materials is established by point defects within these materials. The two most common structural point defects in metallic solids are vacancies and self-interstitials. A vacancy is an atomic lattice position, which is not occupied [9]. A self interstitial is an atom of the crystal that occupies an interstitial site. They are causing a large structural distortion in their surrounding neighbourhood and, therefore, they are much less common than vacancies [9]. A schematic illustration of a vacancy in a crystal is presented in Fig. 3.

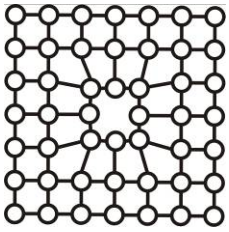

Fig. 3: Vacancy within a crystal lattice.

Vacancies are thermodynamically necessary due to the second law of thermodynamics. It states that the entropy of a closed system strives to reach a maximum. By adding vacancies to a given system, the number of possibilities to arrange the atoms is increased enormously. This causes a positive change in the entropy of the whole structure. Therefore, it is advantageous for the system, to provide the energy for the creation of vacancies [10].

Thermal vacancies are produced randomly, the activation energy for vacancy generation strongly depends on the type of source. Within undisturbed crystal lattices, a vacancy can only be produced together with an interstitial atom [11]. The generation of such vacancy-interstitial pairs requires very high energies, thermal lattice vibrations usually do not provide such high energies. On grain boundaries, surfaces and on other imperfections, vacancies can be generated with much less effort. Therefore, they play a central role in diffusional creep processes [11]. At those favourable sources, which are in general of non-ideal nature [8], vacancies need an activation energy of about 1 eV to be formed. The mole fraction of vacancies in equilibrium N_V is

$$N_V = A_V \exp\left(\frac{-E_V}{kT}\right) \tag{3.4}$$

where A_V is a factor, which has the value of about 3, k is Boltzmann's constant and T is the temperature [10]. The formation enthalpy E_V for vacancy formation is dependent on the material. For iron with a body-centred cubic (bcc) structure, it has a value of about E_V = 154 kJ/mol, whereas for the face-centred cubic (fcc) form a value of about E_V = 135 kJ/mol can be found in literature [12].

Non-Equilibrium

The equilibrium concentration of vacancies is altered, if tensile or compressive stresses are present. This non-homogeneous distribution results in vacancy fluxes through the material, as outlined here following the argumentation of Nabarro [13]. Later, Herring conducted a more general analysis using chemical potentials and considering the fluxes within a polycrystal [1,5].

In Fig. 4, a schematic drawing of an idealized crystal is presented. It does not contain dislocations, the only source and sink for vacancies are the faces. This crystal is acted on by equal and opposite normal stresses σ as indicated in Fig. 4.

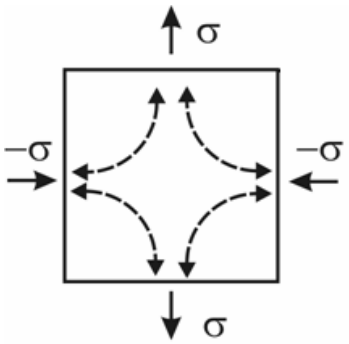

Fig. 4: Schematic single crystal with applied stresses and corresponding vacancy and mass fluxes.

For the creation of a vacancy at a face, where compression takes place, an atom must be transferred from the inside of the crystal to its face. The work $\sigma\Omega$ must be expended for this movement of the atom, where Ω is the atomic volume. The enthalpy of vacancy creation therefore increases, compared to the unstressed state. On faces where tensile stresses are acting, the enthalpy for vacancy creation is lowered by $\sigma\Omega$. Therefore, the equilibrium fraction of vacancy concentration is changed. A local imbalance in vacancy concentration occurs, where the fraction of vacancies in areas with tensile stress is

$$N_{\mathrm{V}}^{+} = N_{\mathrm{V0}} \exp\left(\frac{\sigma\Omega}{kT}\right), \tag{3.5}$$

and, in areas with compressive stress, it is

$$N_{\mathrm{V}}^{-} = N_{\mathrm{V0}} \exp\left(-\frac{\sigma\Omega}{kT}\right) \tag{3.6}$$

where N_{V0} is the equilibrium fraction of vacancies in the unstressed state. The difference in vacancy concentration is the driving force for a flux of vacancies from areas with high vacancy concentration to areas with low concentration [1]. This driving force corresponds to the chemical potential as stated in section 3.1.2.1. The resulting flux of vacancies is compensated by a diffusional flux of atoms from parts of the grain, where they are under compression, to parts of the grain, where they are under tension. In other words, the flux of vacancies into a specific direction causes a transport of mass in the opposite direction. A plastic deformation of the grain or the specimen in the tensile direction is the consequence [11].

Nabarro and Herring consider this mass flux to occur within the grains, therefore this creep regime is referred to as Nabarro-Herring creep. Coble [14], in contrast, regarded diffusional processes taking place along the grain boundaries, this kind of creep phenomenon therefore is

termed Coble creep. The main difference between Nabarro-Herring creep and Coble creep consists of the grain size dependence [15].

Diffusion Coefficient

As already stated in section 3.1.2.1, the flux of vacancies can be calculated from Fick's first law. The constant of proportionality between the concentration gradient and the resulting flux is the diffusion coefficient. Its value is different for different processes, such as diffusion of interstitials, self-diffusion or diffusion of vacancies. The self-diffusion coefficient D_L can be calculated via the diffusion coefficient for vacancies D_V by

$$D_L = D_V N_{V0} = D_V C_0 \Omega \tag{3.7}$$

where C_0 is the vacancy concentration in equilibrium $C_0 = N_{V0}/\Omega$.

The diffusional creep rate increases linearly with the applied stress [1]. Its temperature dependence is determined practically via the coefficient of lattice self-diffusion [1]. This dependence can be described as usual for a thermally activated process by [11]

$$D_L = D_0 \exp\left(-\frac{Q}{RT}\right) \tag{3.8}$$

where Q is an activation energy and D_0 a pre-exponential factor. Values can be found in e.g. [11] and [2]. As an example, the diffusion coefficients for pure iron are shown in Fig. 5 [2]. Phase transformations are indicated in the diagram as well, because the value of D_L is highly dependent on the phase of the material. When ferrite transforms to austenite, a sharp decrease of the diffusion coefficients is observed.

For grain boundaries, the diffusion coefficient has to be evaluated separately. Diffusion along grain boundaries can be several orders of magnitude faster than in the matrix. Thus, the diffusion coefficient in grain-boundaries is different from that for lattice diffusion. Amorphous high angle grain boundaries in particular act as high diffusivity paths [16], because of their highly irregular atomic structure. In contrast to lattice diffusion, the grain boundary diffusion coefficient differs only slightly between α and γ iron. In Fig. 6, the experimentally found data published in [16] are reproduced.

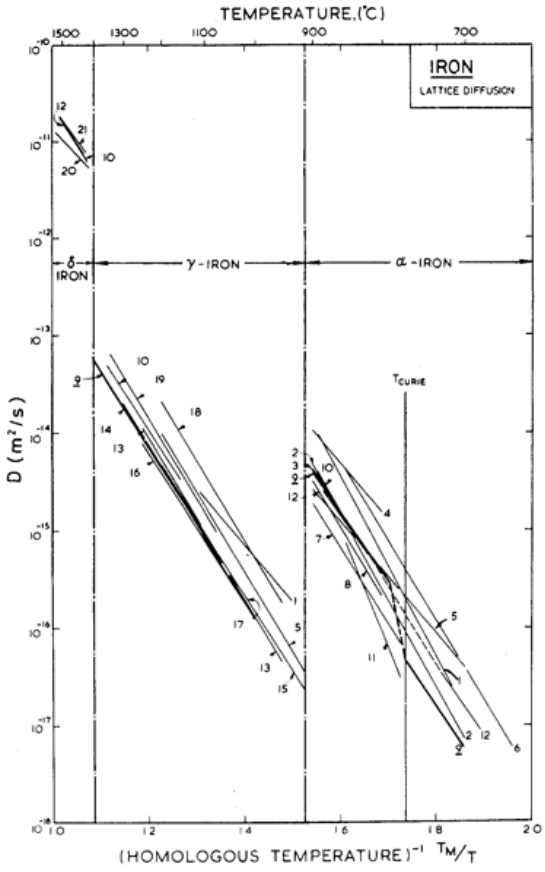

Fig. 5: Diffusion coefficients for self diffusion within the lattice in iron in dependence of temperature a published in [2].

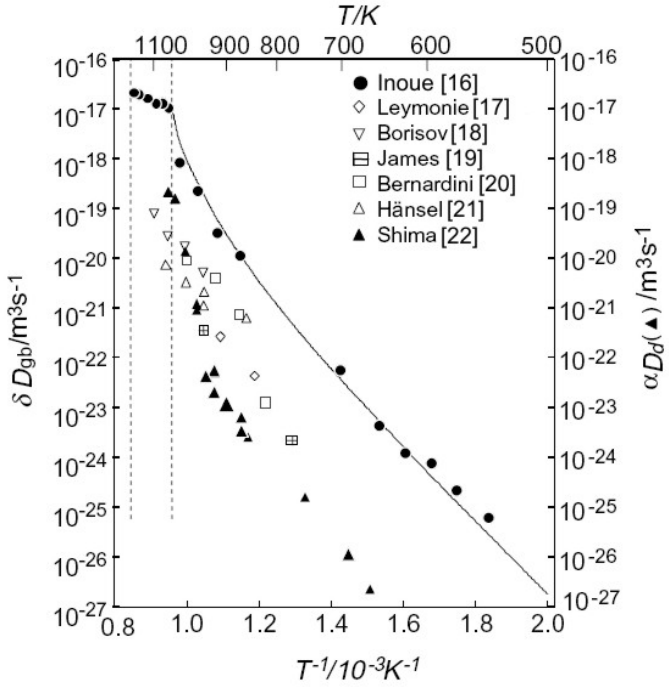

Fig. 6: Arrhenius plot of grain boundary diffusion coefficient as published in [16] in dependence of temperature. Data from other authors [17, 18, 19, 20, 21, 22] are indicated as well.

3.1.2.3 Stress Directed Diffusion

Grain boundaries influence diffusional processes in several ways. Different grain boundaries have different orientations with respect to the direction of the applied stress, and, therefore, experience not the same normal stresses in a given stress field. The concentration of vacancies within the bulk material in the vicinity of a grain boundary is dependent on the normal stresses [11]. Hence, the thermal equilibrium concentration of vacancies is altered in the direct neighbourhood of a stressed grain boundary. This degree of change of concentration is dependent on the angle between the grain boundary and the existing stress within the material. The new concentration is calculated by equations (3.5) and (3.6) [23]. The resulting flux of vacancies is counterbalanced by a flux of atoms in the opposite direction. The plating of atoms on the grain boundaries is causing a displacement of the adjacent grains.

For diffusion through the bulk material, the displacement rate $\dot{u}_n$ between adjacent grains can be expressed by

$$\dot{u}_n = \frac{\Omega D_{\mathrm{V}}}{kT} n_i \left(\nabla_i c^+ - \nabla_i c^- \right) \tag{3.9}$$

where n_i is the unit normal vector pointing into the upper grain, $\nabla_i c^+$ is the concentration gradient above the boundary, and $\nabla_i c^-$ is the concentration gradient from the grain below the grain boundary. For steady state situations, this relation can be transcribed to the known equation for Nabarro-Herring creep [11].

For diffusion along boundaries, a similar result can be derived. Considering grain boundaries where a normal stress is acting on, the grain boundary lowers this potential by a negative work. A flux of atoms in the grain boundary will occur. The resulting displacement rate can be calculated by

$$\dot{u}_n = \frac{\Omega D_{\mathrm{gb}}}{kT} \nabla^2 \sigma_n \tag{3.10}$$

where Ω is the atomic volume, D_{gb} the grain boundary diffusion coefficient, σ_n is the normal component of the stress acting on the grain boundary, k is the Boltzmann constant and T the temperature. For steady state situations, this relation can be further simplified [11].

In surfaces, diffusion phenomena in general will take place as well. Surface diffusion controls the shape of growing cavities. The tendency to minimize the free surface energy acts as driving force.

3.1.2.4 Diffusional Creep and Grain Boundary Sliding

Diffusional creep and grain boundary sliding are closely related to each other. The flux of atoms from boundaries acted on by compressive stress and to boundaries acted on by tensile stresses cause changes in grain shape. These changes must be accommodated, otherwise voids would form and material coherency would not be maintained. Accommodation can be established by grain boundary sliding. This interaction was analysed by many authors and it is generally accepted as a necessary accommodation process of diffusional creep [24]. The geometrically necessary grain boundary sliding is known as Lifshitz sliding. It can be observed by marking lines across the grains as shown in Fig. 7. After deformation by tensile stress a misfit in this marker line indicates that grain boundary sliding has occurred [24].

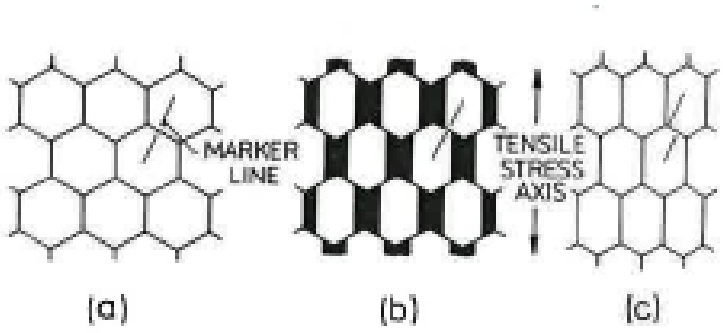

Fig. 7: Grain boundary sliding measured by marker lines. Part (a) shows the original configuration. (b) The new shape of the grains as a result of diffusional creep without grain boundary sliding. (c) Diffusional creep accompanied by grain boundary sliding as indicated by the offset of the marker line. Originally presented by Čadek [1].

Although, in the past, some authors tried to assign the creep strain to separate distributions of both mechanisms, in a general view, the strain rate cannot be divided into separate contributions of diffusion and grain boundary sliding. It is argued that plastic strain can take place only if both mechanisms operate simultaneously. In other words, diffusional creep can either be considered as a diffusion process accommodated by grain boundary sliding or as grain boundary sliding accommodated by diffusion. Material deformation cannot develop in the absence of either mechanism. The whole creep strain then either can be ascribed to grain boundary sliding or to diffusion [1,23,25,26,27].

At small grain sizes, the sliding rate can be written as

$$\dot{\varepsilon}_{\mathrm{gbs}} = A_{\mathrm{gbs}} \frac{D_L}{L^2} \left(\frac{\sigma}{E} \right)^2 \tag{3.11}$$

where E is the Young's Modulus, L a mean linear intercept grain size and A_{gbs} is a constant to be determined [28].

3.1.2.5 Grain Boundaries and Threshold Stress

At low stresses, there seems to be a threshold behaviour in diffusional creep as well. In creep deformation, the applied stress then can be replaced by the effective operating stress

$$\sigma_{\text{eff}} = \sigma - \sigma_{\text{th}} \tag{3.12}$$

where σ_{th} is the threshold stress. In pure metals, the threshold stress in general is below 1 MPa when measured at around half the homologous temperature. In materials, which contain high melting particles on the grain boundaries, the threshold stress can be larger, but is not greater than a few MPa, even in commercial stainless steels [11].

As a possible explanation for this threshold stress, the role of grain boundaries and their interactions with the bulk material is frequently debated in literature [29, 30, 31, 32, 33, 34, 35]. Grain boundaries act as fast diffusion paths because of their, in general, highly disordered atomic structures. The grain boundary is assigned with a thickness of about one atomic layer up to 10 nm. The material diffusion through the boundary will partly leak into the surrounding grains by volume diffusion. The extent of this lateral leakage is determined by the kinetics of diffusion and the two different diffusion coefficients of the grain and the grain boundary [3]. The generation of these vacancies must be fast enough to compensate the drain of vacancies caused by stress directed diffusion. In general, it is assumed that this process is fast and efficient enough, and can easily provide enough vacancies to maintain the thermal equilibrium concentration. For many cases, this assumption is sufficient. The diffusion rate is then only determined by the transport through the grain itself [1,11]. Nevertheless, this assumption seems to be too simple to explain several observations in some alloys, such as lower creep rates than predicted, a threshold stress below which no creep occurs [35] and differing activation energies [1]. A possible explanation would be that the grain boundary does not act as a source and sink in the whole plane, but the emission and absorption of vacancies takes place at discrete positions in the boundary. Grain boundary dislocations, which are constrained to remain in the boundary when moving, provide an appropriate source and sink. While emitting or absorbing vacancies, these dislocations climb in the boundary plane [1]. The rate of diffusion along grain boundaries will be limited by this process [35].

Arzt et al [36] set up a two dimensional model of a crystal with grain boundaries, which are made out of straight, parallel grain boundary dislocations. A correction factor, which depends on the number of the dislocations, has to be introduced. For pure metals, this factor is close to

unity, and therefore gives a possible explanation for the good agreement of theoretical and experimental results in pure metals [1].

When the grain boundary dislocations climb, while they are emitting or absorbing vacancies, their line length and the associated energy are fluctuating. This leads to a threshold stress for diffusional creep, which can be modelled by [1]

$$\sigma_{\mathrm{th}} \cong \frac{1}{2}\frac{Gb_{\mathrm{B}}}{d} \tag{3.13}$$

where b_{B} is the length of the Burgers vector of a boundary dislocation, d the grain diameter and G the shear modulus.
Another explanation for the threshold stress is given by Burton [37]. It states that dislocations can be multiplied by spiral dislocation sources. In this case, the resulting dislocation density is not constant in the grain boundary. At stresses lower than the threshold stress, the critical radius for the nucleation of a dislocation loop is not reached. The dislocation source will not operate and thus creep will not occur. This assumptions lead to an equation identical to equation (3.13).

Burton and Reynolds [23] focus on a theory, where a grain boundary can only act as a source for vacancies if the saturation of vacancies at the grain boundary exceeds a certain value, which is coupled with the threshold stress σ_{th}. This threshold stress is dependent on the number of foreign particles collected at the grain boundaries. During straining, this number is not constant. Especially at grain boundaries parallel to the applied stress, an increase in the density of those particles collected by the elongating grain boundary is expected. As a consequence, the threshold stress increases with increasing strain. This implicates that the strain and the strain rate decay exponentially with time.

Experimental data, which confirm a threshold stress in diffusional creep within a polycrystalline material, are available for a number of pure, nanocrystalline metals [35,38,39,40]. The temperature dependence of the threshold stress was determined for alpha iron to slightly decrease with increasing temperature [40]. Creep testing on uranium dioxide indicates that the temperature dependence of a threshold stress for diffusional creep can be described by an Arrhenius law and that the stress decreases with increasing temperature [41].

3.1.2.6 Inhibition of Diffusion Creep

Inhibition of diffusion creep can occur [23] as a result of difficulties in accommodating atoms in grain boundaries or in the interface between hard grain boundary particles and the matrix. This inhibition can be bypassed by stresses exceeding the threshold stress [11]. Inhibition of diffusion creep plays an important role in nucleation and growth of creep cavities.

Riedel [11] presents a simple model of inhibited diffusion creep with accommodation by power-law creep. He argues that, at very low stresses, all stress is concentrated on the particles. The deformation then is controlled by localized creep of the grains near the particle. The strain rate is dependent on some power n of the applied stress. Especially for very low stresses, this dependency causes a sharp decline in the strain rate with decreasing stresses. In fact, there is no real threshold stress in this model, but the steep decrease of the strain rate could be regarded as quasi-threshold for diffusional creep.

3.1.2.7 Debating Diffusional Creep

Especially for pure metals, the agreement of both theories with experimental data [35,45] is remarkable. In other cases, especially in solid solution alloys and alloys with a fine dispersion of the second phase, several observations cannot be fully explained by the Nabarro-Herring and the Coble theory [1].

For identifying a creep process as diffusional creep, several requirements have to be fulfilled. First, the creep rate has to be linearly dependent on the stress, i.e. the stress exponent has to be unity. Second, the dependency of the creep rate on grain size has to match. And third, the activation energy has to correspond to that for self-diffusion and, finally, experimental observation and theoretical prediction must agree [42]. As an indication for diffusional creep, denuded zones are designated. Denuded zones are zones, which contain no precipitates after creep. They form on grain boundaries transverse to the applied tensile stress. Usually they are taken as evidence for diffusional creep phenomena [42].

The existence of diffusional creep, especially in polycrystalline, precipitate-containing materials, has been debated by some authors in the last years [23,28,43,44]. The disputes comprise experimentally measured creep rates, which do not agree with those predicted by theory, the grain boundary position within the denuded zone and a stress-dependence not consistent with theory [23,44].

A diffusion-controlled dislocation creep mechanism at high stresses and Harper-Dorn creep at low stresses are proposed to explain the observed creep phenomena instead of diffusional creep [44]. On the other hand, it is argued that the role of grain boundaries as source and sink still is not clear in detail, and that the effects of this constraint may play a major role in diffusional creep phenomena [28]. The deposition of material at grain boundaries normal to the applied stress and depletion of material on grain boundaries parallel to the applied stress are interpreted as evidence for diffusional creep as well [43,45]. Furthermore, it is argued that the position of the grain boundary within the denuded zone is not necessarily located centrally, and therefore cannot be used as evidence against diffusional creep [43]. Therefore, modifications of the existing theories for diffusional creep seem to be superior to a complete rejection of the whole theory. Detailed discussions can be found in literature [23,28,42,43,44,45].

3.1.3 Harper-Dorn Creep

Harper and Dorn [46] suggest a dislocation climb process as an additional operative mechanism for creep at high temperatures. The basic mechanism in Harper-Dorn (H-D) creep consist of vacancies diffusing from edge dislocations with Burgers vectors parallel to the tensile axis to edge dislocations with Burgers vector normal to the tensile axis. This process acts within the grain, and there is no depletion or accumulation of atoms on the grain boundaries. The diffusion of the vacancies can take place via the bulk or via the dislocation cores depending on temperature [25].

Harper-Dorn creep is a deformation mechanism, which operates at low stresses and high temperatures [47]. First, H-D creep has been assumed to take place at normalized stresses σ/G below 5×10^{-6} and homologous temperatures higher than about 0.95. But it has been shown that H-D creep can take place at lower homologous temperatures as well [1,48]. Since it occurs intragranularly, the creep rate is independent of the grain size. At high homologous temperatures, it is claimed to be the dominant creep mechanism [28]. The dislocation density in Harper-Dorn creep region is low and independent of the applied stress [28,49,50], though it is specific for the material used [49]. In some reports of experimental data, discrepancies between reported values and theoretical prediction for the dislocation density are observed. According to [28], this is due to a systematic error in the measurements.

To identify Harper-Dorn creep as the rate controlling process, three conditions have to be fulfilled. First, the stress dependence of the creep rate muss be linear, that is, the stress exponent has to equal $n = 1$. Second, the creep rate has to be much faster than for other possible concurring creep mechanisms, such as Nabarro-Herring creep or even Coble creep, if the testing is carried out at lower homologous temperatures. Third, it has to be shown that the grain size does not influence the creep rate, which is the case in Nabarro-Herring or Coble creep [28,51]. Čadek [1] and Kassner [48] state some additional characteristics of Harper-Dorn creep, which include that the creep curve shows a distinct primary stage, the dislocation density has to be low and independent of stress, and that the activation energy is equal to the activation energy of lattice diffusion.

The existence of Harper-Dorn Creep has been widely discussed by some authors. The experimental observations connected with Harper-Dorn creep cannot be fully explained by a single theory [49]. In experiments, especially the linear stress dependence with $n = 1$, could not always be observed in the questionable stress and temperature range [51]. Other data and their interpretation sometimes are ambiguous as well [48].

In [50,52], several creep tests with pure lead (pb) have been conducted. In contrast to other publications, it is found that, for very low stresses and large strains, Harper-Dorn creep has not a Newtonian character but the stress exponent is closer to $n = 3$. Nevertheless, Kumar [52] declares the testing results to be consistent with Harper-Dorn creep. The discrepancy is explained by re-evaluation of previous results and re-plotting the data versus the true stress instead of incorporating a threshold stress. When doing so, both data sets show good agreement. Similar results are obtained for aluminium by Kumar et al. [53].

3.1.4 Power Law Creep

3.1.4.1 Dislocations

Dislocations are line defects within a crystal. They are quantified by a Burgers vector. Due to their presence, the surrounding lattice will be distorted. The presence of dislocations in general strongly influences the strength, the plasticity and creep processes of a material [10]. The study of their generation and motion is an important field in creep modelling, and general materials science.

Two different types of dislocations can be distinguished; both are presented in Fig. 8. An edge dislocation is a line defect within the crystal at which an extra plane of atoms terminates. The Burgers vector is perpendicular to the dislocation core and lies within the distinct slip plane of the dislocation. The strain field initiated by this type of dislocation consists of compressive, tensile and shear strains. The strain drops radially with distance from the dislocation core. The second type of dislocations is a screw dislocation, which creates a spiral ramp of crystal planes [10]. The Burgers vector is parallel to the dislocation core, a screw dislocation has no distinct slip plane. The strain field initiated by this type of dislocations only consists of shear strains [54].

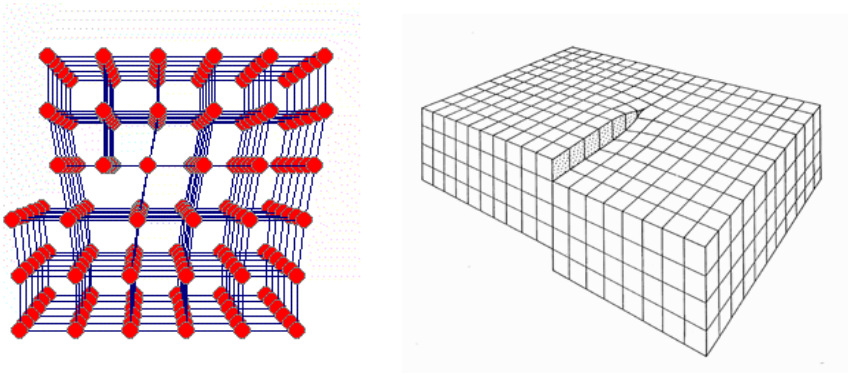

Fig. 8: Edge dislocation and screw dislocation.

3.1.4.2 Movement of Dislocations

The motion of dislocations is one of the most important causes of plastic deformation of crystals at stresses below the theoretical shear strength [55]. Two types of movements for dislocations exist. For the first, one has to keep in mind that the atomic bonding at the dislocation core is weaker than in a perfect crystal. Thus, at low stresses, the atoms can relatively easy be locally rearranged and the dislocation line can move through the crystal. This process is called slip or glide [1,10]. Edge dislocations have a distinct slip plane within which they can move. This plane is necessarily parallel to the core line and the Burgers vector of the concerned dislocation [56]. Screw dislocations can also be envisaged as to move in a slip plane, but in contrast to edge dislocations, the dislocation line and the Burgers vector are parallel and therefore do not define a unique plane. As a result, the glide of the dislocation is not restricted to a specific direction. In both cases, a shear stress must act on the slip plane in the direction of the Burgers vector, irrespective of the direction of the dislocation core line.

The glide velocity of a dislocation is dependent on the type of dislocation, the material, the acting stress and the temperature. This velocity, additionally, is altered when a field of local

obstacles is present. Then, the glide velocity can be regarded as the maximum attainable velocity [1].

The second mechanism, by which dislocations can move, is climb. It is considered as a non-conservative motion. Atoms are added to, or removed from, the bottom of the extra plane, therefore, this motion involves two processes. First, the emission or absorption of a vacancy at the dislocation core, and, second, long-range diffusion of the vacancy to or from the dislocation. If the dislocation represents a perfect source or sink for vacancies, the velocity of the climbing dislocation is controlled by this diffusional transport of vacancies. In most cases, the relaxation time for diffusion from source to sink is large, compared to the nucleation time for vacancies. Therefore, it is a good approximation to consider climb as a diffusional boundary problem. As for dislocation glide, several approaches to quantify the velocity for climbing can be found in literature [1].

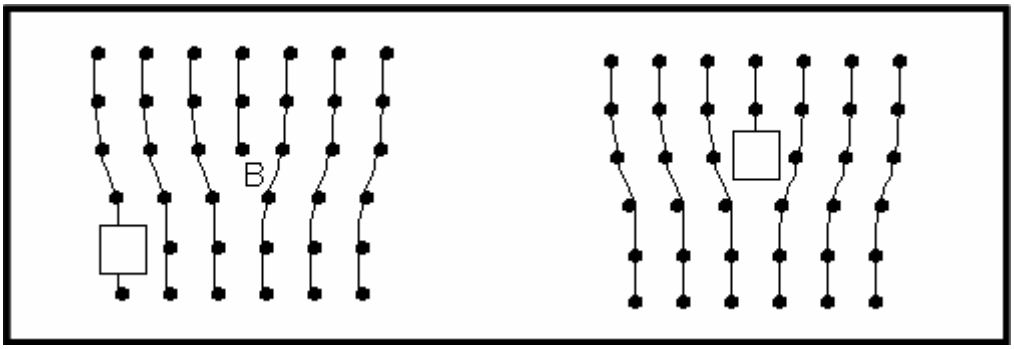

Fig. 9: Dislocation climb accompanied by diffusion of vacancies. The vacancy diffuses to the dislocation core and replaces an atom. The dislocation climbs.

3.1.4.3 Mobile Dislocation Density

Not all dislocations within a crystal can move freely. Only a fraction of all free dislocations – dislocations, which are not associated with boundaries - is potentially mobile when stress is applied. Of these mobile dislocations, only a relatively small fraction is actually moving. Therefore, these terms should be carefully distinguished.

The ratio of the mobile dislocation density can be estimated by some model ideas. One of these theories starts from the idea that the free dislocations are arranged into a network and may be linked to each other, and basically three processes can be distinguished:

- The release of some links,
- the glide of the released links,
- and the capture by other links.

The time interval from a link release to its next capture is assumed to be negligible compared to the time necessary for a link to be released. Thus, at any instant in time nearly all free dislocations are part of the dislocation network and the density of moving dislocations represents only a very small fraction of the free dislocation density. The density can be calculated by using the distribution of the link lengths, where only links of lengths greater than a critical link length are considered. Further details of the theory can be found in [1,57].

The model of Gasca-Neri and Nix [1,58] to calculate the mobile dislocation density starts from the idea that a dislocation glides in a glide plane containing point obstacles. If the dislocation is arrested by these obstacles, the segments between these obstacles bow out in the positive direction. If the applied stress is high enough to bypass, immediately after passing, a dislocation segment bows out in the negative direction. The distribution of these dislocation segments with respect to their radius of curvature R is used in this model as the basic distribution function. Again, only dislocation segments having a minimum critical curvature are considered to calculate the mobile dislocation density.

3.1.4.4 Dislocation Structure and Subgrain Formation

Dislocations are mostly arranged into networks. The greater part is organized in three-dimensional ones, fewer in two-dimensional ones, which form sub-boundaries. The formation of such networks and subgrain structures is the result of the tendency of homogeneously distributed dislocations to create modulated structures. This structure is dependent on the applied stress and tends to change when this stress is altered. But the configuration is influenced by grain size, misorientation and a number of conditions concerning the glide systems as well. At the nodes, where the dislocations are meeting, the sum of the Burgers vectors must equal zero. This structure is very heterogeneous and is strongly influenced by stacking fault energy, especially during primary creep [1].

Quantitative descriptions of dislocation structures can be found in numerous publications, a review is given in [59]. These include

- the density of free dislocations,
- the density of dislocations forming sub-boundaries,
- and the mean subgrain diameter.

The density ρ_u of remaining unbound, free dislocations is dependent on the applied stress and can be described by

$$\rho_{\mathrm{u}} = K_{\mathrm{G}} \left(\frac{\sigma}{Gb} \right)^{p} \tag{3.14}$$

where K_{G} is a constant, p is a value derived from theories of deformation strengthening, G is the shear modulus and b the norm of the Burgers vector [1].

The density of dislocations, which form subboundaries, is dependent on the misorientation Θ between the adjacent grains and is given by

$$\rho_{\mathrm{b}} = K_{\mathrm{B}} \frac{\Theta}{b^2} \frac{\sigma}{G}, \tag{3.15}$$

where K_{B} is a constant [1] given with $K_{\mathrm{B}} \cong 0.3$. The mean subgrain diameter d_{s} is described using the total dislocation density $\rho_{\mathrm{t}} = \rho_{\mathrm{u}} + \rho_{\mathrm{b}}$ with

$$d_{\mathrm{s}} = K_{\mathrm{t}} \rho_{\mathrm{t}}^{-1/2} \tag{3.16}$$

where K_{t} is a constant.

3.1.4.5 Subgrain Structure and Internal Stresses

Considering a subgrain structure composed of dislocations, the dislocation density is highly heterogeneous in the crystal. Dislocation walls contain a high dislocation density, whereas in the volume of the subgrain, the dislocation density is relatively low [1]. These different densities, together with the condition of continuous deformation, are causing different stresses in different areas. The local shear stresses within the walls are higher than in the cells themselves. Therefore, the walls can be considered as hard regions and the cell interiors as soft regions [60]. The mismatch in elastic strain is accommodated by dislocations at the interface between the two areas. As a result, the internal stresses will not be homogeneous; further influences are due to elastic bending of sub-boundaries and from sub-boundaries terminating within the crystal. Experiments support the concept of hard and soft regions [1].

3.1.4.6 Interactions of Dislocations and Sub-Boundaries

Sub-boundaries are, in general, obstacles for moving dislocations. First, their velocity is strongly reduced, then, the dislocation is absorbed by the sub-boundary. Occasionally, the dislocations may penetrate the boundary and continue to move in the adjacent subgrain. Dislocation annihilation by sub-boundaries is another type of possible interactions and plays an important role in recovery at high temperatures. Sub-boundaries can provide a source for dislocations as well, creep of copper single crystals and aluminium polycrystals has shown evidence for this [61].

3.1.5 Creep and Superplasticity

Superplastic materials exhibit a high tensile ductility [62]. In general, grain boundary sliding is accepted as the mechanism for creep deformation of superplastic materials [44]. Usually, a stress exponent with the value $n = 2$ is observed. The necessary accommodation process is modelled in different ways. Some theories [63] feature climb of dislocations as the accommodating mechanism. Dislocations are created in grain boundaries to overcome obstacles. They can then glide across the grain and pile up on the opposite side, which will lead to an additional stress term, i.e. the stress exponent in the creep equation will change from 1 to 2. Other models [64, 65] state that grain boundary sliding accommodated by slip recovery is the critical mechanism for accommodation. A short overview of existing theories is given by Ruano et al. [44].

3.1.6 Microstructure and Creep

The term *microstructure* defines the totality of all thermodynamic non-equilibrium lattice defects and phases on a spatial scale that ranges from Angstrom to meters. Its evolution in time can range from picoseconds to years [66].

Creep is closely related to the microstructure of a material. The microstructure influences the creep behaviour, and creep changes the microstructure. The phases and defects of such a structure have to be defined by their type, structure, number, shape and topological arrangement [55]. The basic defects on the atomistic level have already been introduced in chap. 3.1.2.2 and 3.1.4.1. In this section, properties and features of crystal structures and phases are briefly reviewed.

3.1.6.1 Grain Boundaries

The interface between two crystalline grains is termed as a grain boundary. To describe such a grain boundary exhaustively, not only the position of the grain boundary itself, but also the relative misorientation of both adjacent, crystalline grains are necessary.
The misorientation between the two grains can be illustrated by a rotation of the crystallographic system. Three parameters are necessary to describe such a rotation: the normalized axis (two parameters) and the angle of rotation (one parameter). This angle is used to separate grain boundaries in low-angle and high-angle types [67]. Both are outlined in the next sections.

High angle boundaries

High angle grain boundaries can have equilibrium and non-equilibrium structures. Concerning equilibrium structures, various boundary models are based on the idea that a boundary consists of an array of dislocations. When doing so, one has to realize that grain boundary dislocations and lattice dislocations in general cannot be assumed to have the same structure and Burgers vector [55].

If the dislocations are uniformly spaced, a low-energy boundary is assumed to form. This spacing can only occur if the dislocation spacing matches the number of lattice planes terminating at the interface, as depicted in Fig. 10.

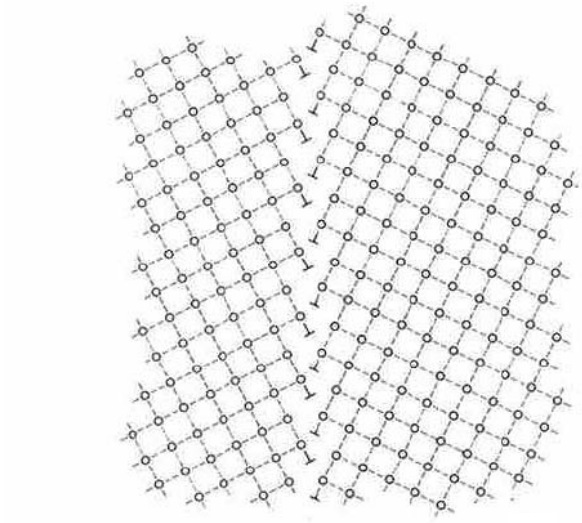

Fig. 10: High-angle (53°) grain boundary of a simple cubic structure built up by dislocations [55].

Boundaries with other angels can be described by the superposition of a boundary with uniform dislocation spacing, and a small-angle tilt boundary. Any other deviation from the low-energy orientation can be accommodated by an additional network of dislocations. High angle boundaries of this type can be found in twinned crystals [55].

In other types of grain boundary models, it is assumed that the boundary consists of groups of atoms, which are densely packed, e.g. in rings with a central atom, as depicted in Fig. 11. Such formations are similar to those existing in amorphous structures. Therefore, the properties of such a boundary can be compared to those of glassy structures, although differences exist. An interface has periodic boundary conditions, which are given by the

periodic structure of the adjacent crystals, whereas a group of atoms in a glassy structure is not exposed to such periodic conditions [55].

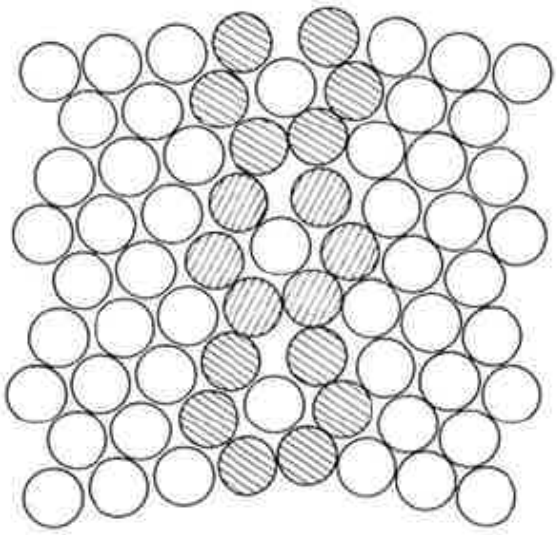

Fig. 11: A grain boundary model considering densely packed groups of atoms [55].

If a boundary is in non-equilibrium, as it can occur during deformation etc., its structure may deviate from the structures discussed above, and structural defects can be included. One of these defects are vacancies. If the boundary has a rather structured configuration, the displacement field caused by the vacancy spreads primarily into the adjoining lattice sites. If the atomic matching is relatively poor, the vacancy causes large atomic displacements in its neighbouring region, but the extent of the field itself is much smaller, as can be seen in Fig. 12 [55].

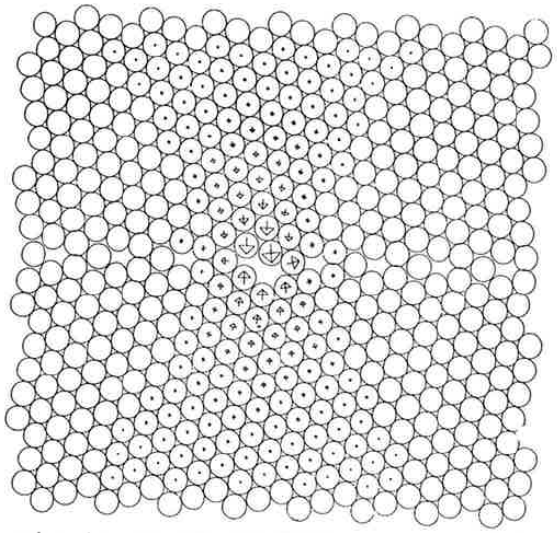

Fig. 12: Relative displacements of atoms caused by a vacancy after [55].

In non-equilibrium, additional dislocations, which are not part of the equilibrium configuration, can enter a grain boundary and change the equilibrium configuration. They are designated as extrinsic dislocations. Several ideas to explain this process exist. These include dissociating the dislocation, spreading the cores of the boundary dislocations and reorganizing the existing boundary dislocations [55].

In ref. [67], the distribution of the angle and the axis of rotation of grain boundaries are extensively studied.

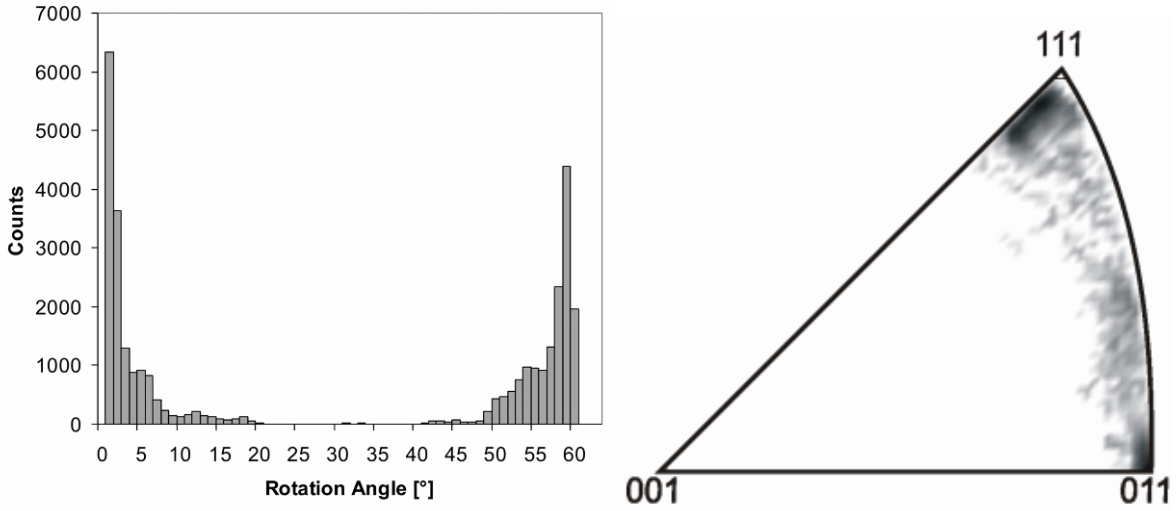

Fig. 13: Distribution of misorientations of sub-boundaries in thermally aged CB8 measured by Sonderegger [67]. (a): angle, (b): distribution of orientation axes.

As an example, a measurement of the grain structure of a specimen of the steel CB 8 (4000 h, thermally aged) is shown here. The statistical data of the misorientation angle can be found in Fig. 13 (a). The orientation axes of the high angle boundaries are shown in Fig. 13 (b). It can clearly be seen that the greater part of these axes do not exactly have an exact orientation of [1 1 1], but show a distinct deviation of some degrees.

Small Angle Boundaries

Small-angle boundaries can be defined as interfaces between lattices that have only a slightly different orientation. Boundaries of this type can be viewed as periodic, two-dimensional networks of dislocations and can be quite complex. The structure, as depicted in Fig. 14, can be visualized as similar to those of high angle grain boundaries. Their formation is often due to the reduction and cancellation of long-range strain fields caused by randomly distributed dislocations. The movement and changes of such networks can be explained by different

mechanisms. These include glide of dislocations, climb accompanied by vacancy absorption and emission, and climb and glide motion along the boundary [55].

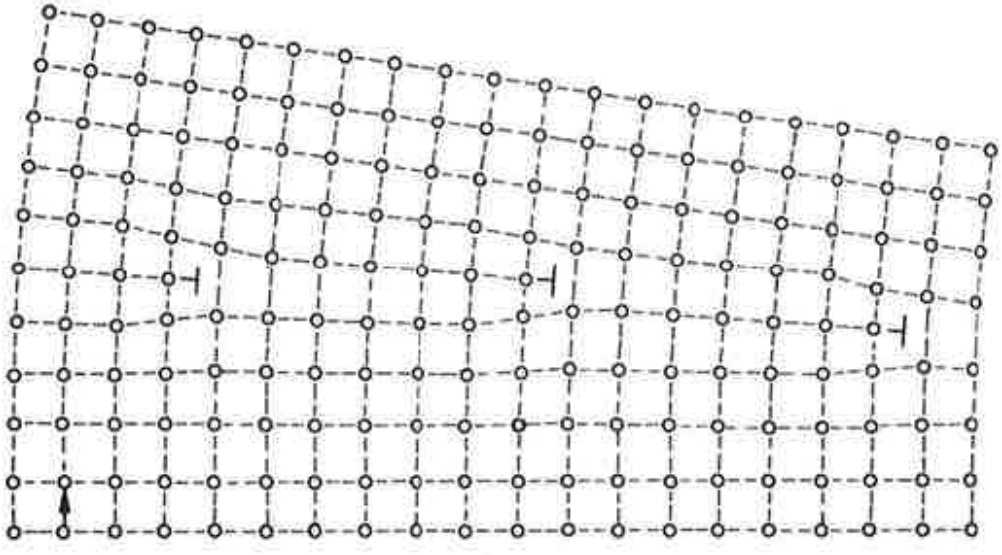

Fig. 14: A small angle grain boundary in a simple cubic structure, from [55].

Stress Concentrations on Triple Points

In a polycrystal, several types of stress concentrations can occur, stemming from triple grain junctions, slip bands impinging on a boundary and particles on sliding grain boundaries [11]. Such elastic stress concentrations on grain boundaries and triple points are a result of the discontinuity of elastic properties across the grain boundaries. The stress singularities can be high enough to cause local plastic deformation and can finally lead to damage [68]. Compared to a stress field of a crack tip, the singularity at triple junctions can be even higher at smaller angles, whereas at higher angles of the junction, the singularity will be weaker. The stress field near the junction of grain boundaries can be calculated starting from the Airy stress function, the solution of which can be found in ref. [11]. The maximum tensile stress occurs on the boundary normal to the applied stress. At elevated temperatures, diffusion and dislocation creep tend to relax such stress concentrations [11].

During power-law creep, the stress distribution is a power function of the distance to the triple point and the exponent has to be determined numerically. The local stress concentration is moderate. In the presence of diffusion, these concentrations are further reduced. During Coble creep, the stress distribution has a parabolic form [11].

3.1.6.2 Subgrains

Subgrains are grains, which are at least partly surrounded by small-angle grain boundaries. As already discussed in paragraph 3.1.4.4, their formation can be attributed to the fact that homogeneously distributed dislocations tend to form modulated structures, which, among others, result in the formation of sub-boundaries. The configuration is influenced by grain size, misorientation of the neighbouring grains and the activity of the glide systems. The equilibrium subgrain size depends on the dislocation density, which in turn is a function of the applied stress [1]. Fig. 15 shows a schematic former austenite grain with subgrains in its interior. Fig. 16 shows a former austenite grain boundary measured in the steel CB8 (15802h, 80MPa) done with the EBSD method [67].

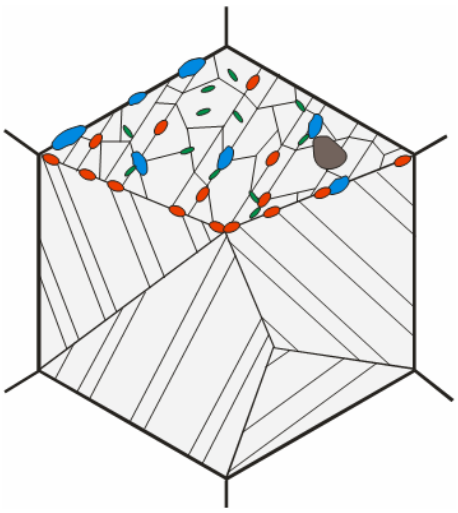

Fig. 15: Former austenite grain with martensitic substructure and precipitates.

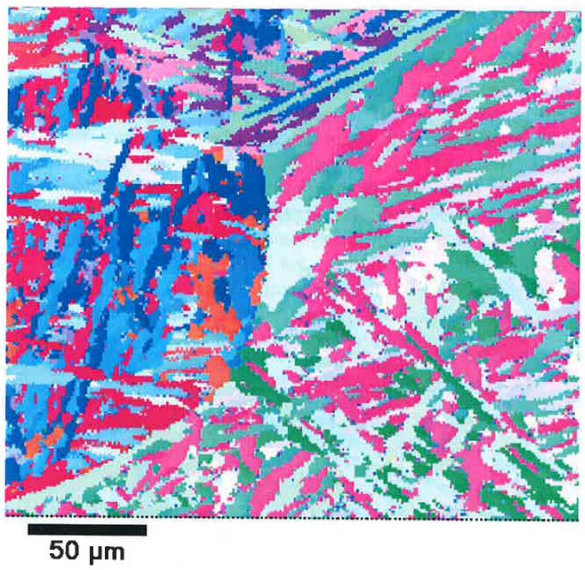

Fig. 16: Former austenite grain boundary. Different colours indicate different lattice orientations.

3.1.6.3 Precipitates

Precipitates, in general, have a different chemical composition and different physical properties than the surrounding matrix. They can have a larger or smaller bulk modulus, different lattice spacing or different crystallographic orientation etc. as the surrounding matrix.

Precipitates can be obstacles for conservatively moving dislocations. When such obstacles are impenetrable for dislocations, the moving dislocation has to bow out between the obstacles. If the stress acting on the dislocation loop is high enough, the dislocation can break free and successfully bypass the particle. The relevant parameter for this mechanism is the mean spacing L between the two obstacles. The minimum shear stress τ for the bypass condition is given by

$$\tau \approx \frac{Gb}{L} \tag{3.17}$$

where G is the shear modulus and b is the magnitude of the Burgers vector of the moving dislocation [36]. The smaller the spacing between the particles is, the higher is the shear stress. The mechanism is referred to as Orowan mechanism.

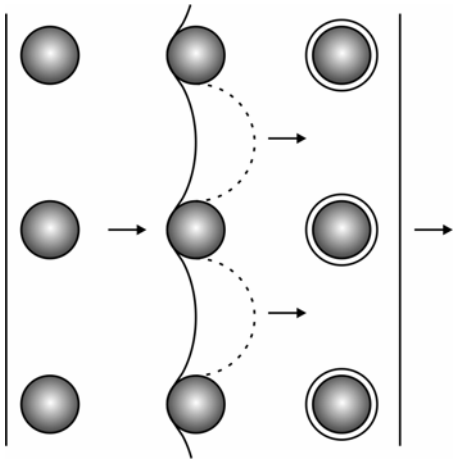

Fig. 17: The Orowan mechanism. The different lines show the different positions of the dislocation at different times.

From eq. (3.17), it is clear that a finer dispersion with a smaller mean particle spacing L will have a larger effect on hardening. The precipitation strengthening effect can be lowered, when the obstacle, e.g. a coherent precipitate, is weaker and can be cut by a dislocation, provided the acting stress is high enough. In this case, not only the particle spacing but also the maximum force, which can be sustained by the particle, plays a significant role as well [36].

At high temperatures, additional mechanisms for dislocation movement can become operative. They can move non-conservatively, that means they can climb or cross-slip. These processes are thermally activated and include the emission and absorption of vacancies. These additional mechanisms allow the dislocations to surmount precipitates and other obstacles. To reduce this effect at high temperatures, the obstacles should feature two properties. First, they should be as large as possible; second, they should exert some attractive or repulsive force to the dislocations to pin them.

The interactions between particles and dislocations can be incorporated in the so-called back-stress concept. The externally applied force is counteracted by microstructural components, such as precipitates. This counteracting dragging force is regarded as internal stress or back stress. Consequently, not the entire external load σ_{ext} acts as driving force for a deformation process; only the part, which exceeds the amount of inner stress σ_i, effectively contributes to creep and other phenomena. This effective creep stress can be expressed by

$$\sigma_{\text{eff}} = \sigma_{\text{ext}} - \sigma_i \,. \tag{3.18}$$

The inner stress can be regarded as a superposition of the contribution of all microstructural constituents. The part resulting from precipitates is described using the Orowan stress as stated in eq. (3.17). The part stemming from dislocations is dependent of the density of the mobile dislocations. If the resulting effective stress is below the threshold stress for the Orowan mechanism, the dislocations are pinned to the particles and the effective creep rate is significantly lowered [69].

Stress relaxation near precipitates

During nucleation and growth of precipitates, significant stress fields can build up within the precipitate and its closest surroundings due to misfit strains. These stresses can be relaxed by different mechanisms of matrix plasticity. These mechanisms include dislocation nucleation and movement on the one hand, on the other hand the diffusion of vacancies, which are generated at the precipitate/matrix interface, have to be taken into account. The Gibbs energy of the system acts as a driving force, where the total Gibbs energy includes the chemical Gibbs energy and the Gibbs energy provided by the elastic strain energy and the interface energy. Precipitate growth is influenced by this stress relaxation [70,71].

3.1.6.4 Evolution of the Microstructure

The microstructure of a material may not remain constant in time. The evolution and the changes in a microstructure are the result of phase transformations and interaction processes between structural defects [55]. Both processes are dependent on time, temperature and stress. The relationships and interactions lead to a complex genesis of the texture of a material. The properties of modern structural materials rely on its particular microstructure. Thus, the evolution of a microstructure in time is of major importance in materials science.

Grain growth and coarsening

Grain growth is a coarsening mechanism, which is motivated by a reduction of the total interface energy through minimization of the interfacial area. Due to this process, the subgrains, in general, will coarsen during creep. Especially at higher temperatures, a pronounced polygonisation of the structure can occur.

Two approaches for modelling the growth of subdomains can be distinguished. The first and widely used assumes that the wall velocity is proportional to the driving force. The proportionality constant is called the mobility. The driving force itself is a product of the curvature of the interface and its excess free energy. In this model, the growth law is of the type $\langle D \rangle^2 = \sigma \cdot t$, where $\langle D \rangle$ is the average domain diameter and t is time. Several modifications of this approach exist. In one, the driving force is assumed to be dependent on the boundary energy of the moving interface, the dependency of domain diameter on stress and time remains unchanged.

In other approaches diffusion phenomena are taken into account. Domain walls are assigned a width including variations of order-parameters and composition of the material. In other words, this structure is a non-uniform system. The resulting gradient concerning these different parameters represents the driving force for an atomic flux, hence for the motion of the interface [55].

External potential fields influence the driving force as well and, therefore, may result in microstructural changes. Temperature has an effect on the chemical potential. As a consequence, the diffusional processes are temperature-dependent. Stress fields can modify the atomic order in solid solutions and the precipitate morphology. Sufficiently strong magnetic and electric fields can affect the material as well.

Experimental evidence for microstructural changes of alloys can be found in numerous experiments. As an example, the microstructure of a creep-loaded sample of G-X12 as measured by Hofer [72] is shown in Fig. 18.

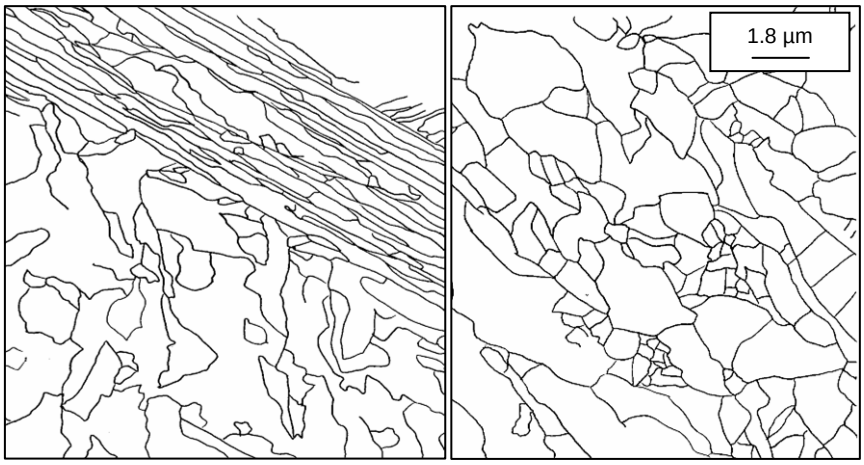

Fig. 18: Creep sample (shaft area) of G-X12 as measured by Hofer [72]. Left image: as received; right image: creep loaded at T = 650°C and σ = 80 MPa. Subgrain growth and grain coarsening is clearly observed.

Precipitation

Precipitation is a special case of phase transformation where, depending on temperature, elements, which are solute in the base metal, precipitate out of the solution. This process is driven by a reduction in Gibbs free energy [55]. The spatial dimensions of the emerging phase, referred to as precipitates, are relatively small compared to the embedding matrix phase.

In modern steel, a number of different types of precipitates will commonly occur. Precipitates at subgrain boundaries will stabilize the structure against microstructure coarsening, whereas precipitates within the bulk will influence the deformation resistance of the grain itself. Changes in the precipitate structure have a pronounced effect on the microstructural behaviour of the material and, during long-term creep loading, generally decrease the creep strength [73].

During creep deformation, precipitates may nucleate, grow, coarsen and dissolve. They can form within a grain or on defects in the crystal, such as grain boundaries, dislocations, stacking faults etc. Especially at lower under-cooling, these heterogeneous nucleation sites are preferred due to the smaller increase in elastic strain energy during formation of the nucleus

[55]. The forming of nuclei on these sites is a stochastic process and is usually treated in terms of probabilities. The growth of those nuclei, which reach a stable size, can then be described by deterministic rules, and is governed by diffusional processes [74].

The last stage of precipitation is coarsening. Many of the small precipitates will dissolve, whereas some larger ones remain stable and continue to grow until only a small number of large particles is remaining. This process is known as Ostwald ripening.
The evolution of the size distributions and number densities can be modelled by various numerical approaches, see [74].

In experiment, precipitates can be made visible using modern technologies such as TEM/EFTEM. In Fig. 19 a recording of such an experiment from Bernhard Sonderegger is shown. The sample contains laves phase (red), $M_{23}C_6$ (green) and vanadium nitrides (blue). A detailed chemical analysis of these three phases was conducted by EDX, the results are presented in [67].

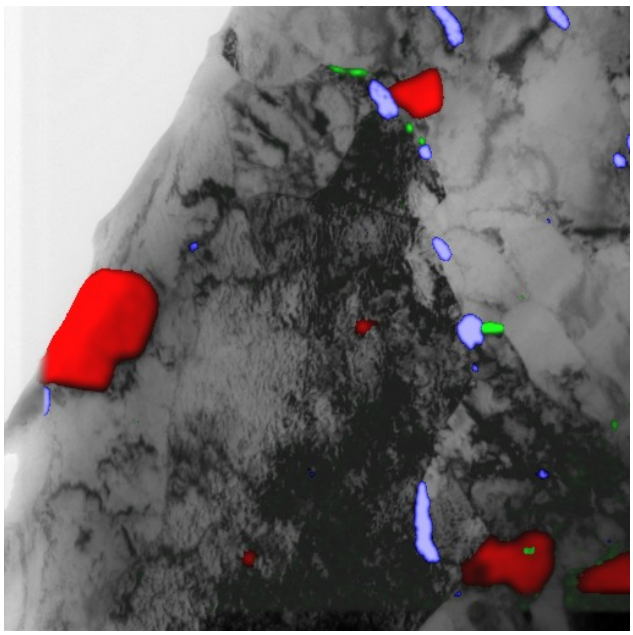

Fig. 19: Creep loaded sample (650°C, 110 MPa) of steel CB 8 with precipitates. The sample contains laves phase (red), $M_{23}C_6$ (green) and vanadium nitrides (blue) [67].

3.2 Models Implementing Creep Phenomena

To comprise creep phenomena, which have been introduced in section 3.1, and possible interactions in a quantitative sense, several models and mathematical frameworks have been developed. The range covers implementations solely describing the overall creep rate of a sample, mathematical frameworks including empirical or phenomenological descriptions, and spatially resolved models incorporating mutual interactions of different mechanisms. A selected overview is given in the next section.

3.2.1 General Approach

In high temperature creep, the creep rate $\dot{\varepsilon}$ for steady state creep is dependent on the applied stress σ, the temperature T and the shear modulus G through the relationship

$$\dot{\varepsilon} = A\frac{DGb}{kT}\left(\frac{b}{d}\right)^{p}\left(\frac{\sigma}{G}\right)^{n} \tag{3.19}$$

where D is an appropriate diffusion coefficient, b the Burgers vector, k Boltzmann's constant and d the grain size. The coefficients p and n and the dimensionless constant A have to be chosen in an appropriate way for each model [75]. When plotting $\dot{\varepsilon}$ versus σ with logarithmic axes, the slope of the curve reflects the value of n. Fig. 20 shows a typical result.

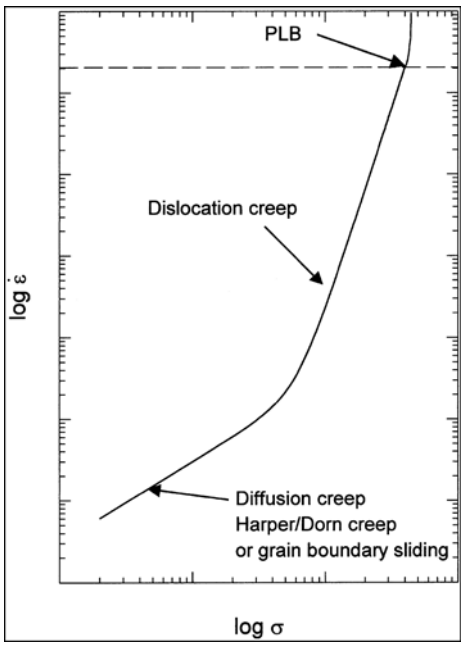

Fig. 20: Schematic, logarithmic plot of the variation of the steady state creep rate with the applied stress from [75].

In the plot, three different regimes can be distinguished. At relatively low stresses, experimental data follow a creep curve with n being approximately 1. This is generally

attributed to diffusional creep, Harper-Dorn creep and grain boundary sliding. At medium stresses, n is in the range of 3 – 6. This region is dedicated to dislocation creep or power-law creep. Dislocation glide is the rate controlling process for $n = 3$, whereas dislocation climb as a rate controlling mechanisms causes slopes with $n = 4.5$ to 6, where the actual value depends on the stacking fault energy of the material. The third regime can be found at very high stresses, the slope does not follow linear behaviour any more. This region is referred to as power-law-breakdown (PLB) and has been treated extensively in creep literature [75]. In the following sections, a brief review of the models based on these processes is given.

3.2.2 Models for Diffusional Creep

Diffusional creep was first treated theoretically by Nabarro [13] in 1948 and Herring [5] in 1950, and later by Coble [14] in 1963, where is the authors are considering different diffusion paths within the material: bulk (or volume) diffusion through the crystal lattice, diffusion in grain boundaries, diffusion over surfaces and diffusion along dislocations [3]. The rate at which atoms diffuse in the latter three is generally much higher than for bulk diffusion. The linear dependence on the applied stress is characteristic for all mentioned mechanisms.

3.2.2.1 Nabarro-Herring Creep

Nabarro and Herring independently derived expressions for diffusional creep [1,5,13]. Nabarro considered the change in concentration of defects near surfaces by acting on forces in a cubic crystal [13], whereas Herring used a gradient of a chemical potential to express the diffusional flux of atoms and vacancies in a polycrystal [5]. Both state that the diffusional flux of vacancies takes place via the grains of the polycrystal. This creep behaviour dominates at low stresses and high temperatures.

The strain rate is linearly dependent on the acting stress and inversely proportional to the square of crystal dimension d^2 [1] and it is expressed as

$$\dot{\varepsilon} = A_{\mathrm{NH}} \frac{D_{\mathrm{L}} \sigma \Omega}{d^2 kT} \tag{3.20}$$

where A_{NH} is a constant, which depends on the geometry of the grains, the grain size and load distribution. This constant usually has a value from 12 to 40, where these two values are considered to be the lower and upper theoretical limit for A_{NH}. The temperature dependence is determined by the lattice self-diffusion coefficient D_{L}. The atomic volume Ω can be estimated by

$$\Omega = 0.7 b^3 \tag{3.21}$$

where b denotes the length of the Burgers vector [28].

3.2.2.2 Coble Creep

Coble [14] argued that, at lower homologous temperatures, the main diffusion paths are the grain boundaries. Thus, in this temperature regime, grain boundary diffusion dominates over the lattice diffusion and the strain rate mainly depends on the grain boundary diffusion coefficient, as opposed to Nabarro-Herring creep [28].
Coble [14] derived the equation

$$\dot{\varepsilon} = A_C \frac{D_B \delta_B \sigma \Omega}{d^3 kT} \tag{3.22}$$

for spherical grains, where D_B is the grain boundary diffusion coefficient, δ_B is the effective grain boundary width and A_C is a constant with the approximate value $A_C = 150/\pi$ [23,28]. Other analyses suggest a value of about 18 for A_C [23]. The temperature dependence is determined by the grain boundary diffusion coefficient D_B. The creep rate again is linearly dependent on the acting stress and inversely proportional to the cube of crystal dimension d^3 [1]. For very small-grained material, an extended formula for Coble creep has to be used [24]. The diffusion coefficient for Coble creep is, strictly speaking, only valid for pure materials. For compounds, the grain boundary diffusivity has to be replaced by a more complex diffusivity, which includes the different single diffusivities, the composition and the grain boundary widths [3].

3.2.2.3 Expansion to Multi-Component Systems

Svoboda et al. [8] derive a mathematical formulation describing viscous creep for multi-component systems by diffusional processes, which includes non-ideal sources and sinks for vacancies. The system is assumed to contain n substitutional components and m interstitial components. A parameter α, which describes the rate, at which vacancies are generated, is derived from the thermodynamic extremal principle. A generalized creep equation is introduced as

$$\dot{\varepsilon} = \alpha \frac{\overline{\Omega}_0}{\overline{\Omega}} - \frac{\delta}{3}\left(\sum_{k=1}^{n} \frac{\left(\Omega_k - \overline{\Omega}_0\right)}{1 - N_0} div\vec{j}_k + \sum_{k=n+1}^{m+n} \Omega_k div\vec{j}_k \right) \tag{3.23}$$

where N_0 is the fraction of lattice sites occupied by vacancies and $\overline{\Omega}_0$ and $\overline{\Omega}$ are, respectively, the effective partial molar volume of the vacancies and the overall effective molar volume of all considered lattice sites. Ω_k represents the molar volume occupied by the species k, whereas $\vec{j}_k$ is the representative diffusive flux. These fluxes are dependent on the chemical potential, the diffusion coefficient and the molar fraction of the respective

component, as well as temperature. Further details on this generalized expansion can be found in ref. [8].

3.2.3 Models for Harper-Dorn Creep

Several theories exist to explain the features of Harper-Dorn Creep [49]. The starting point is usually given by the observation that the dislocation density in this creep regime is very low and independent of stress [50].

Ardell [49] proposes a model based on a network of dislocations for this creep process. It consists of the interaction of free, mobile dislocations and more or less stationary ones. The stationary dislocations form a network, which is coarsening by restricted glide and climb. The extent, to which such a network structure can coarsen, is limited, because a dislocation node can only be formed, if the sum of the Burgers vector of the intersecting dislocations equals zero. This process represents the recovery mechanism. Work hardening occurs by refining the network by mobile gliding dislocations. Both processes compete; equilibrium and steady state creep take place when both processes achieve a dynamic balance. The plastic straining during Harper-Dorn creep is due to the recovery process of the dislocation network. The dependence of the dislocation density on the specific material itself is explained by the limited number of slip systems available for coarsening of the network, while the dislocation density is not depending on the applied stress because the network stops to coarsen, when dislocations with specific Burgers vectors have disappeared. This limit is not depending on the applied stress [49].

Experiments show that the creep rate for Harper-Dorn creep is given by

$$\dot{\varepsilon} = A_{\mathrm{HD}} \frac{D_{\mathrm{L}} G b}{kT} \frac{\sigma}{G} \tag{3.24}$$

where A_{HD} is a constant, D_{L} the coefficient for lattice self diffusion, G the shear modulus, b the magnitude of the Burgers vector, k Boltzmann's constant, T the temperature and σ the acting stress [28].

The values of A_{HD} can be estimated from theoretical considerations. Nabarro [76] and other authors [77, 78,79] incorporate the Peierls stress into the calculation of A_{HD}. Nabarro states that, in equilibrium, the stress exerted by each dislocation on its neighbour equals the Peierls stress. The motion of these dislocations is then controlled by climb and the activation energy is that for self-diffusion.

Based on this hypothesis, Langdon et al. [28,80] model the constant A_{HD} with

$$A_{HD} = \frac{1.4\pi\left(\tau_p/G\right)^2}{-\ln\left(\tau_p/G\right)} \tag{3.25}$$

where τ_p is the Peierls stress and G is the shear modulus.

Wang [81] models Harper-Dorn creep by using a concept of Weertman [82]. Dislocations are generated by sources in parallel planes with spacing h. Dislocations with opposite sign on neighbouring planes can annihilate each other by climb. Steady state creep is reached when the emission of new dislocations equals the annihilation of dislocations. The resulting dislocation density depends on the balance of internal stress, applied stress and the Peierls stress. When the applied stress σ is higher than the Peierls stress, the dislocation density will depend on σ^2 and power-law creep will dominate. When the applied stress is lower than the Peierls stress, the dislocation density will only depend on the Peierls stress, which is a material parameter, and Harper-Dorn creep will dominate. For the resulting creep stress, Wang [81] again derives equation (3.24) with the constant A_{HD} defined by

$$A_{HD} = 1.4 \cdot \left(\frac{\tau_p}{G}\right)^2. \tag{3.26}$$

The value of τ_p/G is material dependent and can be modelled by

$$\frac{\tau_p}{G} = \frac{1}{1-\upsilon} \cdot \exp\left(-\frac{2\pi}{1-\upsilon} \cdot \frac{d}{b}\right) \tag{3.27}$$

where ν is Poisson's ratio and d is the spacing between slip planes. A list of observed and predicted values for A_{HD} can be found in refs. [81] and [28].

3.2.4 Models for Dislocation Creep

Numerous models of dislocation creep exist. Two main approaches can be distinguished, where the creep strain is considered as a result of (i) dislocation glide or (ii) dislocation climb. The former models (i), which assume dislocation glide as the main source for creep strain, can be divided into two sub-groups. The first sub-group states that the creep rate is controlled by climb and annihilation of edge dislocations, the second sub-group is founded on dislocation glide as rate controlling process. The latter approach (ii), which states that creep strain is the result of dislocation climb, in general ignores the contribution of dislocation climb to the creep strain. In the following section some of these models are briefly outlined, following the discussion of Čadek [1].

3.2.4.1 Earlier Weertman's Model

Weertman [83] assumes that the creep rate is controlled by climb, whereas the deformation itself is caused by dislocation glide. The dislocations are assumed to have a specific configuration; they are building dislocation pile ups as shown in Fig. 21.

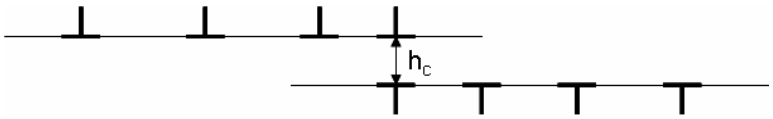

Fig. 21: Dislocation pile-up as suggested by Weertman [83]. The leading dislocations climb along the path h_c and annihilate.

The number of dislocations in each pile-up is dependent on the distance between Frank-Read sources. The leading dislocation is acted on by a force, which depends on the acting stress and the number of dislocations within the pile-up. Vacancies will flow between different pile-ups and will permit the leading dislocations to climb along the path h_c. When they finally meet, they are annihilated. The climb velocity is dependent on the acting force on the dislocation, which finally leads to the conclusion that the creep rate can be expressed by

$$\dot{\varepsilon} = A_{\mathrm{D}} \frac{D_{\mathrm{L}}}{b^{3.5} M^{0.5}} \frac{Gb^3}{kT} \left(\frac{\sigma}{G} \right)^{4.5} \tag{3.28}$$

where b is the magnitude of the Burgers vector, M the volume density of dislocation sources and A_D a constant to be determined. The activation energy is close to the activation energy of lattice diffusion [1]. Later, some objections where raised against this theory. They include that the dislocation configuration shown in Fig. 21 is unstable and that such pile-ups could not be observed in creep experiments. Furthermore, a fixed and stress-independent density of dislocation sources could not be supported by experiments. In a later version of this model, the assumption of dislocations climbing in groups but not forming pile-ups is incorporated, again leading to a stress exponent with the value 4.5 [1,84]. In the most recent version of the model, a stress-dependent density of Frank-Read sources was included, resulting in a creep rate proportional to σ^3 [1].

3.2.4.2 Models Involving the Role of Subboundaries / Subgrain Models

As already stated, dislocation have the tendency to form sub-boundaries. These sub-boundaries can act as regions where dislocation annihilation can take place. Weertman [85] considers the formation of pile-ups of dislocations on sub-boundaries. The basic idea is depicted in Fig. 22. If the approaching dislocation and the sub-boundary have the same Burgers vector (dislocation 1), the dislocation is inserted into the sub-boundary. Dislocation 2

has a Burgers vector with an opposite sign than those of the sub-boundary. After entering the boundary, it will annihilate by climb with one of the existing sub-boundary dislocations. By this mechanism, the overall number of sub-boundary dislocations remains constant; the spacing between the dislocations is adjusted by climb.

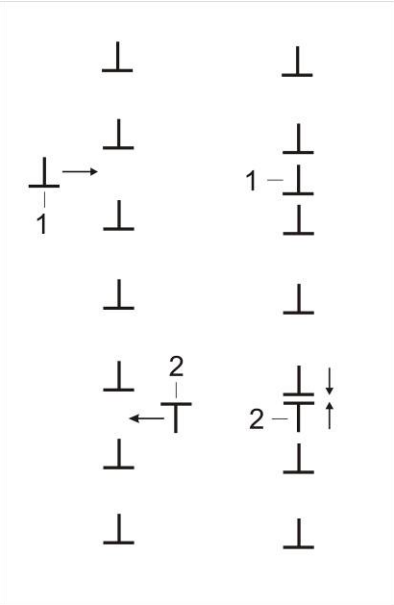

Fig. 22: Insertion and annihilation with dislocations of different signs in a sub-boundary.

Considering the mean spacing of the sub-boundary dislocations, the climb velocity of a dislocation within a sub-boundary, the time required for annihilation and the number of annihilated dislocation segments, Ivanov et al [86] modelled the resulting creep rate with

$$\dot{\varepsilon} = A_{\mathrm{SB}} \frac{D_{\mathrm{L}}}{b^2} \frac{G\Omega}{kT} \left(\frac{\sigma}{G} \right)^3 \tag{3.29}$$

where A_{SB} is a constant to be determined. This model predicts a creep rate dependent on the third power of stress.

Blum [87] modifies this model by assuming a finite sub-boundary thickness a in contrast to Ivanov et al. [86], who considered a zero thickness. Then, the number of annihilated dislocations in the sub-boundary is higher, and the creep rate is expressed by

$$\dot{\varepsilon} = A_{\mathrm{SB}} \frac{D_{\mathrm{L}}}{b^5} \frac{G\Omega}{kT} \left(\frac{\sigma}{G} \right)^3 . \tag{3.30}$$

Weertman [88] modifies a simple cell model, which consists of dislocation loops with edge and screw segments. The loop expands by glide and cross glide. The edge segments are stopped by other edge segments, the movement of screw segments is controlled by super-jogs.

Considering the lengths of the dislocation segments, the time required for dislocation annihilation by climb and the stacking fault energy of the material, the creep rate can be modelled by

$$\dot{\varepsilon} = A_{\mathrm{W5}} \frac{D_{\mathrm{L}}}{b^2} \frac{G\Omega}{kT} \left(\frac{\sigma}{G} \right)^5 . \tag{3.31}$$

where A_{W5} is a constant dependent, amongst others, on the density of the super-jogs and the stacking fault energy of the material.

3.2.4.3 Dislocation Climb Creep

Most models for power law creep assume that the creep strain is a consequence mainly of dislocation glide. In contrast to this, Nabarro [89] presents a model, where the creep strain is a result of climb of dislocations.

The model is based on the assumption that the dislocations, which are arranged into a network and form sub-boundaries, are perfect sources and sinks for dislocations. The individual links of this network bow out while they absorb or emit vacancies. As a result, their length and, hence, the dislocation density increase. This mechanism can be regarded as a dislocation source. The decrease of the dislocation density takes place by annihilation of links with opposite signs, which meet during climb.

To enable climb of the dislocation segments, a diffusive flux of vacancies is necessary. This flux and the mean link length lead to the creep rate

$$\dot{\varepsilon} = A_{\mathrm{N}} \frac{D_{\mathrm{L}}}{b^2} \frac{G\Omega}{kT} \left(\frac{\sigma}{G} \right)^3 . \tag{3.32}$$

where A_{N} is a constant and b the norm of the Burgers vector. Thus, Nabarro creep, which is controlled by lattice diffusion, is dependent on the third power of stress.

3.2.4.4 Model of Jogged Screw Dislocations

In models of this type, the creep rate is controlled by the glide of screw dislocations [1]. The mechanism is considered by many authors, including Mott [90], Raymond and Dorn [91] and Barrett and Nix [92].

The climb of jogs on screw dislocation is a non-conservative motion, which is connected with the emission and absorption of vacancies. Since a jog can be regarded as a short segment of an edge dislocation, the dragging force can be calculated in dependence of the vacancy concentration in the adjacent area. Calculating the velocities of the dislocations and considering the Orowan equation, one obtains the equation

$$\dot{\varepsilon} = 4\pi\beta l D_{\mathrm{L}} \frac{b^2}{a^3} \frac{Gb}{kT} \left(\frac{\sigma}{G} \right)^3 \tag{3.33}$$

where a is the lattice parameter, β is the number of atoms in the unit cell and l is the distance between the jogs of the screw dislocations.

3.2.4.5 Thermally Activated Glide and Diffusion Controlled Recovery

Models of this type are based on the assumption that glide processes and annihilation of dislocations are influenced by the heterogeneous structure of a material. As already outlined, dislocations tend to form substructures. As a consequence, soft and hard regions are created. The acting stresses are influenced by this substructure. In soft regions, long-range internal stresses reduce the acting stress, whereas in hard regions the acting stresses are increased. In addition, the mechanisms of dislocation motion are different in both regions. In soft regions, thermally activated glide processes occur to bypass obstacles, whereas, in hard regions, annihilation and rearrangement of dislocations is favoured to enable the required flow. Although these processes do not work independently, as a simplification, the strain rate can be written as sum of strain rates due to thermally activated dislocation glide and diffusion-controlled recovery. The thermally activated glide is dependent on the energy associated with the movement of the dislocation, the effective stress and the strength of the obstacles. The recovery-controlled strain rate is dependent on the time required for the climb and annihilation of two dislocations and the dislocation spacing. At low stresses, the creep rate is dominated by recovery. At high stresses, glide of dislocations will be the prevailing process. For recovery-controlled creep, the model again predicts the dependence of the strain rate on the third power of the acting stress [1,60].

3.2.4.6 Viscous Dislocation Glide in Solid Solution Alloys

In solid solutions, various mechanisms additionally influence the creep behaviour at high temperatures. The solute atoms form atmospheres around dislocations. During dislocation movement, this atmosphere must either be dragged by the moving dislocation or the induced short-range order must be destroyed by the moving dislocation.

Friedel [93] considers that the solute atoms near a dislocation are mostly situated in a minimum distance from the core. The dislocation core drag reduces the velocity of the dislocation. Taking into account the mean distance between the solute atoms and the density of the moving dislocations, Friedel derives the equation for the creep strain with

$$\dot{\varepsilon} = 2D_S \frac{Gb}{kT}\left(\frac{\sigma}{G}\right)^3 \tag{3.34}$$

where D_S is the diffusion coefficient of the solute.

Takeuchi and Argon [94] assume that a dragging force caused by the solute atoms acts both on dislocation climb and glide. This force is dependent on the velocity of the dislocation and the concentration of the solute in the dragged atmosphere. If the velocity for climb is much lower than the velocity of glide, the dislocations will behave similarly as in pure metals. If the dislocation motion is controlled by atmosphere drag, the glide velocity will be lowered and will be equally small for all motions. As a consequence, the formation of a significant substructure is inhibited, because the motion of free dislocation is as slow as the recovery of the interacting dislocations. Furthermore, numerous jogs will be created on edge dislocations, because the dislocation movement is not restricted to a specific glide plane and the internal stresses have a random distribution. Taking the rates of generation and annihilation of dislocations into account, Takeuchi and Argon obtained for the resulting creep rate the equation

$$\dot{\varepsilon} = D_S \frac{1}{8C_0\alpha^2}\frac{kT}{Gb^5}\left(\frac{\sigma}{G}\right)^3 \tag{3.35}$$

where α is a misfit parameter between the radii of the solute and the solvent atoms and C_0 is the solute concentration at an infinite distance from the dislocation.
The glide velocity of the edge dislocation will be the rate-controlling mechanism, because edge dislocations move slower then screw dislocations. The creep strain is the result of both mechanisms.

3.2.4.7 Precipitation Strengthened Alloys and the Back Stress Concept

If a microstructure subjected to creep conditions is acted on by an external force, this force can be counteracted by microstructural components as precipitates and interfaces. These components are causing a back stress (or inner stress) against the externally applied stress. Consequently, only a part of the external stress can act as a driving force for creep deformation. This concept is commonly denoted as the back stress concept. In this concept, the creep rate is dependent on the difference of the applied stress σ and the back stress σ_B, $(\sigma - \sigma_B)$, instead of the applied stress alone. To model this back stress, several approaches exist.

Several authors [95,96,97] perform an analysis accounting for passing obstacles by climb as the main process. The calculation of the effective spacing L of the dislocation line between the particles is a fundamental part of such models [1]. At zero applied stress, the dislocation line will be straight. When a stress is applied, the dislocation will bow out to a distinct radius of curvature. This radius depends on the acting stress and the dislocation line energy. Considering the total matrix area swept by the dislocation and the radii of the particles, the effective particle spacing can be calculated in dependence of the applied stress. The back stress then is dependent on the spacing of the particles and geometric relations between dislocation and particles.

3.2.4.8 Crystal Plasticity Within the Framework of Finite Elements

A number of models consider creep phenomena within the framework of finite elements. Mostly, the theory of crystal plasticity is utilized. In the theory of crystal plasticity, the concept of deformation by crystallographic slip is applied for calculating the accumulated creep strain [98,99]. The kinetics of dislocations is introduced by a flow rule, hardening effects are established using slip system hardening rules. Elastic anisotropy is considered as well [99].
These models, which are time- and space-discretised [98], were developed for a number of different materials and alloys [56,100,101,102], a few of them are outlined in the next sections.

McDowell

McDowell et al. [56,100] present a model for a duplex Ti-6Al-4V alloy based on a microstructure-sensitive crystal plasticity framework. This material is a dual-phase alloy consisting of an hcp primary α-phase and secondary lamellar α + β phase, which is composed of alternating layers of secondary α laths and bcc structured β laths [100]. The dual-phase nature of the material is considered in the grain orientation, the anisotropic yield strengths of the different slip planes and the non-planar nature of the dislocation cores [54]. The primary α phase has 24 possible slip systems, the secondary α + β-phase is modelled implicitly by an effective grain orientation, which includes both hcp and bcc slip systems. Back stresses and dynamic recovery are considered in the chosen type of flow law.

All grains are assumed to be cubic and to have the same size [56], the phases of each grain are randomly distributed. The model is calibrated by a fitting procedure, using the stress–strain response of tests at different strain rates with strain hold periods.

The results of the finite element simulations are given in effective plastic strains and feature a highly heterogeneous distribution of plastic strain. The authors claim the findings to be in reasonably good agreement with experiments.

Raabe

The conventional approach in crystal plasticity within the framework of finite elements deals with grain boundaries, which coincidence with the cell boundaries. One rare exception is the model introduced by Raabe and co-workers [101,102,103], which uses a special grain boundary element.

The model is introduced in two adaptations, one for fcc and one for bcc metals. The dislocation structure is segmented into two groups of dislocations. First, a homogenous distribution of randomly distributed or, as frequently termed, statistically stored dislocations is considered, which can either be mobile or immobile. The immobile dislocations accommodate the external plastic deformation, whereas the mobile dislocations are responsible for hardening. Second, a fraction of geometrically necessary dislocations is added. The evolution of both densities is tracked separately. The evolution laws for the statistically stored dislocations include annihilation by climb. The Orowan equation is used to calculate the plastic shear rate of each slip system as a function of the mobile dislocation density. The interaction between different slip systems is modelled using an interaction strength, which includes, amongst others, cross slip and glissile junctions. The evolution of the density of geometrically necessary dislocations is calculated using the Burgers vector and the derivative of the plastic deformation gradient [103]. In the vicinity of grain boundaries, an additional activation enthalpy for mobile dislocation is introduced into the rate equations. This additional term quantifies the probability for a dislocation to penetrate the grain boundary. The grain boundary itself is introduced as a separate grain boundary element containing the interface itself [102]. Temperature dependencies are included in a generic fashion.

To validate the model, simple shear experiments of Al single [103] and bi-crystals [102] are used. The constitutive parameters are obtained by fitting stress-strain curves. The local deformation is found to be in good accordance with experimental results.

Cheong and Busso

Cheong and Busso [104] present a rate-dependent crystal plasticity model for single phase polycrystal configurations. Deformation is the result of crystallographic slip, where the overall slip is calculated as the sum of slip rates of activated slip systems.
Forest dislocations (network of dislocations) are considered to act as an obstacle for moving dislocations. Deviations from the regular spatial arrangements of the dislocations are simulated by a statistical coefficient. The interactions between all dislocations are taken into account by a dislocation interaction matrix. Dislocation densities are accounted for screw and edge dislocations separately.

The generation of dislocation is ascribed to Frank-Read sources. The expanding dislocation loops are assumed to be rectangular with edge and screw sides. The increase in the length of the dislocation segments causes a change in the respective dislocation density. As predominant annihilation mechanisms in this model, interactions between dislocations of the same character but opposite sign are introduced. The probability of an annihilation event during a distinct time interval is determined first, by the area the moving dislocation passes within this time interval and, second, by the critical distance for an annihilation between two dislocations to take place. For both screw and edge dislocations, different expressions are derived, due to the fact that edge dislocations cannot cross-slip.

The calibration of the parameters is done by using data from a Cu single crystal experiment. Furthermore, the behaviour of a Cu multi-crystal during creep is simulated. Slip behaviour and influences on the misorientation of the grains are studied.

3.3 Creep Modelling Using the Finite Element Method

For a better comprehension and a possible future upgrading of the model introduced in chapter 4, the basic finite element equations are briefly outlined in the following sections. Knowledge of matrix algebra is assumed throughout this work.

3.3.1 Time-Dependent Creep Modelling

In general, the material response to a given load or stress can be divided into four different regimes depending on time dependency and reversibility. Creep is time-dependent and not reversible and, thus, belongs to the visco-plastic phenomena as stated in Table 1.

Table 1: Overview on material behaviour in terms of deformation theory.

	time-dependent	reversible
elastic	✗	✓
plastic	✗	✗
visco-elastic	✓	✓
visco-plastic	✓	✗

CREEP

Because of the time-dependency of visco-plastic behaviour, the calculation of the stresses and strains has to be done step by step. The solution, in general, will be path dependent. For the description of the problem, some constitutive relations and assumptions have to be set up. The total strain $\boldsymbol{\varepsilon}$ can be separated into elastic $\boldsymbol{\varepsilon}^{el}$ and inelastic components $\boldsymbol{\varepsilon}^{in}$ by

$$\boldsymbol{\varepsilon} = \boldsymbol{\varepsilon}^{el} + \boldsymbol{\varepsilon}^{in}. \tag{3.36}$$

The inelastic components include plastic strain, viscoplastic strain and creep. The elastic part can be described by Hooke's law.

3.3.2 Finite Elements in Structural Mechanics

Mesoscale methods, such as finite elements, are continuum approaches. They are not intrinsically calibrated and, thus, can span larger time and length scales [66].
Two types of formulations exist. Lagrangian elements follow the material deformation; free and moving boundaries can be treated automatically. Eulerian elements are not attached to the material, but have a fixed grid. This description is a valuable tool for large deformations and fluid dynamics. But for small deformation, the Lagrangian description is advantageous and is widely applied. Therefore, this concept is used in this work [105].

3.3.2.1 Formulation of the Mathematical Framework and Basic Relationships

The displacement-based finite element method consists of an idealization of the spatial structure (specimen, sample) into an assemblage of elements [105]. A typical finite element consists of nodes and straight line boundaries. The nodal displacements $\mathbf{u}$ are summarized in a vector [106]

$$\mathbf{u} = \begin{Bmatrix} u_1 \\ \vdots \\ u_i \end{Bmatrix}. \tag{3.37}$$

In a three dimensional analysis, each node consists of three displacements, whereas in two dimensions only two displacements are comprised in the vector. The displacements $\hat{\mathbf{u}}^e$ at any point within the element can be calculated using the displacements $\mathbf{u}^e$ at the nodes of the element by

$$\hat{\mathbf{u}}^e = \sum \mathbf{N}\mathbf{u}^e \tag{3.38}$$

where **N** is the displacement interpolation matrix [105], which includes the so-called displacement shape functions [106]. The shape functions have to be chosen such as to give the appropriate nodal displacements when the coordinates of a corresponding node are inserted.

3.3.2.2 Strains and Stresses

The strains can be calculated at any point of the element provided that all the nodal displacements are known. This relationship can be written as

$$\boldsymbol{\varepsilon} = \mathbf{B}\mathbf{u} \tag{3.39}$$

where the matrix strain displacement matrix **B** is an operator, which contains all necessary geometrical information of the element. The size of **B** is dependent on the type of element, the number of nodes and the degree of freedom at each node. For a quadrilateral, four nodded element in two dimensions, **B** equals [106]

$$\mathbf{B} = \begin{bmatrix} \frac{\partial N_1}{\partial x} & 0 & \frac{\partial N_2}{\partial x} & 0 & \frac{\partial N_3}{\partial x} & 0 & \frac{\partial N_4}{\partial x} & 0 \\ 0 & \frac{\partial N_1}{\partial y} & 0 & \frac{\partial N_2}{\partial y} & 0 & \frac{\partial N_3}{\partial y} & 0 & \frac{\partial N_4}{\partial y} \\ \frac{\partial N_1}{\partial y} & \frac{\partial N_1}{\partial x} & \frac{\partial N_2}{\partial y} & \frac{\partial N_2}{\partial x} & \frac{\partial N_3}{\partial y} & \frac{\partial N_3}{\partial x} & \frac{\partial N_4}{\partial y} & \frac{\partial N_4}{\partial x} \end{bmatrix}. \tag{3.40}$$

All strains are summarized in a so-called pseudovector, which consists of the normal and the shear components of the strain tensor, which contribute to the internal work [105,106]. In two dimensions, this vector consists of three components

$$\boldsymbol{\varepsilon} = \begin{Bmatrix} \varepsilon_x \\ \varepsilon_y \\ \gamma_{xy} \end{Bmatrix} \tag{3.41}$$

where ε_x and ε_y are the normal components and γ_{xy} is the shear component.

Stresses are caused by the change in the actual strains. Any initial strains $\boldsymbol{\varepsilon}_0$, which can be caused by e.g. temperature, don't contribute to stresses have to be subtracted from the actual strains. Furthermore, any initial stresses $\boldsymbol{\sigma}_0$ due to material history have to be added on to the general definition. Assuming linear elastic behaviour, the stresses can be calculated by

$$\boldsymbol{\sigma} = \mathbf{D}\left(\boldsymbol{\varepsilon} - \boldsymbol{\varepsilon}_0\right) + \boldsymbol{\sigma}_0 \tag{3.42}$$

where **D** is the well-known elasticity matrix, which contains the usual isotropic stress-strain relationships. For plane strain analysis, **D** takes the form [105]

$$\mathbf{D} = \frac{E(1-\upsilon)}{(1+\upsilon)(1-2\upsilon)} \begin{bmatrix} 1 & \frac{\upsilon}{1-\upsilon} & 0 \\ \frac{\upsilon}{1-\upsilon} & 1 & 0 \\ 0 & 0 & \frac{1-2\upsilon}{2(1-\upsilon)} \end{bmatrix} \tag{3.43}$$

where E is Young's modulus and ν is Poisson's ratio.

3.3.2.3 Forces and Loads

Each force and distributed load must contain the same number of components as the corresponding displacement vector **u**. Furthermore, each component has the appropriate, corresponding direction.

The distributed loads **b** are defined as loads acting on a unit volume of material, the force $\mathbf{F}_b$ due to those loads can be calculated by [106]

$$\mathbf{F}_b = -\int_V \mathbf{N}^{\mathrm{T}} \mathbf{b} \mathrm{d}V \,. \tag{3.44}$$

The forces $\mathbf{F}_0$ due to initial strains $\boldsymbol{\varepsilon}_0$ and stresses $\boldsymbol{\sigma}_0$ can be calculated by

$$\mathbf{F}_0 = -\int_V \mathbf{B}^{\mathrm{T}} \mathbf{D} \boldsymbol{\varepsilon}_0 \mathrm{d}V + \int_V \mathbf{B}^{\mathrm{T}} \boldsymbol{\sigma}_0 \mathrm{d}V \,. \tag{3.45}$$

All forces mentioned above must be taken into account when establishing the equation system for the problem. If a boundary is subjected to an external load **t** per unit area, then the load term

$$\mathbf{F}_t = -\int_A \mathbf{N}^{\mathrm{T}} \mathbf{t} \mathrm{d}A \tag{3.46}$$

has to be added.

3.3.2.4 Stiffness Matrix and Resulting System

In the framework of the Finite Element Method, the stiffness matrix describes geometrical and physical properties of the spatial structure to be modelled. The stiffness matrix has to be calculated for each finite element of the element assemblage separately. Each element has its own element number and a list of its nodal points. The stiffness matrix of an element will always be square. The coefficients of the element stiffness matrix $\mathbf{K}^e$ are calculated by

$$\mathbf{K}^e = \int_V \mathbf{B}^{\mathrm{T}} \mathbf{D} \mathbf{B} \mathrm{d}V \,. \tag{3.47}$$

The global stiffness matrix **K** is assembled of all element matrices by

$$\mathbf{K} = \sum_i K_i^e \tag{3.48}$$

Every sub-matrix has to be inserted according to the coordinates of its nodal points. Each of these matrices contributes in an additional sense, which means that, for each coefficient, the attributions have to be summed up that is all numbers in the appropriate space of the global matrix have to be summed up. As all matrices are symmetric only the upper half above the diagonal has to be considered [105,106].

3.3.2.5 Boundary Conditions

There are two types of boundary conditions. In structural analysis, these consist of prescribed displacements and prescribed acting forces. The displacement boundary conditions are also called essential or Dirichlet boundary conditions. The force boundary conditions are also called natural or Neumann boundary conditions.

The force boundary conditions are calculated by the external nodal point force vector. They include all the external forces loaded on the specimen. Such a boundary loading is represented by concentrated forces acting on the boundary nodes.

The displacement boundary conditions simply specify the value that the nodal displacement at a specific point needs to adopt. A minimum number of displacements has to be prescribed because the displacements cannot be only determined by the acting forces. Physically, this is obvious because the structure should be prevented from rigid body movements. Mathematically, the matrix **K** would become singular. It should be noted that, if, at a node, the displacement is prescribed, the external forces at this node cannot be prescribed and must remain unknown [105,106].

3.3.2.6 System of Equations

The stiffness matrix **K**, the nodal displacements **u** and the force vector **F** finally add up to

$$\mathbf{K}\mathbf{u} = \mathbf{F} \,. \tag{3.49}$$

The solution of this system of equations involves of the calculation of the unknown resulting displacements **u** at all nodes of each element. The stresses and internal forces are then obtained from these calculated displacements [105,106].

4 Numerical Implementation

In this chapter, the creep model launched in this work is introduced in detail. The individual sections discuss the general methodology of the approach, as well as the individual physical mechanism operating during creep loading of a poly-crystalline structure. The chapter is concluded with a description of the code implementation and a discussion of the problems and difficulties observed when treating a complex structural problem numerically using the Finite Element Method.

4.1 Design of the Spatially Resolved Creep Model

As a first step, the spatial range covered by the presented model is specified, the physical mechanisms representing the basic model ingredients are introduced and potential interactions are described.

4.1.1 Multi-Scale / Multi-Phase Approach

The presented model introduces different microstructural features and their interactions. These ingredients span different length and time scales. To give an overview on the scale used, as a typical example, the behaviour of solids on different spatial levels is examined as shown in Fig. 23.

The first level is the engineering level, where structures and assemblages are analysed on a macroscopic scale. The material is considered to be homogeneous in sufficiently large volumes. The evolution of material parameters, such as deformation, is described without explicitly taking into account the underlying physical mechanisms. The length scale ranges down to millimetres. The scope of this work is far below this level and, therefore, macroscopic interactions are omitted in the model.

The second level is the mesoscopic level. This length scale takes into account the internal structure of the material. In our case, the arrangement consists of grains, their martensitic substructure, grain boundaries and precipitates. In modelling, the local properties are taken into account by assigning a set of different properties to each of these microstructural components. The length scale ranges from micro- to nanometers. The model introduced in this work includes the microstructure, its properties and interactions within this length scale.

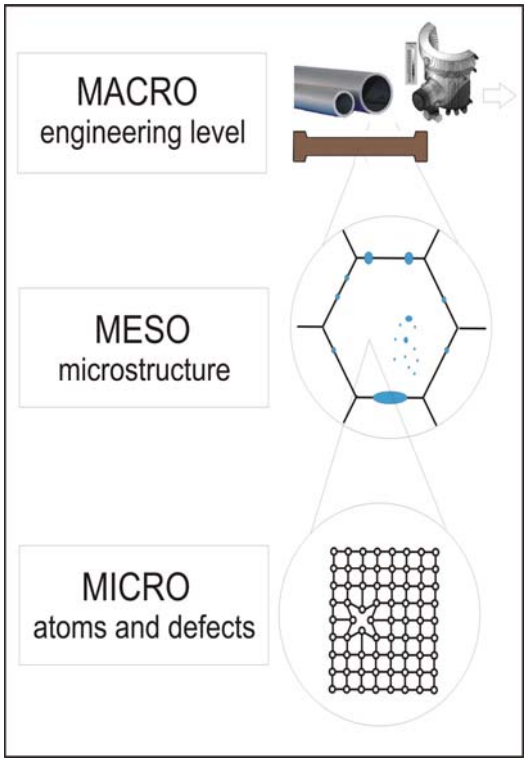

Fig. 23: Macroscopic, mesoscopic and microscopic length scales with examples.

The microscopic level consists of atomic structures and their interactions. In creep modelling, this concerns microstructure constituents such as vacancies and dislocations. Their reactions and interactions within the material comprise e.g. vacancy migration, dislocation movement and pinning of dislocations at obstacles. These interactions determine the response of a material to prescribed conditions, such as mechanical stress or elevated temperature. Diffusional processes and, thus, mass transport, are occurring. The resulting mass flux caused by migration of structural vacancies is incorporated into the presented model and determines the deformation of the material, whereas the resulting creep strains and stresses are calculated at the mesoscopic level.

4.1.2 Spatially Resolved Microstructure

To reflect the impact of a microstructure on creep behaviour, the presented model represents a particular microstructure and its reactions in terms of stresses and strains on external influences. The microstructure of metallic materials and its influence on creep is complex. Therefore, the model consists of several elements, including grains, their substructures, high angle and low angle grain boundaries, precipitates, dislocations and vacancies. The characteristics of the material are, in addition to its chemical composition, controlled by the properties of these microstructural components and their particular arrangement. This local arrangement of different constituents and their interactions lead to a highly heterogeneous

response to externally applied loads of the affected material in terms of internal stresses and creep strains.

The intention of the implemented work is to reflect the influence of this locally differing microstructure on the overall material behaviour during creep. The microstructure is represented by a spatially resolved section of a creep-loaded sample as represented in Fig. 24. On the chosen length scales, the incorporated microstructural elements consist of

- the matrix of the grains,
- grain boundaries,
- precipitates, both on grain boundaries and within the matrix,
- the mass flux caused by vacancy migration.

As already stated, the main focus in the presented work lies on creep deformation caused by diffusion. For the benefit of generality, the deformation caused by moving dislocations is already implemented indirectly into the model by a simple power-law constitutive formulation, though. Explicit treatment by, e.g., dislocation dynamics, is beyond the scope of this work. However, the inherent option to do so, provided by the model architecture, adds a valuable possibility to upgrade and expand the model in the future.
Each of the mentioned microstructural elements (grain boundary, bulk, precipitate etc.) is characterized by a number of properties, including

- grain orientation,
- grain structure (fcc, bcc or hcp structure),
- Young's modulus,
- Poisson's ratio,
- yield and threshold stresses,
- diffusion coefficients,
- and activation energies.

In this work, the main focus lies on the elastic modulus, Poisson's ratio and diffusion coefficients. An overview on the basic features of the model is given in Fig. 24 and the following paragraphs. A detailed discussion of the properties of these elements and of their actual implementation is given in the subsequent sections.

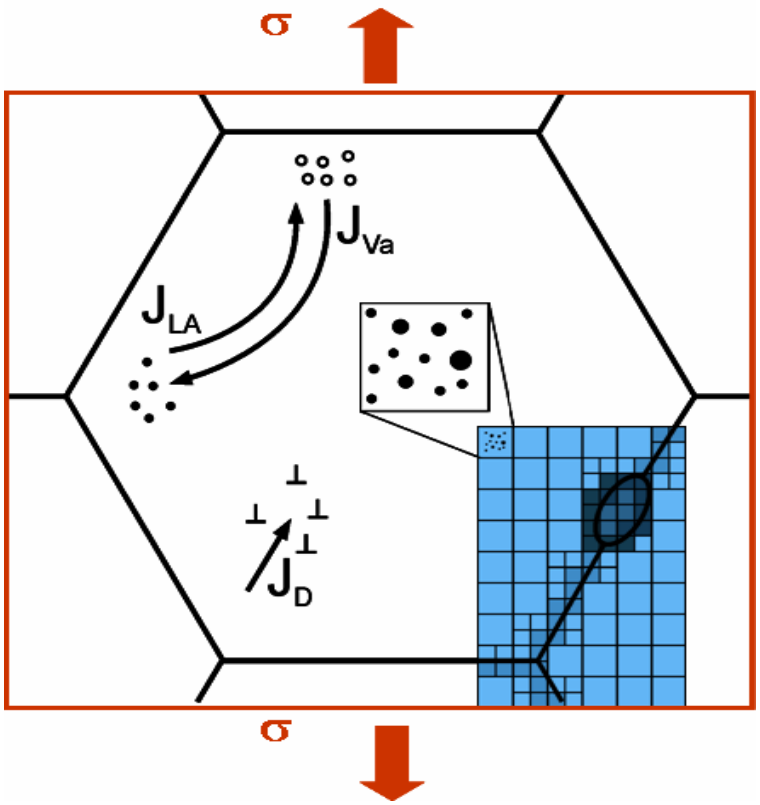

Fig. 24: The spatially resolved microstructure, represented by a grain with vacancies, dislocations, fine and coarse precipitates. The mathematical discretisation is indicated as well.

In this model, the matrix is assumed to have a homogeneous, crystalline structure. In general, the different grains have different crystallographic orientations. Adjacent grains are separated by high angle grain boundaries. Grain boundaries are considered as a separated, distinct element in the calculations. Due to their amorphous structure, the properties of grain boundaries are different from that of the grain itself, in particular, the elastic modulus and the diffusion coefficient. Precipitates are either introduced as a fine dispersion within the matrix, which will alter the properties of the respective region, or they form relatively coarse, hard particles. In this case, the precipitate is regarded as a discrete region within the bulk material, either within the grain directly or on grain boundaries.

The structure, as given by Fig. 24, is then discretised into cells. Each cell is described by a set of parameters depending on the microstructural element it represents. Again, the details of the incorporation into the model will be given in the following sections.

The basic mechanisms for creep deformation (Fig. 24) consist of material transport by vacancies and plastic deformation by dislocation movement. The local vacancy concentration is determined by the given stress distribution. The resulting flux of vacancies J_{VA} is described

by Fick's first law, as introduced in section 3.1.2.1. This flux is connected to a flux of lattice atoms J_{LA} in the opposite direction, which again is depicted in Fig. 24. The basics of these diffusional processes have been introduced in chapter 3.1.2. As already outlined, these fluxes are linearly dependent on the acting forces. The associated deformation rate $\dot{\varepsilon}$ of the material, therefore, is linearly dependent on the acting stress as well, expressed by

$$\dot{\varepsilon}_{\mathrm{NH}} \cong J_{\mathrm{LA}} \cong \sigma \,. \tag{4.1}$$

For the material fluxes due to dislocation movement, the situation is different. The material deformation caused by dislocation movement has a non-linear dependency on the acting stresses σ given by

$$\dot{\varepsilon}_{\mathrm{D}} \cong J_{\mathrm{D}} \cong \sigma^{n} \tag{4.2}$$

where n is the so-called stress exponent. The value of n depends on the type of dislocation movement, an introduction is given in chapter 3.1.4.

For both kinds of fluxes, this relationship has to be specified and a distinct relation between acting stresses and the resulting fluxes has to be introduced into the model. In this work, the main focus lies on Nabarro-Herring creep, which can be expressed by

$$\dot{\varepsilon} = A_{\mathrm{NH}} \frac{D_{\mathrm{L}} \sigma \Omega}{d^{2} k T} \tag{3.19}$$

with A_{NH} being a constant, D_{L} being the self-diffusion coefficient, Ω the atomic volume, d the grain size, k Boltzmann's constant and T the temperature.

4.1.3 Interactions

All microstructural elements and processes to be incorporated into this model interact with each other. A basic overview of all possible interactions is given in Fig. 25 and briefly discussed in the following. Part of these are already implemented and applied in the actual implementation, others can be introduced in the future to extend the capabilities of the model. The implementation of these interactions can be carried out in several ways, depending on the particular mechanism as discussed subsequently.

High angle grain boundaries are strongly interacting with all other microstructural constituents. They act as sources and sinks for vacancies, their major role in threshold behaviour of diffusional creep already having been discussed in chapter 3.1.2. Furthermore, they act as fast diffusion paths in the Coble creep regime due to their unordered atomic

structure. For dislocation movement, grain boundaries can, on the one hand, act as obstacles. On the other hand, they can provide dislocation sinks and sources, although Frank-Read sources are commonly stronger sources.

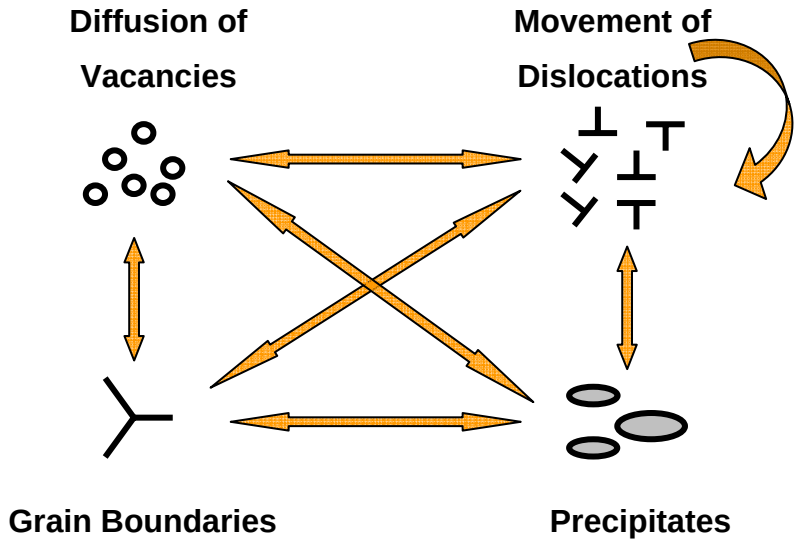

Fig. 25: Possible interactions of different microstructural elements.

For precipitates, grain boundaries represent a favourable nucleation site, here again the causes lie within the amorphous arrangement of atoms, which strongly facilitates precipitate nucleation.

A major role, although not indicated in this diagram, is the one that grain boundaries play in altering the stress distribution in the adjacent grains and forming stress concentrations near triple points. Details can be found in chapter 3.1.6.1.
Vacancies and dislocations are interacting as well. Dislocations emit and absorb vacancies when they move non-conservatively, i.e. during climb. Depending on the availability of vacancies, this mechanism can be the rate limiting process of creep deformation controlled by climb. Concerning dislocations and particles, climb and glide play an important role as well. On one hand, fine dispersed particles can be obstacles for dislocation glide. To bypass them, a dislocation has to climb, a process, which requires extra work and long-range diffusion. On the other hand, small particles can be a source for dislocation production (Frank-Read source), provided that the local stress exceeds a given threshold.

4.2 Physical Modelling

4.2.1 Modelling Creep Strain and Stress

The heterogeneity of creep strains and stresses is a consequence of the locally differing properties of the microstructure. These properties influence stresses or creep strains directly. Because of the mutual reactions within the physical system of the structure, the results and effects in terms of strains and stresses are coupled. In terms of creep modelling, their implementation takes place at different places within the setup of the model, depending on the particular mechanism, as outlined in the next section.

On the one hand, the creep strain is dependent on the locally acting stress. This stress is the response of the mesoscopic system to specific boundary conditions. If the properties of the system are homogeneous, the reacting internal stresses are homogenous as well. Since the microstructure of a polycrystalline material is far from being homogeneous, the reacting stresses will also have a non-homogeneous distribution within the material.
In the presented model, two specific properties of the microstructure are responsible for this observation: the Young's modulus E and Poissons ratio ν. Both properties are implemented into the model by introducing them directly into those equations of the model, which describe the interactions between applied forces, resulting displacements and internal reacting stresses. This is done by using the so-called elasticity matrix **D** [106]

$$\mathbf{D} = \frac{E(1-\upsilon)}{(1+\upsilon)(1-2\upsilon)} \begin{bmatrix} 1 & \frac{\upsilon}{1-\upsilon} & 0 \\ \frac{\upsilon}{1-\upsilon} & 1 & 0 \\ 0 & 0 & \frac{1-2\upsilon}{2(1-\upsilon)} \end{bmatrix} \tag{3.41}$$

to calculate the reacting stresses $\boldsymbol{\sigma}$ with

$$\boldsymbol{\sigma} = \mathbf{D}\boldsymbol{\varepsilon}^{\mathrm{el}}. \tag{4.3}$$

That is, the reaction itself of the structure on given conditions is altered directly. The resulting plastic strain is calculated in subsequent parts of the code.

The second possibility to influence the creep strain in the simulations is to change the proportionality constants, which link a given stress and the resulting mass flux and creep strain, respectively. In other words, not the driving force itself is changed, but the reaction of the system on this specific, given force is altered. For instance, the same stress distribution

leads to different mass fluxes, if the diffusivities of atoms are different. An increasing temperature initiates faster movement of particles, even when the stress level remains unchanged. The same holds true for other factors as well, which include

- diffusion coefficients,
- vacancy densities,
- temperature,
- shear modulus and
- dislocation densities,

where the former two are the most relevant ones in this model. These quantities, here for generality termed A, are introduced directly into the calculation of the creep deformation with

$$\Delta\varepsilon \cong A\bar{\sigma}^{n}\Delta t \tag{4.4}$$

where $\Delta\varepsilon$ is the strain increment, $\bar{\sigma}$ is the effective stress, n is the stress exponent and Δt is the time increment. The stresses are not influenced by the parameters A. Each phase implemented into the model can have parameters of both kinds. In the next section, a detailed description is provided.

Strain and Time Hardening

Time and strain hardening models provide simple empirical descriptions of creep phenomena [107]. In strain hardening models, the strain rate depends on the actual stress and the accumulated creep strain, which can be expressed by

$$\dot{\bar{\varepsilon}} = A\bar{\sigma}^{k}\bar{\varepsilon}^{l} \tag{4.5}$$

where A, k and l are constants to be chosen properly. Time hardening models postulate a relationship between the equivalent creep strain, the equivalent stress and the time at a fixed temperature with

$$\bar{\varepsilon} = A\bar{\sigma}^{n}\bar{t}^{m} \tag{4.6}$$

with the parameters A, m and n, which, again, have to be chosen properly.
In the actual framework, time hardening is already implemented, though not used in the presented simulations.

Threshold behaviour

Some mechanisms, which are acting as driving force for material transport, must overcome a certain activation energy or an activation barrier Q_{barrier} before they start to be operative. This condition can be expressed by

$$\dot{\varepsilon} \cong \begin{cases} A\sigma^n & Q \geq Q_{\text{barrier}} \\ 0 & Q \leq Q_{\text{barrier}} \end{cases} \tag{4.7}$$

where Q is the actual value and Q_{barrier} is the minimum energy, which has to be reached to initiate the process.

In this model, the threshold stress for creep deformation is regarded as such a barrier. It controls the onset of creep deformation, but its magnitude does not influence the material fluxes or the strain rate itself. The implementation in the model is rather simple. If a condition, as stated in equation (4.7), is met, the creep calculation is performed for the concerned phase. Otherwise, the change in creep strain is set to zero and only elastic response is calculated.

For diffusional creep, the threshold stress, albeit existent, does not play an important role because creep loading commonly occurs on levels clearly beyond its level. Therefore, its threshold value is set to zero for all simulations.

4.2.2 Modelling Phases

4.2.2.1 Bulk Grain

In this model, the grain interior is presumed to be homogeneous and to have the same lattice orientation over the entire subgrain. The main parameters related to the grain bulk volume are the elastic modulus E, Poissons ratio ν and the vacancy or mean lattice diffusion coefficient D_L.

The elastic modulus is grain size dependent for small grains. For grains larger than 20 nm, the elastic modulus can be taken as constant [108]. Thus, Young's modulus is chosen to have the same value for the entire matrix, with the actual values taken from literature [66]. Poisson's ratio is assumed to be constant as well.

The incorporation of both parameters into the model takes place in equations (3.41 and (4.3).

4.2.2.2 Grain Boundaries

High Angle grain boundaries, although assumed to have the same chemical composition, because we are neglecting segregation effects presently, have different properties than the bulk material. In contrast to the ordered, crystalline phase of the matrix, their structure is highly disordered. Therefore, grain boundaries can be regarded as an amorphous phase.

In the present model, grain boundaries are implemented as a homogeneous material without any specific crystal lattice orientation. Furthermore, the stress-strain response of a grain

boundary is not the same as in the surrounding lattice. The reason lies in the different strength of the disordered phase. Therefore, for grain boundaries, an elastic modulus different from that of the bulk material is utilized in the model.

Because there is no data available for amorphous pure metals, the properties of a grain boundary can be approximated by the values of the metallic glass in glass-forming systems and some theoretical considerations. Carsley et al. [109] approximate the shear modulus of the amorphous metal Gallium to be half that of the crystalline one. Schuh et al. [110] state that both, shear modulus and Young's Modulus, are about 30% smaller than that of the crystalline phase. The density of the material and the interatomic spacing differ only slightly (0.5-2.0%), so this cannot be an adequate, single reason to explain the decrease in those two moduli. Weaire et al. [111] assume that the local atomic displacements on straining are different because of the slightly different atomic spacing. This gives way to internal rearrangements that reduce Young's modulus and the shear modulus considerably.

For this reasons, the Young's modulus for grain boundaries E_{GB} is modelled with

$$E_{GB} = \frac{E_{\mathrm{c}}}{2} \tag{4.8}$$

where E_{c} is the modulus for the crystalline phase. Poisson's ratio is assumed to have the same value as the bulk. The width of the grain boundary is assumed to be 1 nm [112].

The implementation takes place in the same way as for the matrix phase. The elastic modulus is incorporated into the stiffness matrix of the element, and affects the stress response of the material to an existing strain as stated in equations (3.41) and (4.3).

4.2.2.3 Precipitates

To incorporate precipitates into the model, two different length scales are distinguished. Small precipitates within the bulk material are included into the model as a fine dispersion of particles. They are not introduced as separate cells, but alter the properties of a matrix cell. These precipitates have two effects on the creep determining stress distribution. First, the mean elastic modulus E of the lattice is higher than in unaffected material. The extent is dependent on the fraction f_{P} of the small precipitates on the overall composition and their elastic modulus E_{P} by

$$E = f_{\mathrm{P}} E_{\mathrm{P}} + (1 - f_{\mathrm{P}}) E_{\mathrm{L}} \,. \tag{4.9}$$

The density of these precipitates can be calculated with suitable simulation techniques. Again, the altered elastic modulus is incorporated into the model by changes in the element stiffness matrix of the affected phase.

Second, small precipitates are causing a so-called back stress. This back stress lowers the effective stress distribution, which is the driving force for dislocation creep, as outlined in section 3.1.6.3. It is incorporated into the model by lowering the effective stress, which is responsible for the evolution of the creep strain by

$$\sigma \rightarrow (\sigma - \sigma_b) \tag{4.10}$$

where σ_b is the back stress.

In contrast to the fine dispersed particles, large precipitates are introduced into the model as a distinct, separate phase. Their elastic modulus is generally higher than that of the surrounding matrix, which causes different stress-strain responses. Poisson's ratio is assumed to have the same value as the bulk material. The implementation of both parameters into the system of equations again takes place through equations (3.41 and (4.3).

4.2.3 Modelling Mass Fluxes

Atomic diffusion is modelled according to the Nabarro-Herring creep law. The resulting mass fluxes, which are dependent on the acting stresses, are incorporated into the model using a creep law, which links these stresses with the resulting creep strain. Assuming constant density, the mass flux leads to a shape change of the overall volume of the material. The resulting strain can be linked to this mass flux as follows.

The flux J of atoms per time and unit area is given by Fick's law with

$$J = -D\frac{\partial c}{\partial x} \tag{4.11}$$

where D is the diffusion coefficient and c is the concentration of the considered atoms. Integrating this flux J in time t and space $\mathrm{d}\Omega$ gives the total number of particles N_p, which flow out of the considered integration volume $\mathrm{d}\Omega$. Multiplying this number N_p with the mass per particle m_p gives the total change in mass $\mathrm{d}m$ by

$$m_p N_p = m_p \iint J \mathrm{d}\Omega \mathrm{d}t = \mathrm{d}m\,. \tag{4.12}$$

On the other hand, any change in mass in linked to a change in volume via the mass density ρ by

$$\mathrm{d}m = \rho \mathrm{d}V\,. \tag{4.13}$$

Keeping in mind the definition of strain $\boldsymbol{\varepsilon}$

$$\varepsilon_x = \frac{\partial x}{x},\quad \varepsilon_y = \frac{\partial y}{y},\quad \varepsilon_z = \frac{\partial z}{z}, \tag{4.14}$$

the volume change dV can be calculated in terms of change in strain and, therefore, can be linked to the effective creep strain with

$$\bar{\varepsilon} = \frac{\mathrm{d}V}{V} = \frac{\mathrm{d}m}{m} = \frac{1}{m} m_p \iint J \mathrm{d}\Omega \mathrm{d}t \,. \tag{4.15}$$

This effective creep strain, which is caused by mass transport by the flux J, is then directly incorporated into the code. For modelling the resulting effective creep strain, the expression

$$\bar{\varepsilon} = A \bar{\sigma}^n \bar{t}^m \tag{4.16}$$

is selected, where $\bar{\sigma}$ is the effective stress, $\bar{t}$ is the effective time and A, n and m are constants. This choice is motivated by generality, because with this expression it is possible to describe different creep regimes with different sets of material constants and to incorporate different mechanisms. All parameters, which influence these fluxes, such as the diffusion coefficient, temperature, dislocation densities and so forth, are included in the parameter A of equation (4.16).

As already mentioned, due to the generality of expression (4.16), it is possible to include empirical descriptions for strain hardening and time hardening as well. Strain hardening can be incorporated by giving A a dependency on the accumulated plastic strain. Time hardening is already incorporated and can be modified by choosing the constant m properly. For future work, this provides additional possibilities to expand and to upgrade the model.

4.2.4 Selection of Material Parameters

A characteristic set of parameters for the creep regime to be modelled has to be chosen. These parameters depend on the microstructure, the temperature and the stress range. For comparison, parameters corresponding to those of experimental boundary conditions have been chosen [113]. The implementation into the model is described in sections 4.2.2 and 4.2.3

With the implemented algorithm, it is possible to model time hardening as well; however, it is not considered in this work due to its minor relevance in the context of diffusional creep. Thus, the time-dependence of the creep rate is linear and the constant m is chosen to equal 1 for all calculations.

4.2.4.1 Modelling Nabarro-Herring Creep

In the diffusional creep regime, the stress dependence on the applied stress is linear. Therefore, the constant n in equation (4.16) has to be chosen with $n = 1$. The other quantities,

such as the mean lattice diffusion coefficient D_L, the general constant for diffusional creep A_{NH}, the atomic volume Ω and grain size d are included in the parameter A with

$$A = A' A_{\mathrm{NH}} \frac{D_L \Omega}{d^2 kT} \tag{4.17}$$

where A' is a constant, which equals 1 in all presented simulations.

The temperature T for all simulations is chosen with $T = 600°\mathrm{C}$. The grain size varies between 2 and 100 μm. The diffusion coefficient D_L is dependent on temperature through an exponential law [11]

$$D = D_0 \exp\left(\frac{-Q}{RT}\right) \tag{3.7}$$

where D_0 is the pre-exponential factor, Q is the activation energy and R is the ideal gas constant. Using the material parameters given in [113], the mean lattice diffusion coefficient is calculated with $D_L = 2.85 \cdot 10^{-19}\ \mathrm{m^2/s}$. The atomic volume Ω can be calculated by using the lattice parameter a with

$$\Omega = \frac{a^3}{n_{\mathrm{atom}}} \tag{4.18}$$

where n_{atom} is the number of atoms within the unit cell. Using lattice constants for ferritic steel [11], the atomic volume is given with $\Omega = 1.17 \cdot 10^{-29}\ \mathrm{m^3}$. The general constant for Nabarro-Herring creep A_{NH} lies within the range of 12 – 40 [28] and is chosen with $A_{\mathrm{NH}} = 13.3$ for polycrystals [5].

4.2.4.2 Modelling Dislocation Creep

Even though the main task of this thesis is to model diffusional creep, some very simple examples of dislocation creep are simulated as well to demonstrate the potential that the present model offers.

Dislocation creep is generally dependent on some n^{th} power of stress. In this work, a creep law for diffusion-controlled dislocation climb creep by Nabarro [1] is modelled with

$$\dot{\varepsilon} = A_{\mathrm{N}} \frac{D_L G \Omega}{b^2 kT} \left(\frac{\sigma}{G}\right)^3 \tag{4.19}$$

where D_L is the mean lattice diffusion coefficient, G the shear modulus, Ω the atomic volume, b the Burgers vector, k Boltzmann's constant and T the temperature. The stress exponent for the dislocation creep examples is chosen to be $n = 3$. All other quantities are integrated within the general parameter A with

$$A = A' A_{\mathrm{N}} \frac{D_L G \Omega}{b^2 k T} \tag{4.20}$$

where A' is a constant. Other variables, such as dislocation densities, dislocation mobilities, dislocation lengths and activation energies, are included in this model as intrinsic variables. D_L and Ω are calculated according to the previous section.

The magnitude of the Burgers vector depends on the atomic plane of dislocation movement and the lattice parameter a with

$$\|\mathbf{b}\| = \frac{a}{2}\sqrt{h^2 + k^2 + l^2} \tag{4.21}$$

where h, k and l are the components of the Burgers vector. Assuming an offset of one crystal layer, which is common for metallic materials, and a dislocation plane corresponding to the [1 1 1] direction, the magnitude of the Burgers vector equals $b = 2.46 \cdot 10^{-10}$ m.

Again, due to the generality of the chosen expression (4.16), this model can be replaced by other models in a simple way, if desired.

4.2.5 Temperature Dependence

Temperature dependence can easily be taken into account by letting the materials constants be a function of temperature. The diffusion coefficient has an Arrhenius type of dependence on temperature T given by

$$D_{\mathrm{L}} = D_0 \exp\left(-\frac{Q}{RT}\right) \tag{3.7}$$

where Q is an activation energy and R is the gas constant.

Due to the linear expansion of rigid bodies, the elastic modulus E decreases with decreasing temperature. Still, due to possible anomalies in Young's modulus [114,115], it is recommendable to take precise, experimental values for the desired temperature range from literature. An interpolation for intermediate temperatures can be done using quadratic functions [116]. In this work, Young's modulus is assumed to have a value of E = 143 000 MPa at the elevated temperatures used in the simulations.

Other material constants, such as Poisson's ratio and Burgers vector, slightly differ with temperature as well, again an interpolation can be done using polynomial functions [116]. All examples presented in this work are simulated at a fixed temperature. An adjustment for other temperatures can easily be done by adjusting these parameters where necessary.

4.3 Code Implementation

4.3.1 Own Code

Numerous commercial finite element software packages are available nowadays for structural analysis in solid-state problems. General-purpose FEM codes normally include some conventional creep models. The parameters of the chosen creep law are specified by the user, but further intervention into the model and the code is not easily possible. As an addition, in some FE software packages, it is possible to define user specified subroutines for creep calculations. Even with this device it is not possible to incorporate all ideas, especially some features of a spatially resolved microstructure with locally differing characteristics. In addition, any linking with other software should be possible without restrictions.
For these reasons, it is worthwhile to set up an own independent finite element model to calculate creep behaviour.

4.3.2 Technical Details

For the numerical implementation of the presented model, the general-purpose, commercial software MATLAB® is utilized. MATLAB is a software package, which provides an interactive environment and high-level programming language for numerical computations. Its main focus lies on numerical analysis, although add-on toolboxes allow access to computer algebra capabilities.

In the implemented code, all basic equations and expressions are programmed directly. Therefore, a transfer to any other programming language can easily be done. Only for solving the systems of equations, basic MATLAB routines for matrix calculation are used. Furthermore, all graphical output is handled with tools provided by MATLAB.
The finite element method is encoded applying a standard Lagrangian approach using Hooke's law. As element type, a quadrilateral element with four nodes is used.
For the necessary integrations, the concept of Gaussian quadrature is adopted. The analytic solution of the integral is approximated by summing up the values of the function to be integrated on the four specific points specified in Table 2.

A standard patch test [106] for elastic behaviour has been conducted successfully to show that the implementation works correctly. For this test, a grid containing 5 elements with altogether 8 nodes is set up as shown in Fig. 26. A plane stress analysis is performed. Node 1 is fully

restrained and node 4 is restrained only in the *x* direction. Then the forces *F* specified in Table 3 for nodes 2 and 3 are applied to the system.

Table 2: Coordinates of the four Gauß points used to calculate the weighted values of all integrated functions.

X	Y
$\sqrt{1/3}$	$\sqrt{1/3}$
$\sqrt{1/3}$	$-\sqrt{1/3}$
$-\sqrt{1/3}$	$-\sqrt{1/3}$
$-\sqrt{1/3}$	$\sqrt{1/3}$

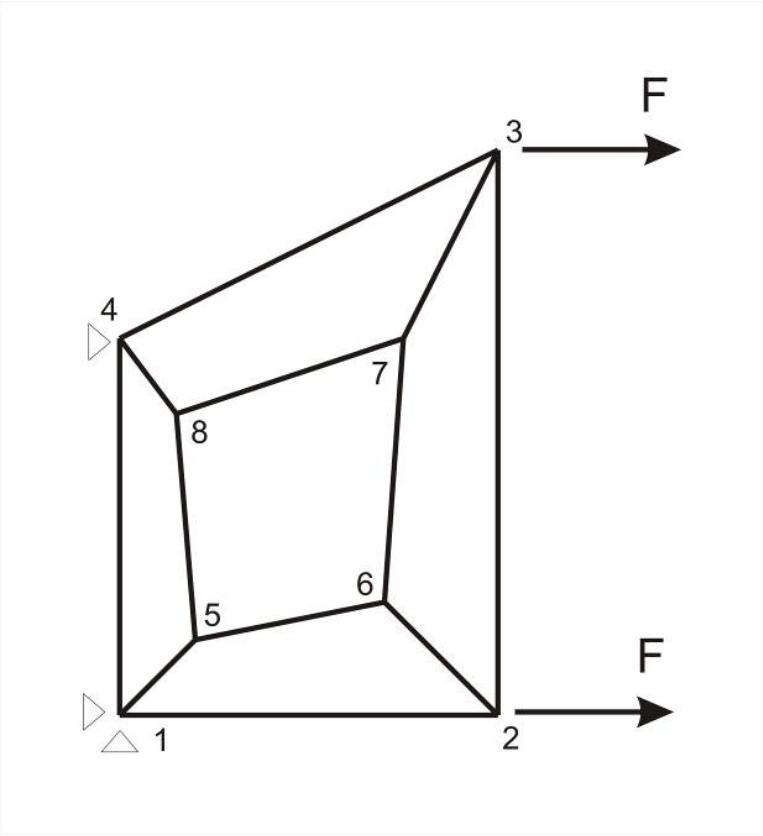

Fig. 26: Patch test with a five element grid, restrained nodes and applied forces.

Table 3: Node numbers *i*, coordinates x_i and y_i off all nodes, displacements u_i and v_i and forces F_{xi} and F_{yi} for the applied patch test.

	Coordinates		Displacements		Forces	
Node *i*	x_i	y_i	u_i	v_i	F_{xi}	F_{xi}
1	0.0	0.0	0.0	0.0	-2	0
2	2.0	0.0	0.0040	0.0	3	0
3	2.0	3.0	0.0040	-0.00186	2	0
4	0.0	2.0	0.0	-0.00120	-3	0
5	0.4	0.4	0.0008	-0.00024	0	0
6	1.4	0.6	0.0028	-0.00036	0	0
7	1.5	2.0	0.0030	-0.00120	0	0
8	0.3	1.6	0.0006	-0.00096	0	0

The simulation produces exact solutions for all nodal quantities listed in Table 3. Thus, the basic implementation can be considered as to work correctly.

4.3.2.1 Layout of the Code

As is illustrated in Fig. 27, the code is divided into three main modules: the input and set up of all necessary data, evaluation of the system equations and their solution and, finally, the output of the results. Each of these modules is divided into sub-modules, the details of which are outlined in the next chapters.

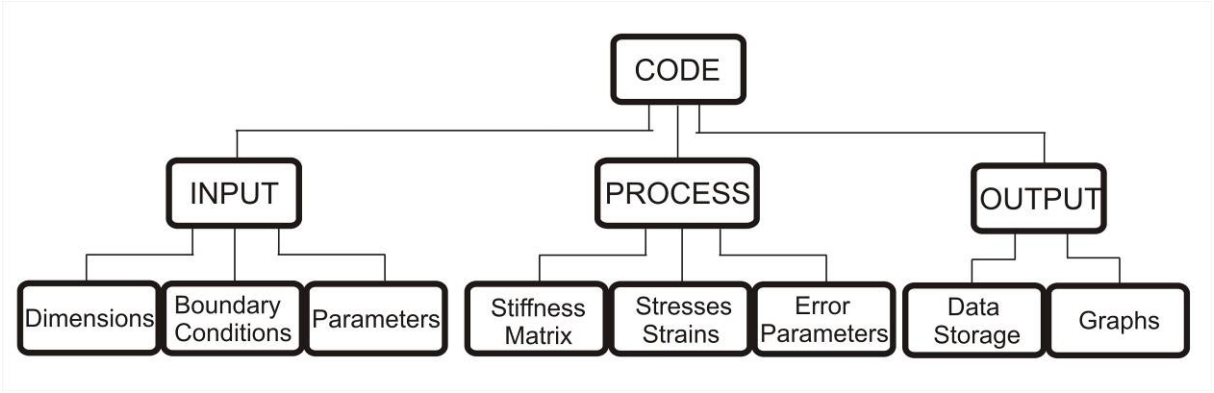

Fig. 27: Modules and sub-modules of the implemented code.

Input

At the beginning, all necessary input data have to be handled. As a first step, the finite element grid itself is set up. All nodes have to be specified by their coordinates in *x* and *y* direction, each node has to be identified with a positive integer number. Then, all nodal

connections have to be specified. That is, for each element, the four attached nodes have to be named in a list. Furthermore, all elements of the grid have to be indexed as well.
For simple, rectangular meshes, these specifications are done by a simple sub-routine. Only the length of an element and the number of elements per boundary have to be specified. The mesh and the table for the elements and nodes are calculated automatically. Shapes other than rectangular can be defined as well, but node numbering and all mesh-defining tables must then be inserted manually.
All boundary conditions have to be specified at the corresponding node numbers. Two different types can be distinguished. The Dirichlet boundary condition specifies a value that the solution of the problem must adopt at the boundary. In this model, as usual in structural mechanics, this corresponds to specification of a displacement for a node. In the input file, this is done by a list of node numbers and the corresponding displacements in both *x* and *y*-direction.
Neumann boundary conditions specify the value that the derivative of the solution has to adopt on the boundary. In other words, the force acting on the chosen node has to be given. In this model, again, this results in the specification of the node numbers and the corresponding forces in *x* and *y*-direction.
Parameters concerning physical properties of the structure, such as Young's modulus, diffusion coefficients, threshold hold stresses etc. have to be specified for each element. For each of these parameters, again, this is done by tabulating the element numbers and the corresponding values. In principle, they can be specified per Gauß point as well, but in the actual examples calculated with the model, this is not done.
For handling of the iteration process, some additional parameters have to be established. These include the maximum number of iterations, the maximum number of increments, the time interval for each increment and error parameters.

Setup of the Stiffness Matrix

The first step when setting up the mathematical model is the specification of the system of equations, which describe the system. To do so, the stiffness matrix for each element has to be established by a summation with

$$\mathbf{K}^e = \sum_i \mathbf{B}^{\mathrm{T}} \mathbf{D} \mathbf{B} \det \mathbf{B} \tag{4.22}$$

over all four Gauß points *i* of the element. The strain displacement Matrix **B** in this implementation is not constant and has to be calculated for each of these Gauß points. The determinant of **B** reflects the size of the single finite element and equals one if the actual cell

has the same size as the finite element unit cell. The matrix **D** is dependent on some physical parameters and, therefore, has to be set up for each Gauß point as well.

The stiffness matrix of the overall element assemblage is calculated using the direct stiffness method. In this procedure, each element matrix $\mathbf{K}^e$ is inserted into the overall matrix by adding the entries at the corresponding node numbers, as is indicated in Fig. 28. Other methods have been proven to be too time-expensive for an implementation with MATLAB.

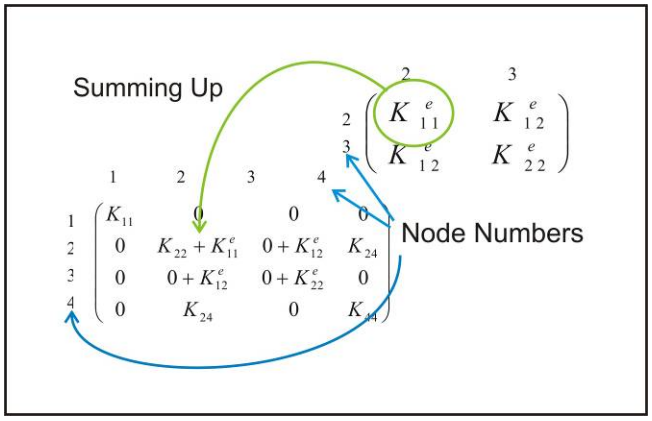

Fig. 28: Assemblage of the overall stiffness matrix using the single element stiffness matrices.

Once the stiffness matrix is set up, the boundary conditions for the individual nodes are implemented into the matrix **K** and the external force vector **F**, both forming the system of equations

$$\mathbf{Ku} = \mathbf{F} \tag{4.23}$$

where **u** contains the unknown displacements.

As already discussed in chapter 3.3.2.5, Dirichlet boundary conditions control the value of the solution for the selected node, in other words, the displacement is prescribed. In this work, a simplified method (containing two solution steps) is used. For the selected node *i*, the entry K_{ii} in the stiffness matrix is set to one. Then, all other entries in the corresponding row and column are set to zero. The matching entry in the load vector **F** adopts the selected value for the displacement. One has to keep in mind that, in this case, for the resulting displacements of all other nodes, a second purely elastic step of the calculation must be carried out. Fixing a node is handled as a special type of a Dirichlet boundary condition with zero displacement, albeit, in this case, a second elastic iteration of the calculation is not necessary.

The implementation of Neumann boundary conditions is much simpler. This kind of boundary conditions reflects the applied external force. For the selected node *i,* the selected value is prescribed in the entry F_i of the force vector.

For solution of the system of equations, the modified Newton-Rhapson method is used. That is, the stiffness matrix is only setup once and then remains constant throughout all simulation processes. This completes the setup of the problem before the iteration scheme can start.

Incremental Process to Calculate Stresses and Strains

The calculation of stresses and strains for non-elastic problems, as in the visco-plastic regime, has to be done stepwise, and the overall time has to be divided into time steps, i.e. into increments. Within each of these increments, several iterations are computed to reach the equilibrium solution for the actual increment, i.e. time step. Fig. 29 gives an overview. Furthermore, in this kind of problem, the application of all external loads is done stepwise to ensure stability of the following calculations, i.e. the load is not applied all at once, but over a relatively short, but defined time interval. Therefore, the external force vector $\mathbf{F}_{ext}$, which includes all prescribed displacements and applied forces, has to be updated at the beginning of each increment. The time step Δt is specified and the overall time t is updated as well.
At this point, the iteration process for the calculation of the equilibrium solution for the actual increment starts. In a first step, the residual force vector $\boldsymbol{\Psi}$, which denotes the difference between the internal reacting forces $\mathbf{F}_{int}$ and the external load $\mathbf{F}_{ext}$, is set up.

The internal forces can be regarded as the reaction of the system to balance the applied external load on the nodes. Any deviation of this balance is calculated by the vector $\boldsymbol{\Psi}$ with

$$\boldsymbol{\Psi} = \mathbf{F}_{int} - \mathbf{F}_{ext} . \tag{4.24}$$

The internal forces are calculated from the existing displacements and equal zero for the very first step of the computation.

Then, all additional boundary conditions are implemented into the residual force vector. In the present model, these include all chosen fixations with prescribed zero displacement. The implementation is simply done by setting the entries in the residual force vector to zero for the selected nodes.

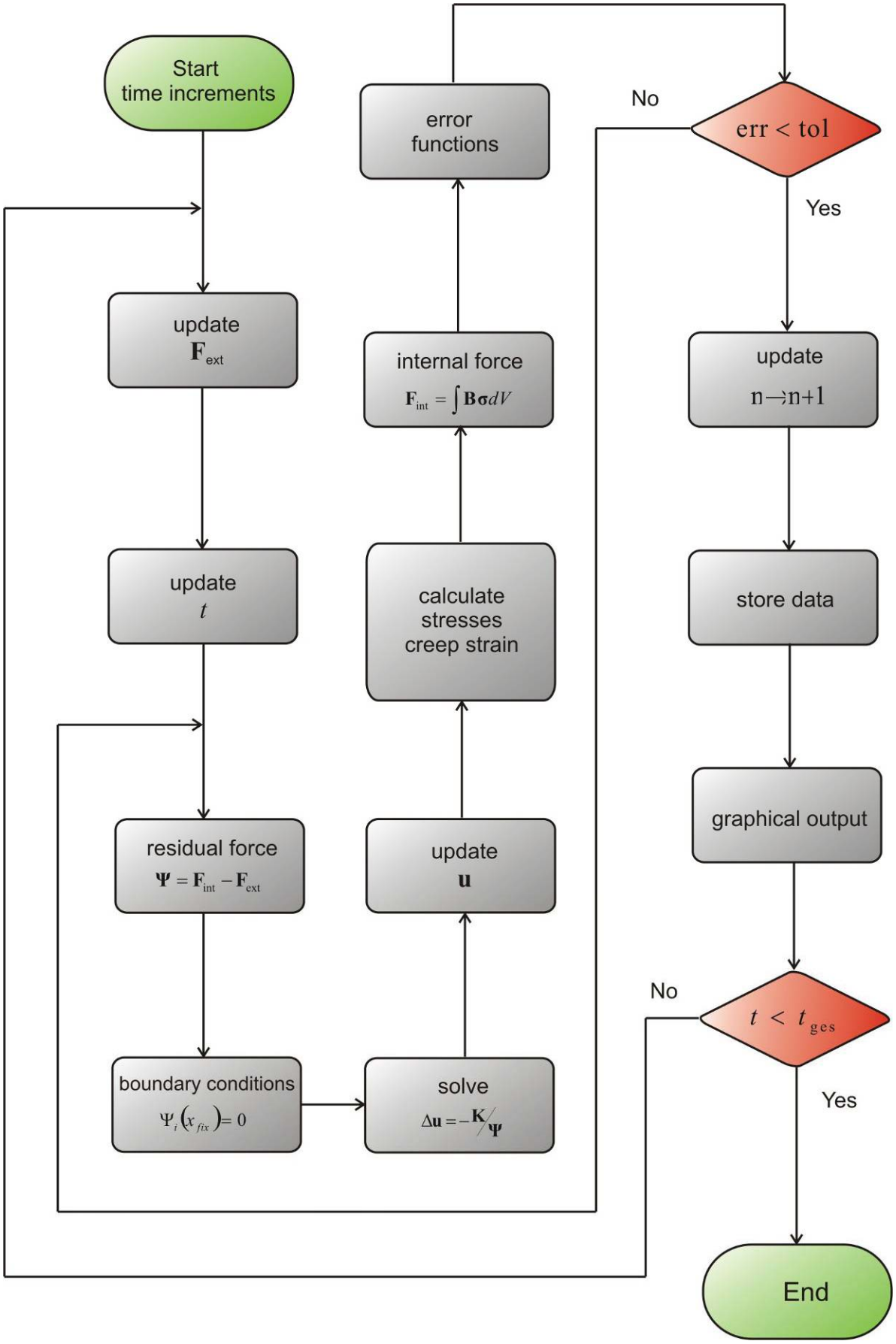

Fig. 29: The iteration scheme of the implemented routine to calculate the stresses and creep strains.

The displacements **u** are calculated in increments $\Delta\mathbf{u}$ by

$$\mathbf{K}\Delta\mathbf{u} = -\mathbf{\Psi}\,. \tag{4.25}$$

These displacements can be regarded as an adjustment of the structure to the imbalance described by the residual force.

To solve this system of equations, an internal routine of the MATLAB software is used based on matrix triangulation. The output is stored into a vector. With this result, the overall displacements for the actual step u_{n+1} are updated.

The next step is the central part of the model and consists of calculating the stresses and creep strains. A more detailed outline for this segment is given in section 4.3.2.2 below.

Once the stresses and strains are calculated, the internal response to the external loads can be updated. To do so, in a first step, these forces are computed for each node of each single element with

$$\mathbf{F}_{\text{int}}^{\text{el}} = \sum_{i} \mathbf{B}^{\text{T}} \boldsymbol{\sigma}_{n+1} \det \mathbf{B} \tag{4.26}$$

using the actual stresses $\boldsymbol{\sigma}_{n+1}$ and the strain-displacement matrix **B**. In Fig. 30, this procedure is indicated for four adjacent elements, for each node, the reacting force in terms of *x* and *y* component for all four elements is calculated. In a second step, the total force acting on a node can be calculated by summing up the nodal forces of the four neighbouring elements. In Fig. 30, this is shown for the marked node in the middle.

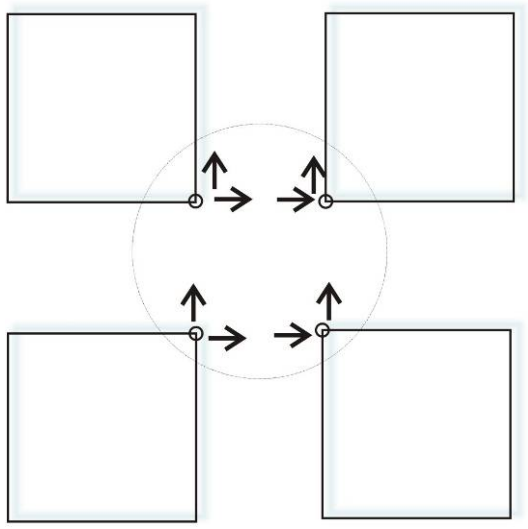

Fig. 30: Summing up the forces for each node, using the adjacent four elements.

The calculated overall forces are stored into the vector forces $\mathbf{F}_{\text{int}}$ and are used in the next iteration step to calculate the next residual force vector as stated in equation (4.24).

The final step of the actual iteration is to evaluate whether the system is near equilibrium. Various methods for doing this exist. In this present model, the method chosen is a check for the unbalanced energy E_{unb}. This energy is calculated by

$$E_{\text{unb}} = -\boldsymbol{\Psi}\Delta\mathbf{u} \tag{4.27}$$

and gives an estimate of the error of the calculation. If this error is below a given threshold, the iteration loop can stop. Otherwise, the calculation of displacements and the resulting strains and stresses is repeated.

After a successful end of the iteration loops, the stresses and strains are stored as the new equilibrium solution *n* and the output of all desired data for the actual increment done. When finished, the next time step can be calculated by starting the next increment. When the overall time limit is reached, which means that the desired number of increments has been calculated, the procedure stops.

Output

The main results of the simulations are the computed stresses and strains. Additional information, such as time steps and error parameters, provide valuable information as well. The output of these results is handled in two different ways. On the one hand, the results are stored into fields and can be used for different kinds of post-processing, data analysis and evaluation. On the other hand, the results can be represented graphically using routines provided by MATLAB. This provides some limitations, but the programming of own graphic tools would have been too time-expensive in the present project.

The routines used in this model to plot distribution for stresses, strains and other variables can only handle one value per element. This results in a relatively coarse representation of these distributions, albeit the exact solution of the system of equations is calculated at more than one point per element. Furthermore, an interpolation can be done for every point of the element with any length scaling desired. An example is shown in Fig. 31. In the left part of the figure, the overall solution is displayed. In the right part the interpolation results for the indicated element are shown.

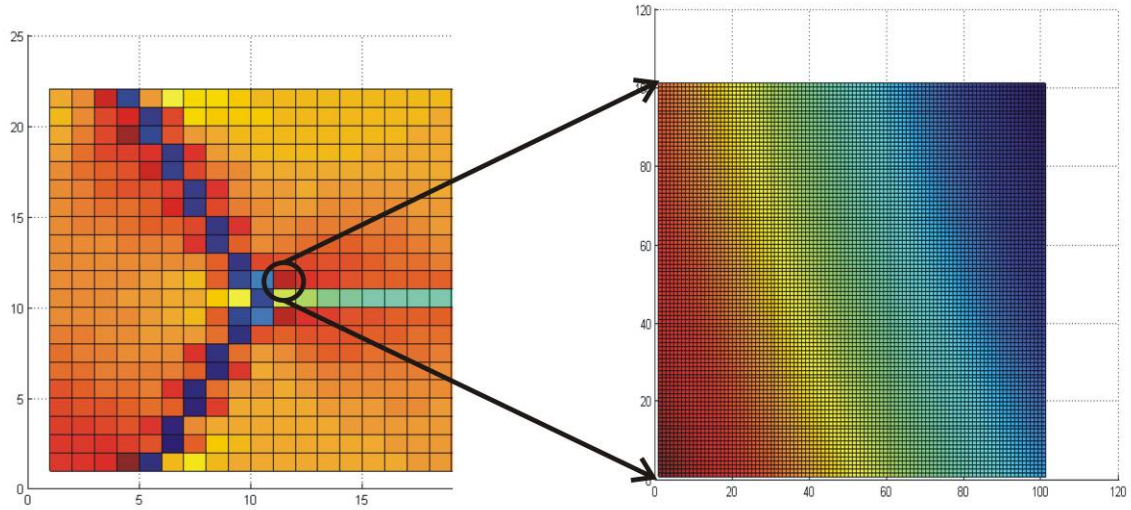

Fig. 31: Coarse graphical representation of the results versus the more detailed interpolation that can be calculated.

A second limitation, when displaying the results graphically, consists of the fact that the actual deformation and offsets of the nodes cannot be displayed simultaneously with the resulting stresses. Either stresses or strains in terms of coloured meshes can be shown, or the strains itself in terms of a deformed mesh can be displayed.

All these mentioned limitations only affect the graphical representation of the output, but do not bring any limitation on the quality of the results that the model produces. The underlying data itself is not affected by these limitations.

4.3.2.2 Details on the Calculation of Creep Strain and Stresses

The calculation of the stresses and the resulting creep strain is the central part in modelling of creep and other visco-plastic phenomena. In the presented model, a formulation following Whirley and Henshall [117] was implemented. Its basic steps are outlined in the following paragraphs.

The scheme is a fully implicit method, which makes the algorithm unconditionally stable. The creep strains and stresses for the step n+1 have to be calculated for each element and for each Gauß point separately. Within this double loop, several steps to get the desired result are necessary. Fig. 32 gives an overview. All necessary constants, the time step Δt and the overall displacements of the element have to be given to start. These overall displacements are evaluated by the solution of the system of equations (4.25). Furthermore, the values for the creep strain and the stresses of the equilibrium solution n of the last time step are assumed to be given. For the very first increment within this procedure, they equal zero.

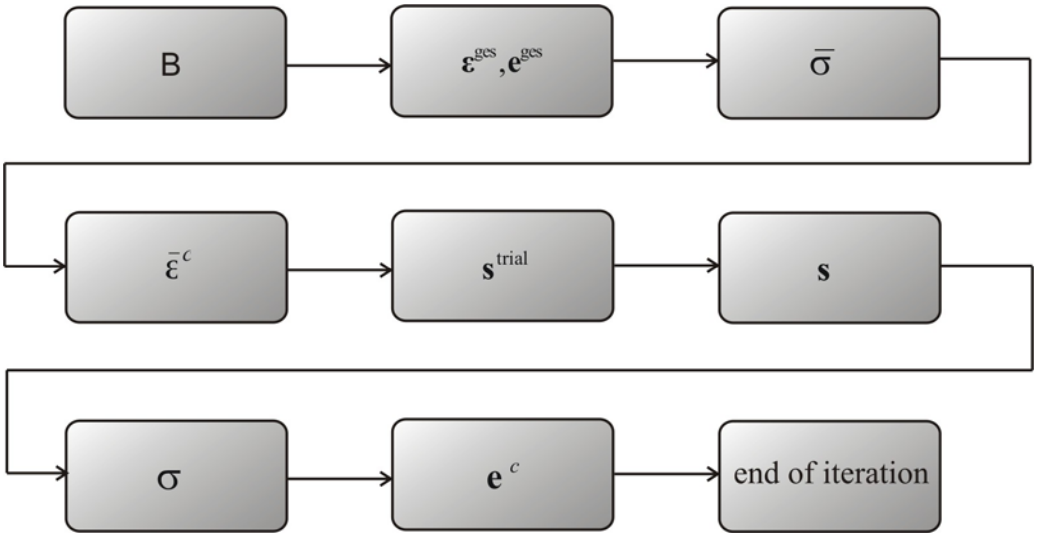

Fig. 32: Necessary steps to calculate the updated stresses and creep strains within each iteration.

The first step, as can be seen in Fig. 32, is to calculate the strain-displacement matrix **B**, which contains geometrical information on the element and the Gauß point, for which the calculation is done. Using this matrix and the given displacements, the overall strain **ε** and the deviatoric part **e** of the strain are calculated. The deviatoric strain and the resulting stresses are linked to each other. In this model, the relationship is given by

$$\left|\mathbf{e}_{n+1} - \mathbf{e}_n^{c}\right| = \sqrt{\frac{2}{3}}\frac{1}{2G}\bar{\sigma}_{n+1} + \frac{3}{2}\sqrt{\frac{2}{3}}A\bar{\sigma}_{n+1}^{n}\left\{\left[\left(\frac{\bar{\varepsilon}_n^{c}}{A\bar{\sigma}_{n+1}^{n}}\right)^{1/m} + \Delta t\right]^{m} - \left(\frac{\bar{\varepsilon}_n^{c}}{A\bar{\sigma}_{n+1}^{n}}\right)\right\} \qquad (4.28)$$

where A is a constant, $\bar{\sigma}_{n+1}$ is the effective stress of the actual increment n+1, $\bar{\varepsilon}_n^{c}$ the effective creep strain from the last equilibrium solution n and $\mathbf{e}_{n+1}$ the overall strain of the actual iteration. The effective stress is calculated by finding the root of this non-linear equation. The procedure to do so is outlined separately in a paragraph at the end of this section.
With each subsequent iteration, the stress found from equation (4.28) will converge to the equilibrium final stress. An example is demonstrated in Fig. 33, where the development of the effective stress in one Gauß point within one increment, i.e.time step, is shown. On the *x*-axis, the number of iterations is given, on the *y*-axis, the actual stress found from equation (4.28) is plotted. Within the first iterations, the estimated stresses are too small, but then the stress converges and stays constant.

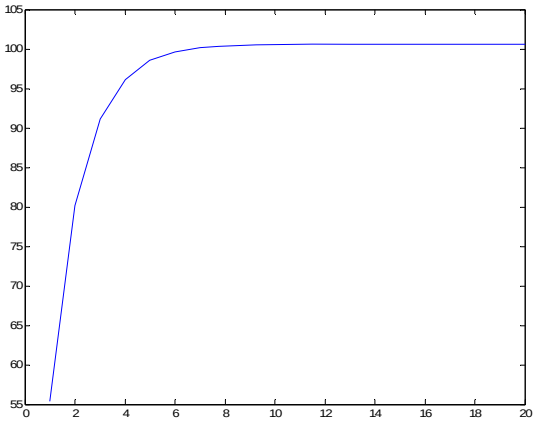

Fig. 33: The convergence of the calculated effective stress on one Gauß point within one increment.

This is an indicator for the importance of ensuring that the obtained solution is as close as possible to the stable solution. Only when enough iterations are done, the stresses and the creep strains will equal equilibrium values, the model will produce correct results and the next time step can be calculated.

Once the effective stresses for the actual iteration are found, the resulting creep strain can be calculated. The creep behaviour is described by equation (4.16). Within the implementation of the model as an incremental form, the expression

$$\Delta\bar{\varepsilon}^{\mathrm{c}} = A\bar{\sigma}_{n+1}^{n}\bar{t}^{m} \tag{4.29}$$

is used to calculate the increment in effective creep strain. The effective time is found with

$$\Delta\bar{t}^{m} = \left(\bar{t}_{n} + \Delta t\right)^{m} - \Delta\bar{t}_{n}^{m}\,. \tag{4.30}$$

To find the normal stresses, a predictor-corrector procedure is implemented. As the predictor step, the stress, which would occur if the calculation would be purely elastic, is calculated. This stress is the so-called trial stress $\mathbf{s}^{\mathrm{Tr}}$, given with

$$\mathbf{s}^{\mathrm{Tr}} = \mathbf{s}_{n} + 2G\Delta\mathbf{e}\,. \tag{4.31}$$

In a second step, the deviatoric stresses $\mathbf{s}_{n+1}$ are then updated with

$$\mathbf{s}_{n+1} = \mathbf{s}^{\mathrm{Tr}}\frac{1}{1+3G\dfrac{\Delta\bar{\varepsilon}^{\mathrm{c}}}{\bar{\sigma}_{n+1}}} \tag{4.32}$$

In contrast to the procedure by Whirley et al., this formula includes a $\Delta\varepsilon$ instead of ε. This is motivated by using the relationship

$$\mathrm{d}\mathbf{e}^{\mathrm{c}} = \frac{3}{2}\frac{\mathbf{s}}{\bar{\sigma}}\mathrm{d}\bar{\varepsilon}^{\mathrm{c}} \tag{4.33}$$

to connect the increments in creep strain $\mathrm{d}\mathbf{e}^{\mathrm{c}}$ to the components of the deviatoric stress tensor $\mathbf{s}$.

In a third step, the total normal stresses have to be sought. To do so, a volumetric pressure term is added to the deviatoric stresses, which delivers

$$\boldsymbol{\sigma}_{n+1} = \mathbf{s}_{n+1} + K\mathrm{Tr}(\boldsymbol{\varepsilon}) \tag{4.34}$$

Finally, the resulting deviatoric creep strains $\mathbf{e}^{c}$ are calculated by using equation (4.33). The normal creep strain ε_n^{c} equals the deviatoric creep strain, because viscoplastic phenomena are not influenced by hydrostatic stresses.

This completes the algorithm used for calculating the stresses and creep strains in the model. All necessary quantities are updated and the next iteration step of the model can start.

Finding the effective stresses

An important point in the simulations is to find the effective stresses from equation (4.28). To do so, a Newton iteration scheme as described in chapter 3.3 is implemented into the code. To get good results from this procedure, the starting value for σ at the beginning of the stepwise process has to be chosen carefully. For the implemented algorithm, two different values are adopted.

If the creep strain has dominated the total strain increment in the previous time step, the effective stress $\overline{\sigma}_{n+1}$ at the end of the current time step will be close to the stress $\overline{\sigma}_n$ from the last step. The initial guess for $\overline{\sigma}_{n+1}$, therefore, is simply the updated $\overline{\sigma}_n$ from the previous step with

$$\overline{\sigma}_{n+1}^{(\mathrm{start})} = \overline{\sigma}_n \,. \tag{4.35}$$

If the elastic strain has dominated the total strain increment, the updated stress σ (at the end of the current time step) will be closer to the purely elastic solution of the problem. This solution is called the elastic trial state $\mathbf{s}^{\mathrm{tr}}$ and it is calculated using equation (4.31), as stated in the next section of this chapter. In this case, as a starting value, the effective elastic trial stress with

$$\overline{\sigma}_{n+1}^{(\mathrm{start})} = \sqrt{\frac{3}{2} s_{ij}^{\mathrm{tr}} s_{ij}^{\mathrm{tr}}} \tag{4.36}$$

is chosen.

The convergence criterion for termination of this iterative calculation of the updated stress $\overline{\sigma}_{n+1}$ is written as

$$\left| \frac{\overline{\sigma}_{n+1}^{(k+1)} - \overline{\sigma}_{n+1}^{(k)}}{\overline{\sigma}_{n+1}^{(k+1)}} \right| \leq \mathrm{tol} \tag{4.37}$$

where k is the local iteration number within the Newtonian iteration scheme, and tol is an error tolerance to be specified. A value of 10^{-5} usually ensures accurate results.

4.3.3 Suggested Future Work

4.3.3.1 Modifications of the Model

To adapt and further improve the model on a physical basis, different paths can be followed. The physical basis of the implemented model can be adapted by e.g.

- the implementation of other creep laws,
- the usage of shear stresses instead of normal ones,
- incorporation of anisotropy,
- and the integration of strain hardening.

The feature of time hardening is already implemented.
Another subject is the usage of other types of finite elements. For an improvement in terms of accuracy, elements with more than four nodes can be introduced, albeit one has to keep in mind that, especially for such implementations with MATLAB, the computing time will increase significantly. To handle other phenomena, such as boundary sliding, other elements with different characteristics and properties, such as contact features, can be implemented. Improvements in the area of mesh refining are also possible. In the actual implementation, only regular meshes with equal sized elements can be generated automatically. All other meshes have to be calculated and numbered by the user himself. Some automatic refinement with differing element sizes would be helpful if the user wants to take a closer look on selected areas of the specimen.

4.3.3.2 Changes Concerning the Computational Performance

To improve computational efficiency, the handling and the representation of the results, also some upgrading can be done.
In the actual code, boundary conditions have to be specified always for each point manually. For a simpler handling, it would be helpful, if the forces and fixations could be indicated per element or per boundary. The further segmentation to calculate the nodal forces must then be done automatically.
When a certain force is assumed to act on an element on the boundary, as indicated in Fig. 34 (a), the nodal components $\mathbf{F}_i$ for all points i of the specified element are calculated by

$$\mathbf{F}_i = \int_V \mathbf{B}^{\mathrm{T}} \boldsymbol{\sigma} \mathrm{d}V \ . \tag{4.38}$$

Once these forces (see Fig. 34 (b)) are calculated for all concerned elements, they all have to be assembled together to give the overall force vector $\mathbf{F}$ on the boundary. This is done by

summing up the components of each node, a procedure similar to the assemblage of the stiffness matrix **K**.

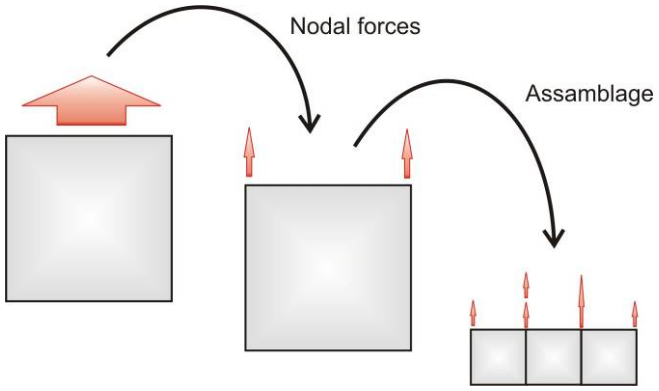

Fig. 34: Calculation and assemblage of the nodal force vector.

When visualizing this assemblage, as in Fig. 34, it becomes clear that, although the stress distribution is homogeneous, the distribution of the nodal forces is not. The forces on the nodes, which are directly situated at the edges of the concerned boundary, are smaller. This is an important point one has to keep in mind when calculating the applied nodal forces manually. To avoid errors, an introduction of an automatic routine could be helpful.

To setup the system of equations, which is necessary for determining the nodal displacements, in the implemented code the modified Newton-Rhapson method is utilised. In this method the stiffness matrix is determined once at the very beginning of the simulation, and then remains unchanged for all iteration and incremental processes.
To reduce computational time, the Newton-Rhapson method can be introduced instead. In this method, the constant stiffness matrix is replaced by a stiffness matrix, which is recalculated for each iteration loop. The advantage is that within each time increment, the displacements converge much faster to their equilibrium solution. In other words, less iterations are needed to reach equilibrium and the calculation time can be reduced considerably.
The stiffness matrix **K** within this procedure is calculated with

$$\mathbf{K} = \int_V \mathbf{B}^{\mathrm{T}} \frac{\mathrm{d}\boldsymbol{\sigma}}{\mathrm{d}\boldsymbol{\varepsilon}} \mathbf{B} \mathrm{d}V \tag{4.39}$$

where $\boldsymbol{\sigma}$ are the actual stresses and $\boldsymbol{\varepsilon}$ are the actual strains. The detailed deduction of this modified matrix can be complex and is dependent on the algorithm. However, it can increase the speed of the simulations significantly.
To increase the speed of the calculations in general, and for an expansion to bigger meshes, a porting to a low-level programming language such as C++ would be valuable. At the moment, the size of the grid is limited to 50x50 elements and simulations are relatively slow.

All these possible changes do not influence the results of the simulations, but only represent improvements in handling and calculation time. The mathematical accuracy of the results is already good and will not be improved by the suggested changes.

4.4 Conclusion

In this chapter, a spatially resolved model to simulate creep behaviour within a polycrystalline microstructure is presented. Diffusional creep processes are introduced and implemented into the model. The microstructure can represent different components, such as grains, grain boundaries and precipitates.

The numerical algorithm used in this model, is a robust and efficient method to calculate stress and strain response to given boundary conditions. To compute all quantities, an iterative process is used. The general form of the constitutive equation used in the present analysis makes the model flexible and adaptable. Details on the implementation of the algorithm into the code were given.

The model is capable of simulating the creep behaviour of a microstructure caused by diffusional processes. In this work, the creep behaviour following the ideas of Nabarro and Herring was set up. The inhomogeneous distribution of stresses and creep strains caused by the underlying microstructure is calculated. Numerical examples are shown in the next chapter.

5 Results

With the model implementation presented in the preceding section, various simulations are conducted to simulate the stress-strain response of microstructural elements and configurations. In the following section, the results of these calculations are presented in mainly three parts.

As a first step, some basic examples are calculated to test the model. In the second part, the purely elastic response of several microstructure configurations is shown. In the third part, the inelastic reactions due to the elastic, internal stresses, which act as a driving force, in terms of creep deformation and stresses are presented.

5.1 Overview on Modelling Parameters

As already outlined in the previous chapter, the physical parameters used in the calculations are taken from experimental values reported in literature. Numerical parameters are chosen such as to reach the requested accuracy. The applied boundary conditions are typical for diffusional creep experiments conducted on the 9-12% chromium steel P91, as published in literature [113].

In summary, the main parameters are listed in Table 4. Some parameters, such as the grain size d, the spatial resolution and the calculation time t, are different for each example and, therefore, are listed separately in the specific sections.

Table 4: Physical and numerical parameters used for the calculations. A_{NH} denotes the Nabarro-Herring creep parameter, D_L is the diffusion coefficient, Ω the atomic volume, T the temperature, E Young's modulus for the bulk material (b), the grain boundaries (gb) and hard particles (p), ν is Poisson's ratio, σ_{ap} is the applied von Mises stress, and N_{iter} the number of iterations used per increment.

A_{NH} [-]	D_L [m^2s^{-1}]	Ω [m^3]	k [JK^{-1}]	T [°C]	ν [-]
13.3	$2.85\ 10^{-19}$	$1.17\ 10^{-29}$	$1.38\ 10^{-23}$	600	0.3

E_b [Nm^{-2}]	E_{gb} [Nm^{-2}]	E_p [Nm^{-2}]	σ_{vm} [N]	N_{iter} [-]	
$143\ 10^9$	$71.5\ 10^9$	$286\ 10^9$	50	20	

5.2 Simple Examples for a Homogeneous Material

To evaluate the model and to show that the code has been implemented correctly, a first, basic example with only one single finite element is calculated. Diffusional Nabarro Herring creep, which is linearly dependent on the applied stress, is modelled. The material is considered to be homogeneous with only one single, cubic grain with a diameter of d = 2000 nm. An effective stress of 50 MPa is applied along the y-axis, the tensile direction is shown in Fig. 36, as well as the fixations. The overall simulation time is t = 100 h. All other parameters are listed in Table 4 in section 5.1.

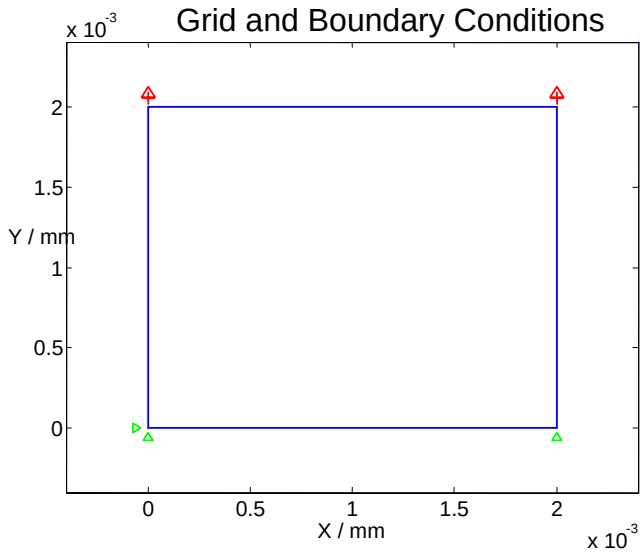

Fig. 36: Boundary conditions for a single cubic grain. The fixations are marked with green triangles, whereas the applied nodal forces are indicated by red arrows.

The numerical stability of the algorithm has shown to be good. The creep strain versus the time and the overall effective strain versus the time are shown in Fig. 37, the strains are linearly dependent on the stress. The difference between both denotes the purely elastic strain, which acts instantaneously upon the application of stress. This elastic strain is time independent and remains constant throughout the entire calculation, as expected. The slope of the effective creep strain curve corresponds to a stress exponent of n = 1, as typically is observed in diffusional creep.

The stress distribution inside the element is calculated at the Gauß points and is constant throughout the specimen. The results are in perfect agreement with the expectations and prove that the basic strain-stress behaviour is implemented correctly into the model.

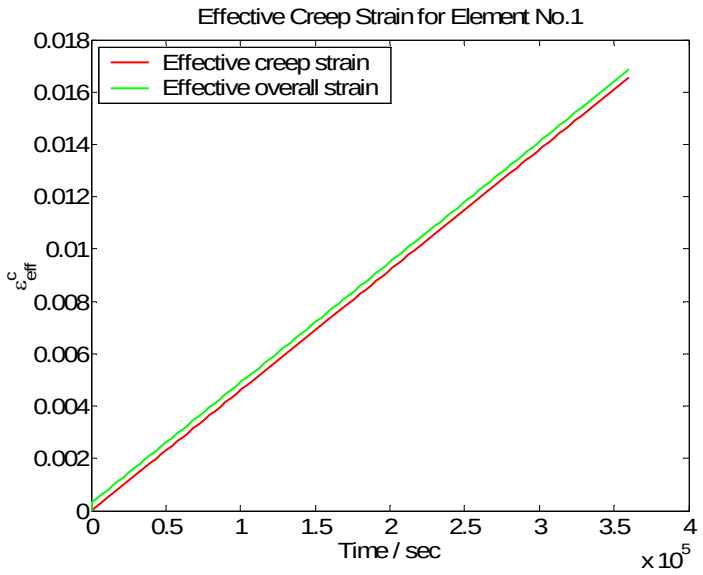

Fig. 37: Effective overall strain (green) and creep strain (red) for a single cubic grain subjected to diffusional creep for a period of 100 h.

As a next step, the mesh is refined. Instead of only one single finite element, the cubic crystal is represented by a 21x21 grid of finite elements with the same characteristics as in the previous example. The lateral length of each element is 95.24 nm, resulting in a grain diameter of d = 2000 nm, as in the previous example.

As expected, the results, which are shown in Fig. 38, are the same, the stress distribution is homogeneous. Therefore, for homogeneous, isotropic specimens, the mesh refinement has no relevant consequences.

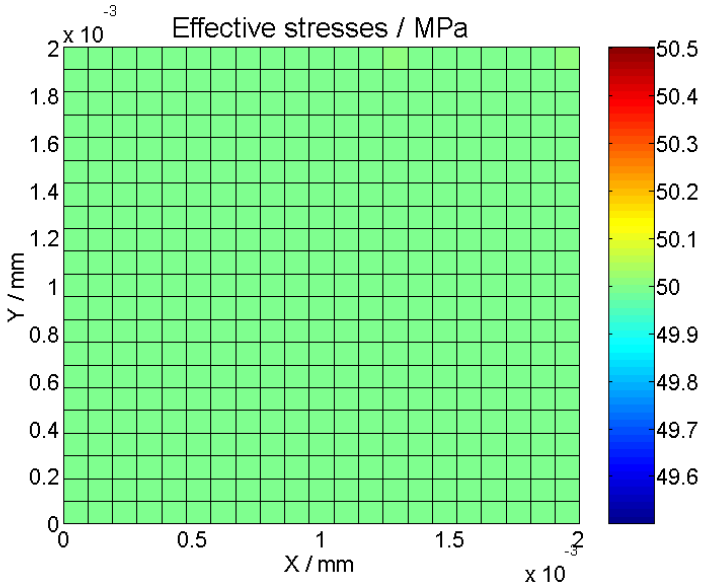

Fig. 38: Effective stress distribution for a single cubic grain calculated with a refined mesh.

The implemented algorithm is not restricted to only linear stress and linear time dependent creep laws. It is possible to model power law creep as well, the stress exponent can be chosen freely, albeit it has to be kept in mind that, especially for higher stress exponents, the convergence in the updated stress calculation is less stable. Therefore, the parameters have to be chosen carefully. The higher the stresses and the faster the creep rate, the more sensitive is the calculation of the effective stress in general.

An example is shown in Fig. 39. The stress exponent $n = 5$ is chosen to mimic power law creep. For all other parameters, the same values as listed in Table 4 in section 5.1 are chosen. For reasons of stability, the stress application has to be done stepwise within the first 100 increments. The slope of the creep curve in Fig. 39 shows the desired dependency on $n = 5$.

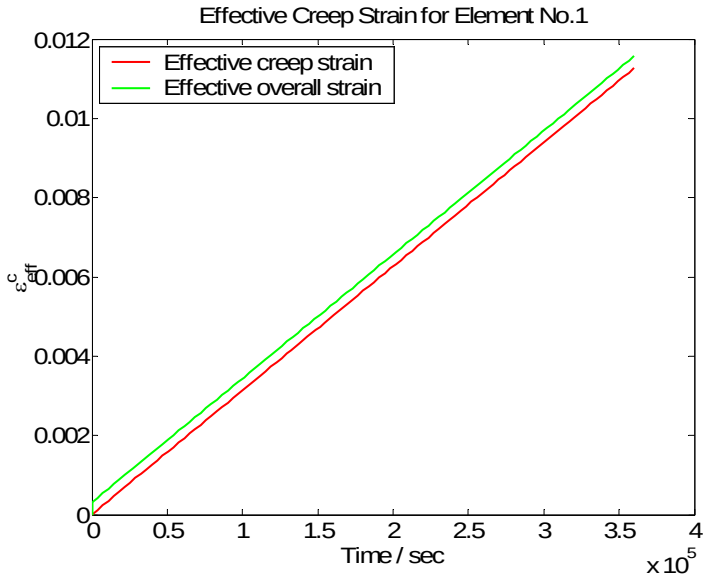

Fig. 39: Effective overall strain (green) and creep strain (red) for a single cubic grain subjected to power law creep with a stress exponent of $n = 5$ for a period of 100 h.

5.3 Results of Elastic Calculations

In general, a microstructure cannot be considered as a homogeneous configuration and the stress-strain response will show a distinct pattern depending on this microstructure. In this section, the elastic stress response of several microstructural configurations is presented.

5.3.1 Implementing Grain Boundaries

As a first item of the multiphase model, grain boundaries are implemented. To show the effect that an amorphous boundary produces within a crystalline phase, a purely elastic calculation is executed. Different stresses can be calculated, some samples are presented in the following figures.

For the calculation, a grid of 21x21 elements is used with an element length of 2000 nm. The boundary conditions are specified in Fig. 40 and consist of a fixation on the bottom x-line of the grid and an applied force on the top x-line with only a component in y-direction. The displayed internal stress for each element is the mean value of the stresses calculated at the four Gauß points.

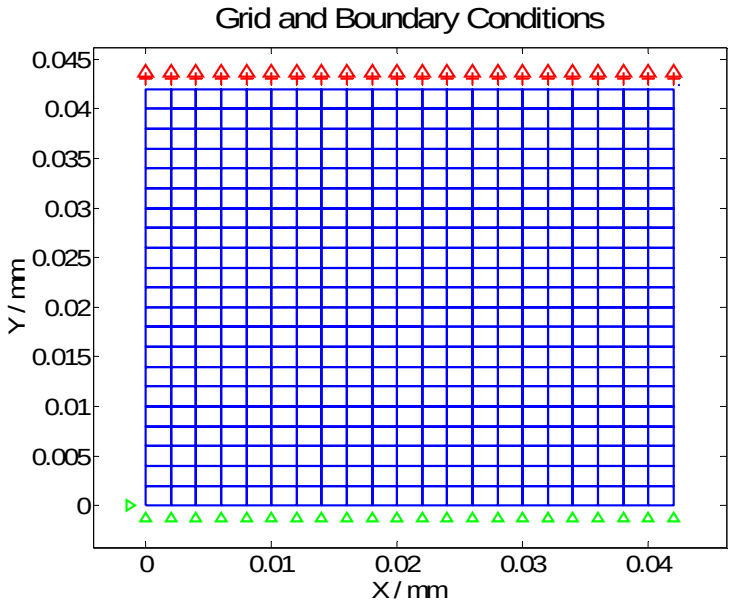

Fig. 40: Boundary conditions for the examples in section 5.2. The fixations are marked with green triangles, whereas the applied nodal forces are indicated by red arrows.

In the next examples, different configurations of grain boundaries are shown. Especially their orientation to the applied stress plays an important role for the resulting stress distribution.

5.3.1.1 Single Grain Boundary Configurations

Grain Boundaries Parallel to the Applied Stress

In the first example, two parallel grain boundaries are implemented with an orientation parallel to the applied stress, i.e. they run from the bottom x line to the top x line as can be seen in Fig. 41. The boundary conditions as specified in Fig. 40 are applied.

The reacting stresses are depicted in Fig. 42. The x-component can be seen in part (a), the y-component in part (b). One can clearly see that the y-stress in the grain boundary is considerably lowered in contrast to the surrounding bulk material. The x-stresses are not influenced by the grain boundary. Grain boundaries with this orientation in comparison with the applied stress will act as a sink for vacancies.

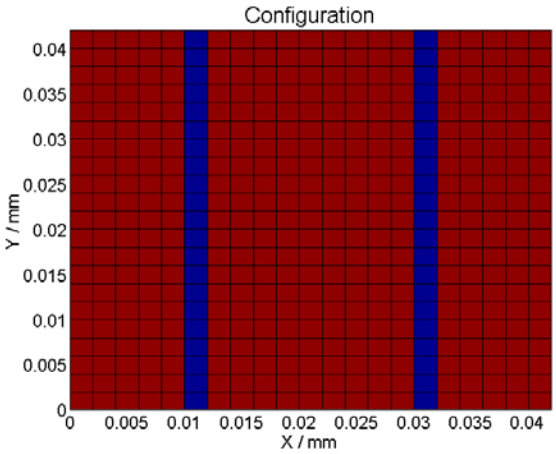

Fig. 41: Configuration of the two grain boundaries (blue) within a homogeneous bulk material (red) oriented parallel to the applied stress.

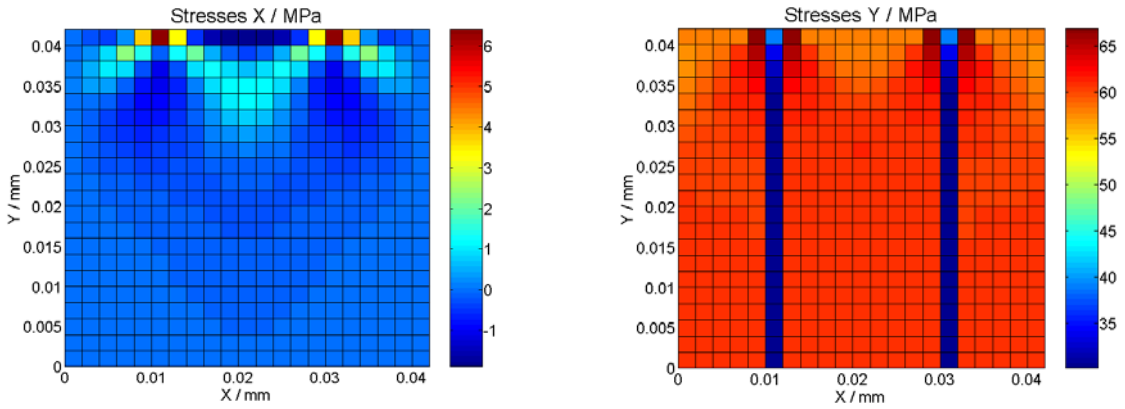

Fig. 42: (a) X-stresses and (b) y-stresses for grain boundaries in a homogeneous matrix oriented parallel to the applied stress.

Grain Boundaries Normal to the Applied Stress

In the next example, two parallel grain boundaries with orientation normal to the applied stress are implemented. In this case, for the x-component, an alteration in the stress distribution within the material is clearly calculated as depicted in Fig. 44 (a). In fact, within the matrix, the resulting x-stresses are of slightly compressive nature.

For the y-stresses, no alteration of the reacting internal stresses regarding the grain boundary-matrix interface can be observed. Thus, it clearly can be seen that the orientation of a grain boundary with respect to the applied stresses has a distinct influence on the reacting stress distribution within the material. Grain boundaries with this orientation in comparison with the applied stress can act as a source for vacancies.

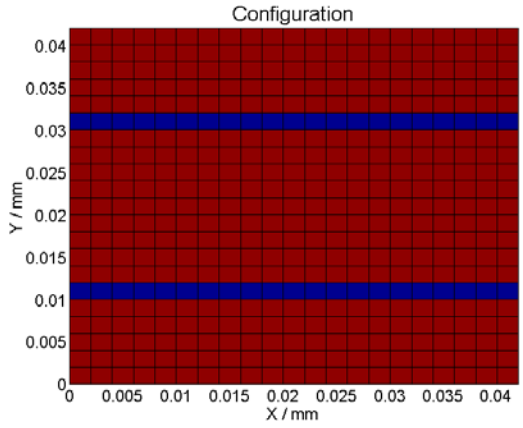

Fig. 43: Configuration of the two grain boundaries (blue) within a homogeneous bulk material (red) oriented normal to the applied stress.

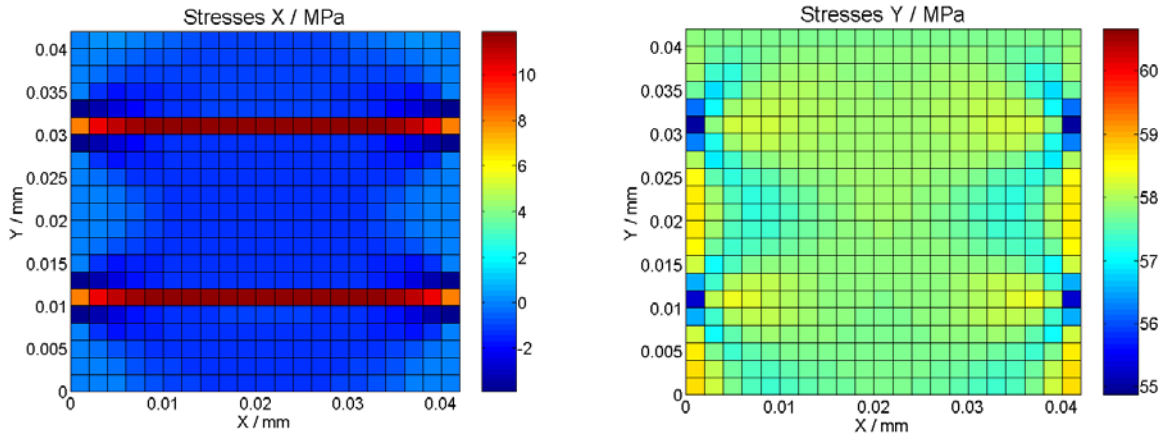

Fig. 44: (a) X-stresses and (b) y-stresses for grain boundaries in a homogeneous matrix oriented normal to the applied stress.

Diagonal Grain Boundaries

In this example, a diagonal grain boundary is implemented as can be seen in the configuration in Fig. 45. The y-component of the stress (Fig. 46 (a)) and the x-component (Fig. 46 (b)) are shown in the following graphs as well.

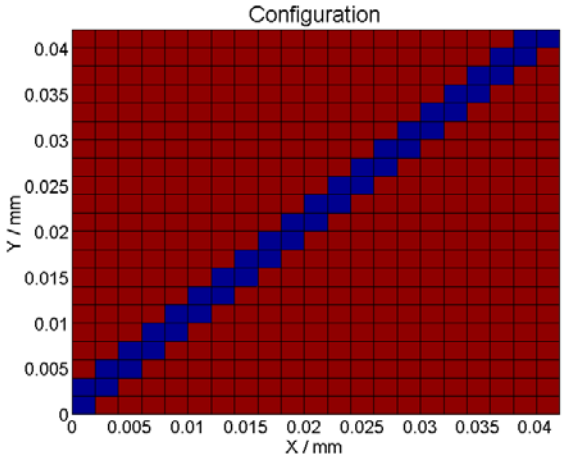

Fig. 45: Configuration of a grain boundary (blue) within a homogeneous bulk material (red) oriented diagonally to the applied stress.

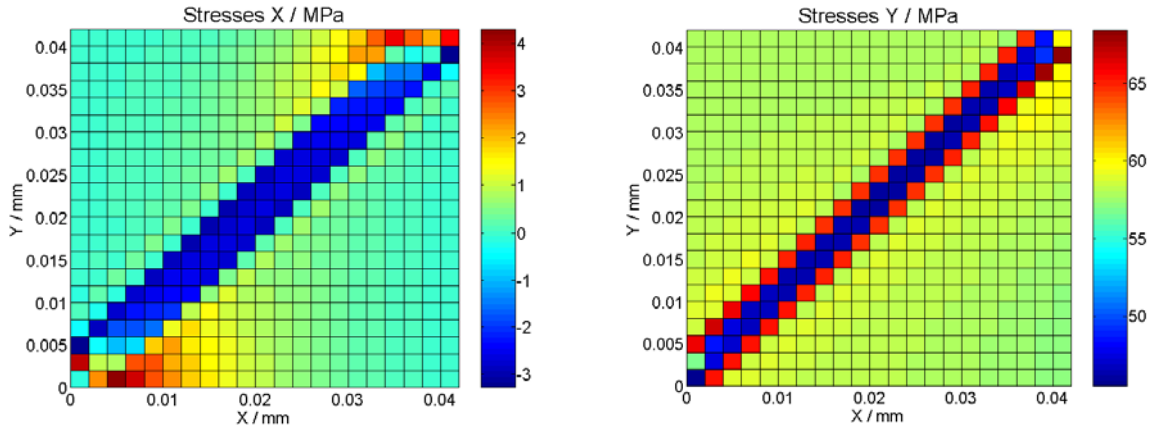

Fig. 46: (a) X-stresses and (b) y-stresses for a grain boundary in a homogeneous matrix oriented diagonally to the applied stress.

Again, the stress distribution within and in the vicinity of the grain boundary is affected. The y-stresses are lowered within the grain boundary, whereas, in the nearby area, the stresses are decreased. The x-components within the grain boundary are showing a slight compression compared to the matrix.

5.3.1.2 Combining Different Grain Boundaries.

Quadrilateral Grain

In this example, two parallel grain boundaries normal to the applied stress and two grain boundaries parallel to the applied stress are combined to a quadratic grain within in a bigger

homogeneous matrix. The whole grain has a dimension of about 20000 nm, as can be seen in the configuration in Fig. 47.

The internal x-stresses are depicted in Fig. 48. The boundaries, which are aligned normally to the applied stress, are not influencing the displayed stresses, their distribution remains homogeneous. In contrast, the two boundaries, which are oriented normally to the applied stress and are in line with the x-axis, are causing an increase of the x-component of the internal stress. These boundaries are assumed to act as a source for a vacancy flux.

The resulting stress distribution for the y-component of the internal stresses is shown in Fig. 49. It can clearly be seen that the two boundaries, which are oriented normally to the applied stress, do not influence the distribution of the displayed stresses. The situation is different for the grain boundaries, which are aligned parallel to the applied stress. In this case, the y-component of the resulting stresses is lowered clearly. These boundaries can act as a sink for the flux of vacancies.

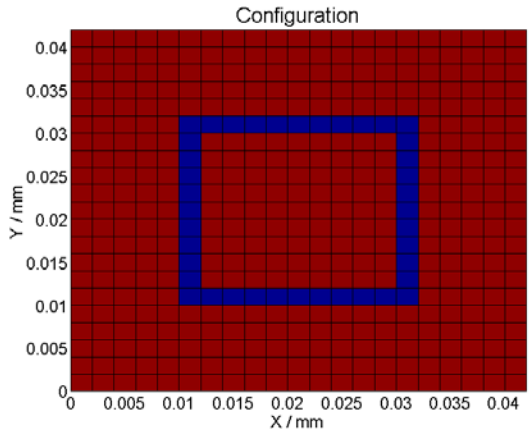

Fig. 47: Configuration of a quadrilateral grain (blue) within a homogeneous bulk material (red).

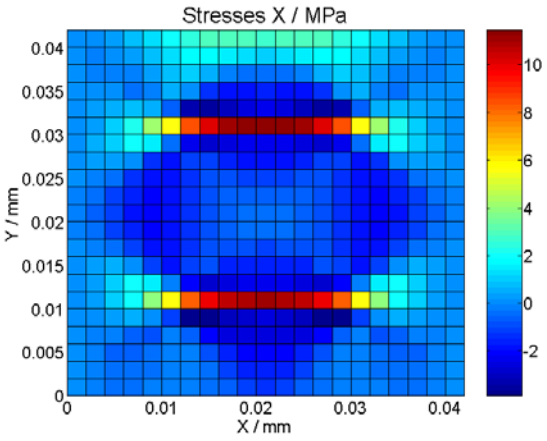

Fig. 48: X-stresses for a quadrilateral grain.

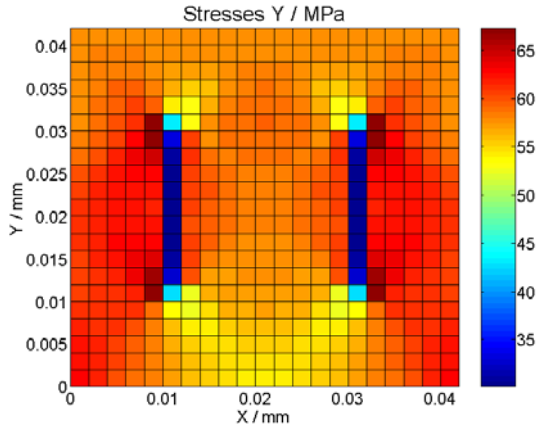

Fig. 49: Y-stresses for a quadrilateral grain.

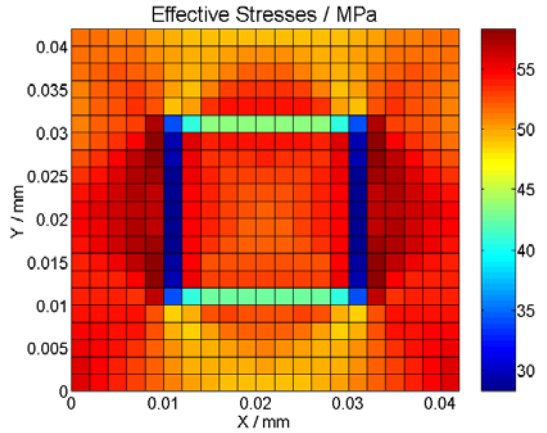

Fig. 50: Von Mises stresses for a quadrilateral grain.

To combine both stress components, the von-Mises stress is displayed in Fig. 50 for the quadratic grain within the homogenous matrix.

Triple Points

In the following examples, the resulting inner stresses caused by a triple point with a configuration as can be seen in Fig. 51 are discussed. The grain boundaries and the triple point again are embedded in a homogeneous matrix. The triple point is simulated for different values of the angle α as indicated in Fig. 51. Each specific configuration is presented in a separate graph, the grain boundaries are marked in blue, whereas the bulk material is displayed in red colour. The stress distributions are shown in the subsequent figures.

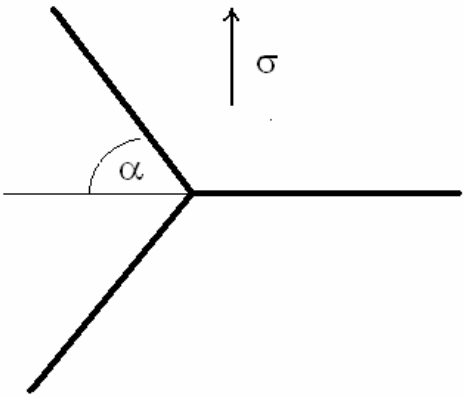

Fig. 51: Specifications for triple point simulations.

In Fig. 52 the configuration for the first example is presented. This configuration matches an angle α of 37.5°.

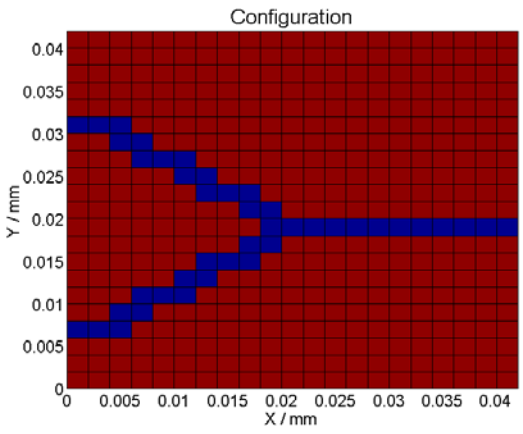

Fig. 52: Configuration of a triple point (blue) with an angle of 37.5° within a homogeneous bulk material (red).

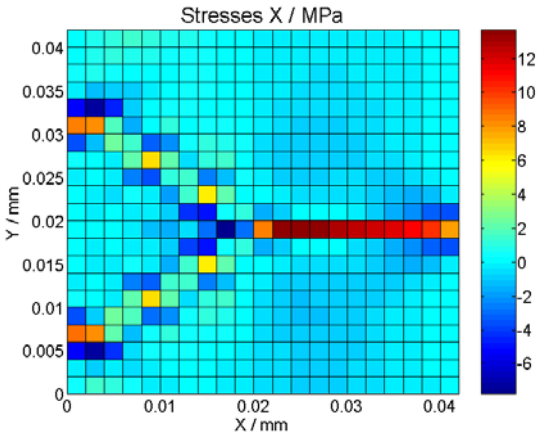

Fig. 53: X-stresses for the triple point.

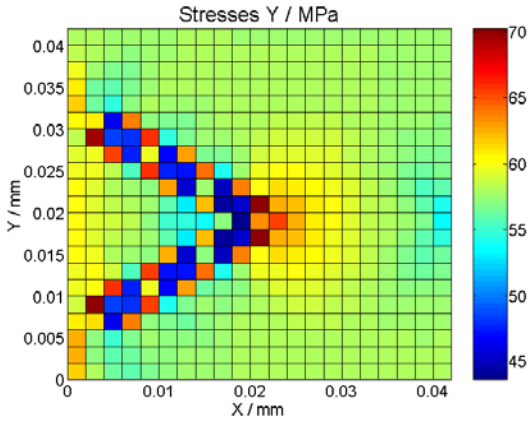

Fig. 54: Y-stresses for the triple point.

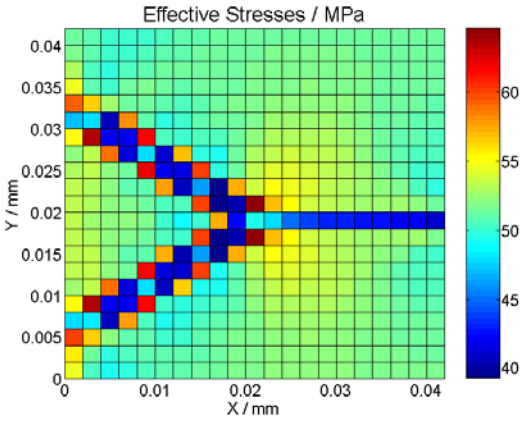

Fig. 55: Von Mises stresses for the triple point.

In Fig. 54, the y-component of the stress is depicted. The grain boundary normal to the applied stress shows no significant change in the stress distribution as is to be expected. The grain boundaries which run under the angle of 37.5° are causing an alteration in the displayed stress distribution in the similar way as was simulated in Fig. 45 to Fig. 46 for diagonal grain boundaries. The main focus of interest in this calculation is the triple point itself. As already outlined in section 3.1.6.1, Riedel [11] discusses stress distributions near triple junctions and claims that, in such configurations, the maximum tensile stress occurs on the boundary normal to the applied stress. The calculated stress distributions are in perfect agreement with this statement.

In Fig. 53, the x-component of the reacting stresses is shown. For this case, compressive stresses in the vicinity of the triple point within the angle α can be seen.

The effective stresses of this sample are calculated in Fig. 55. Again, the influence of the triple point is obvious.

For a comparison, in the next example, a triple point with an angle of $\alpha = 45°$ is simulated. The arrangement of the triple point is shown in Fig. 51. The boundary conditions are the same as in the previous examples.

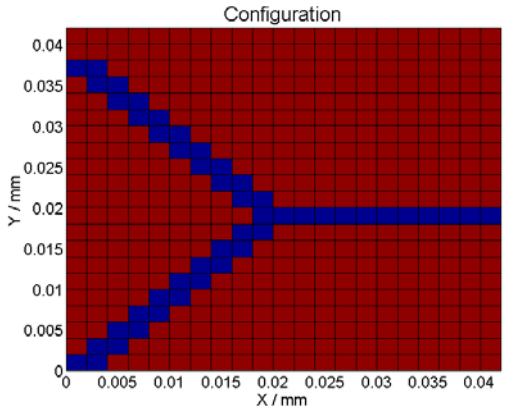

Fig. 56: Configuration of a triple point (blue) with an angle of 45° within a homogeneous bulk material (red).

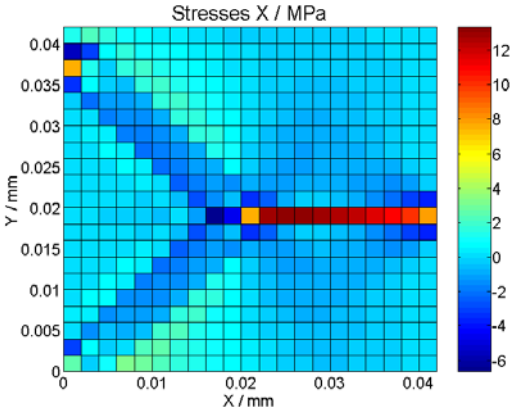

Fig. 57: X-stresses for the triple point.

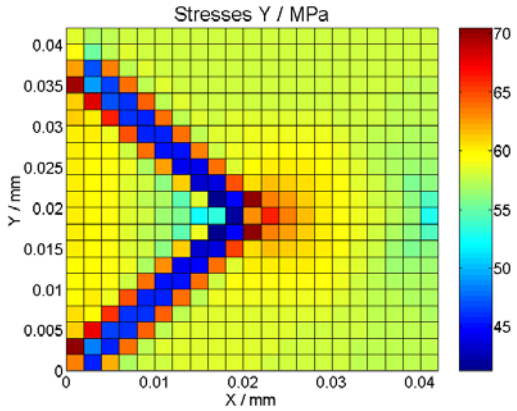

Fig. 58: Y-stresses for the triple point.

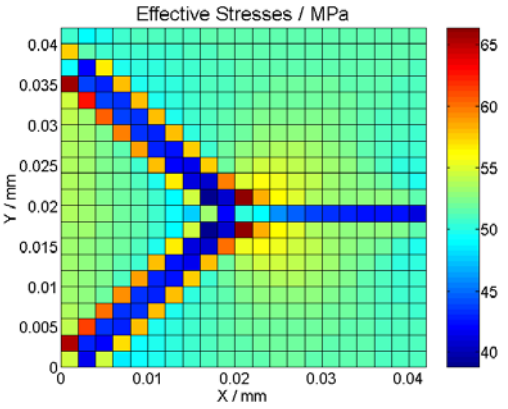

Fig. 59: Von Mises stresses for the triple point.

The x-component of the stress distribution is shown in Fig. 57, the y-stresses in Fig. 58 and the effective stress in Fig. 59. The findings are similar to those of the triple point with an angle of 37.5°, but the stress inhomogeneities are bigger and the tensile stress near the triple point is higher.

As a third example for triple point configuration under different angles, a triple point with α = 60° is modelled. Fig. 60 shows the configuration, Fig. 61 is depicting the y-and Fig. 62 the x-component of the internal stress distribution. Fig. 63 shows the effective internal stresses.

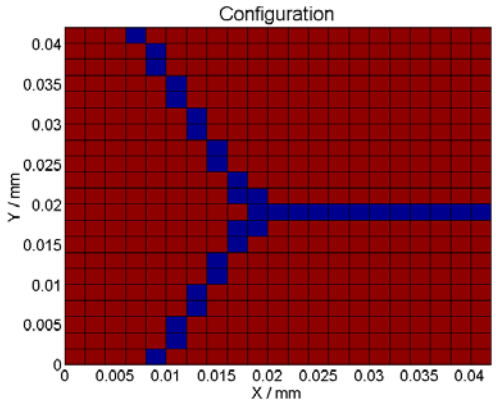

Fig. 60: Configuration of a triple point (blue) with an angle of 60° within a homogeneous bulk material (red).

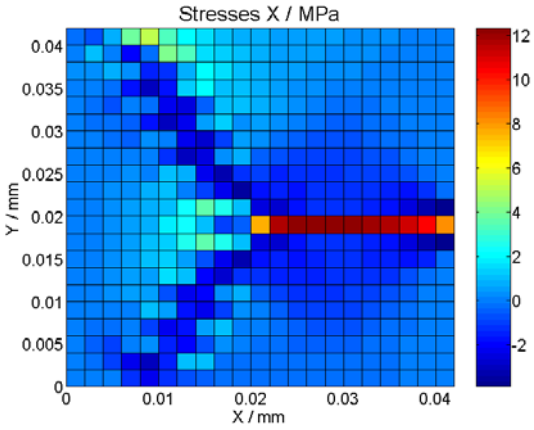

Fig. 61: X-stresses for the triple point.

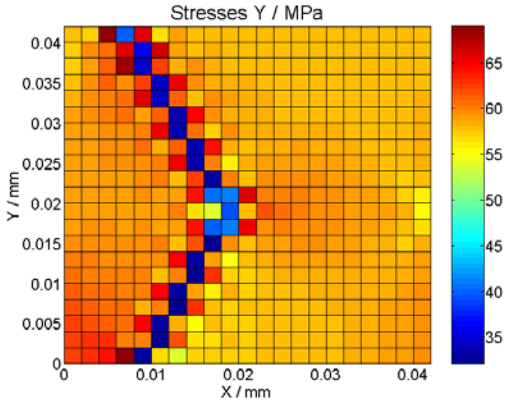

Fig. 62: Y-stresses for the triple point.

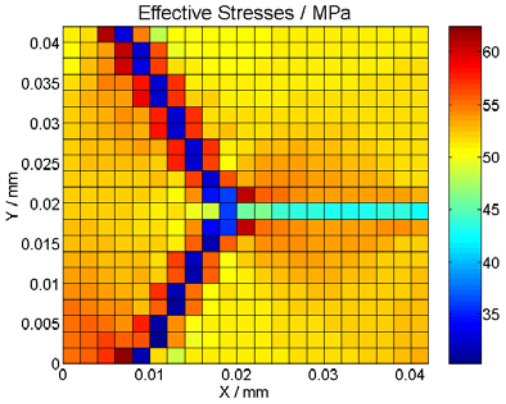

Fig. 63: Von Mises stresses for the triple point.

When comparing all three triple point configurations, the results show that the inhomogeneities are biggest for an angle of 45°.

As a final example for triple point configurations, a triple point with alpha = 45° but with a different orientation with respect to the applied stress is modelled. Fig. 64 shows the configuration. Fig. 65 and Fig. 66 are showing the y- and the x-component of the internal stress distribution Fig. 67 depicts the effective internal stresses The tensile stresses in the element next to the triple point once again are increased.

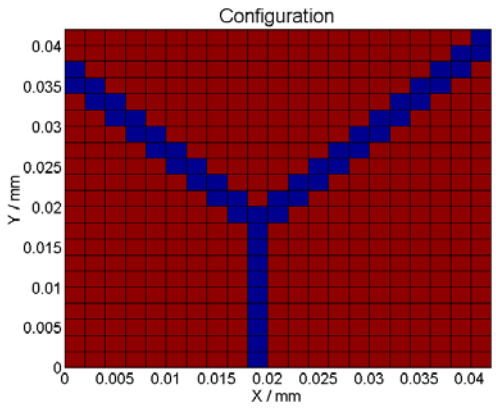

Fig. 64: Configuration of a triple point (blue) with an angle of 45° within a homogeneous bulk material (red).

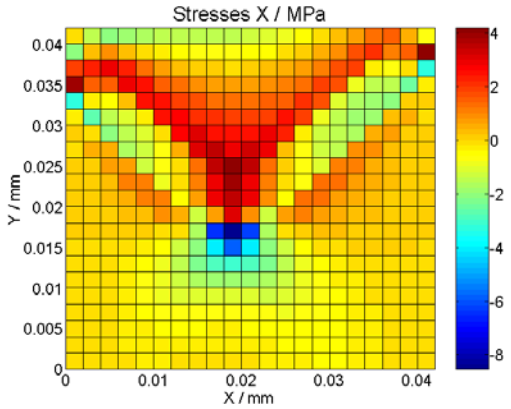

Fig. 65: X-stresses for the triple point.

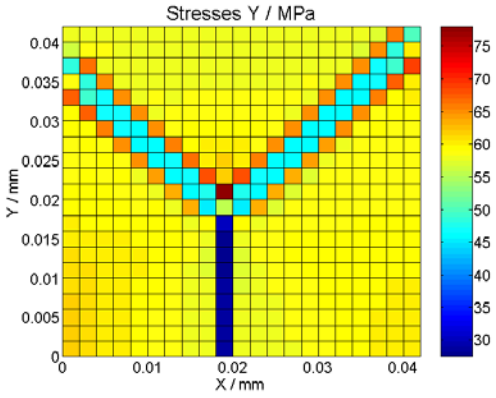

Fig. 66: Y-stresses for the triple point.

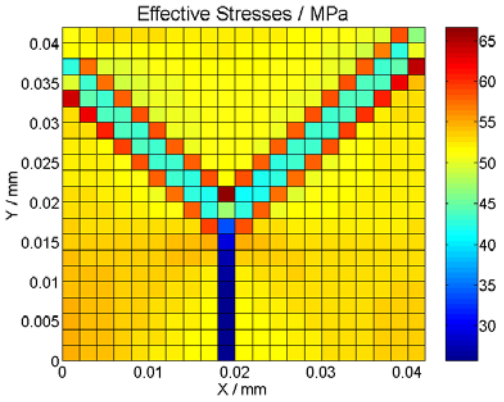

Fig. 67: Von Mises stresses for the triple point.

Hexagonal Grain

A grain is usually surrounded by several grain boundaries. In 2D, an equilibrium configuration consists of 6 boundaries forming a hexagonal grain. The boundary conditions for this example again are the same as in the previous calculations. In this example, and as well in the following ones, the grain boundaries are marked in dark blue colour to highlight the stress distributions within the bulk material itself. In Fig. 68, the configuration of the grain

itself is shown. In Fig. 69 and Fig. 70, the x-and the y-component of the internal stresses are depicted and Fig. 71 presents the effective stresses in the grain.

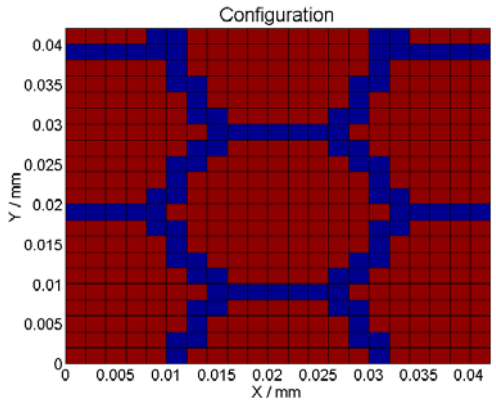

Fig. 68: Configuration of a hexagonal grain with grain boundaries in blue colour consisting of a homogeneous bulk material (red).

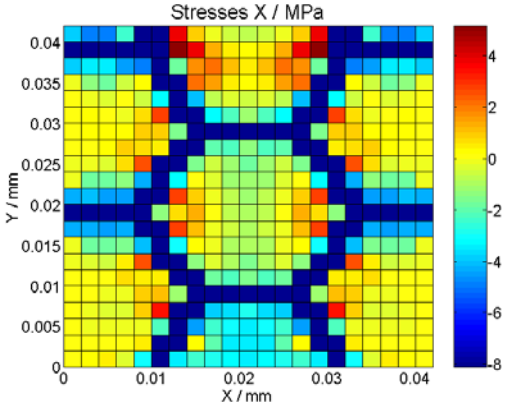

Fig. 69: X-stresses for the hexagonal grain.

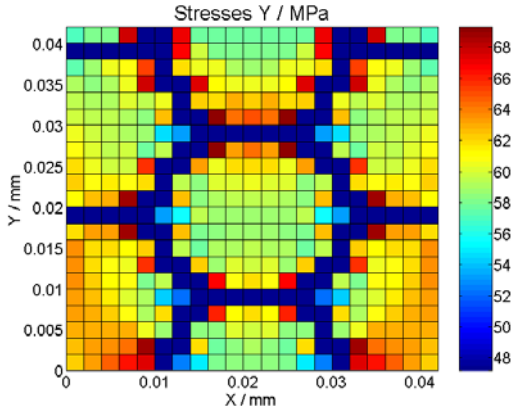

Fig. 70: Y-stresses for the hexagonal grain.

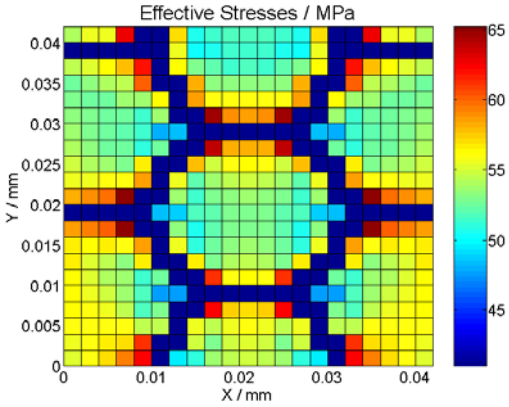

Fig. 71: Von Mises stresses for the hexagonal grain.

Once again, the orientation of the grain boundaries versus the applied stress plays an important role in the stress distribution within the material. All triple points of the depicted hexagonal grain are causing a distinct increase in the local stress distribution nearby. The grain boundaries themselves play an important role as well resulting in a clearly inhomogeneous stress distribution, where especially the grain interior is subjected to lower reacting stresses compared to the vicinity of grain boundaries oriented normally to the applied stress.

5.3.2 Implementing Hard Particles

In a multi-phase environment, hard particles can lead to stress concentrations as well. Again, for the simulation, a grid of 21x21 elements is used. The boundary conditions are the same as

specified in Fig. 40 and consist of a fixation on the bottom x-line of the grid and an applied stress on the upper border of the specimen. The internal stresses for each element are calculated at the four Gauß points. In each element, a mean value is displayed.

5.3.2.1 One Hard Particle

In the following example, the stress distribution caused by a hard carbide precipitate in a softer matrix is modelled. The precipitate is embedded in the softer matrix. In each of the following figures, it is coloured in dark blue. Its elastic modulus is assumed to be twice the modulus of the bulk material.

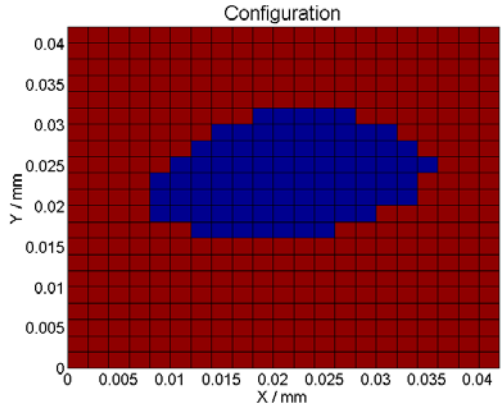

Fig. 72: Configuration for a particle (blue) embedded in a homogeneous bulk material (red).

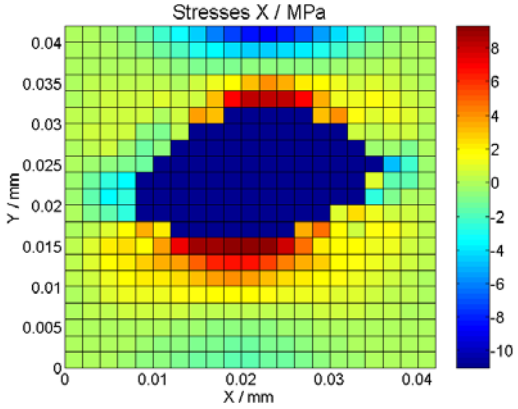

Fig. 73: X-stresses for the particle.

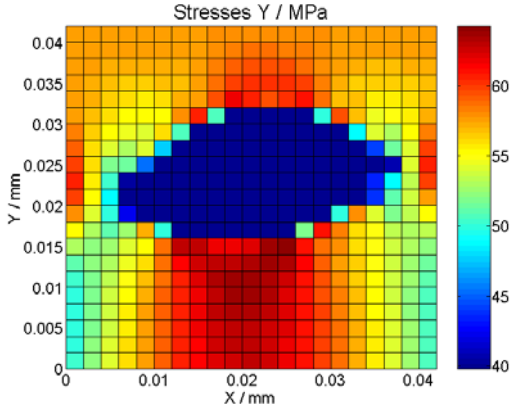

Fig. 74: Y-stresses for the particle.

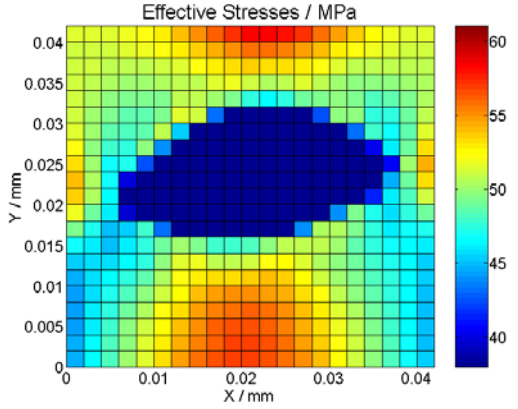

Fig. 75: Effective stresses for the particle.

In Fig. 73, the x-component of the reacting internal stress distribution is shown. Near the normal oriented faces, the tensile stress is increased, whereas, near the parallel oriented faces, compressive stress occurs. In Fig. 74, the y-component of the reacting stresses is displayed. In the regions near the faces oriented normal to the y-axis, the stress is clearly increased compared to the regions near the faces oriented parallel to the applied stress. In Fig. 75, the effective stress distribution is depicted.

5.3.2.2 Two Smaller Particles

As a further example, the stress inhomogeneity caused by two smaller particles is calculated. All parameters and boundary conditions are the same as in the previous simulation Again, the elastic modulus of the precipitate is assumed to be twice the modulus of the surrounding matrix. Each particle is coloured in dark blue in all graphs.

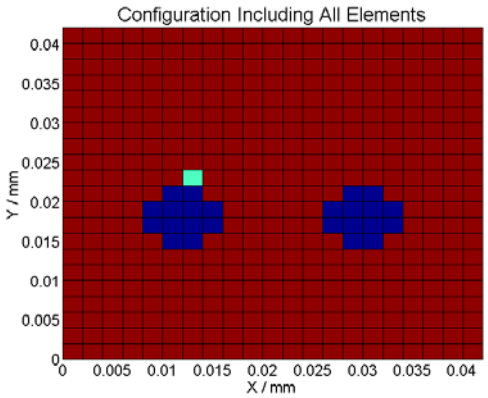

Fig. 76: Configuration for two small particles (blue) embedded in a homogeneous bulk material (red).

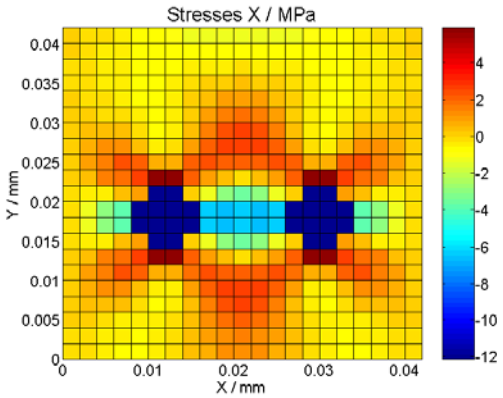

Fig. 77: X-stresses for the particles.

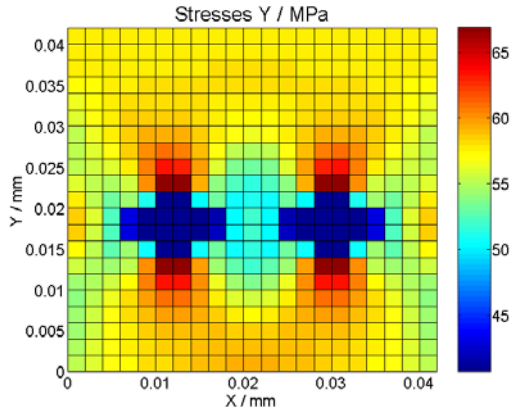

Fig. 78: Y-stresses for the particles.

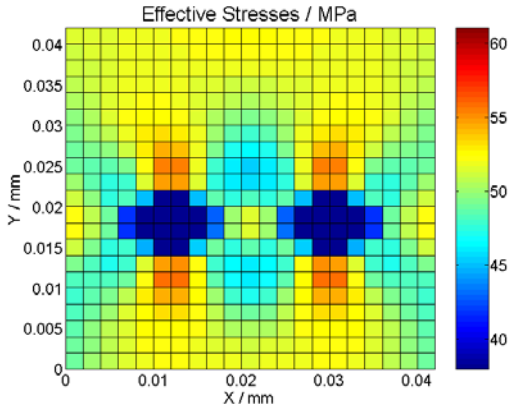

Fig. 79: Effective stresses for the particles.

In Fig. 78, the y-component of the reacting stresses is depicted. The results are similar to those calculations for one hard particle in the previous example. On the boundaries oriented normal to the applied stress, the stresses are increased significantly. Near all faces parallel to the applied stresses, the y-component is decreased. In the area between these two particles stresses are lowered as well. In Fig. 77, the x-component is shown. Near the normal oriented faces, the tensile stress is increased, whereas, near the parallel oriented faces, compressive

stress occurs. In Fig. 79 the effective stress distribution can be seen. The stress pattern is about the same as for the y-component of the reacting stresses.

5.4 Creep Behaviour of the Microstructure

As already outlined in chapter 3, the creep strains within a microstructure show a distinct pattern due to the inhomogeneities of this particular microstructure. In this section, the results of the simulations in terms of creep stresses and strains are presented. All parameters are chosen according to Table 4 in section 5.1.

5.4.1 Stress Relaxation on Triple Points

Triple Points in an otherwise homogeneous matrix are causing elastic stress concentrations as shown in the previous section and as stated by Riedel [11]. These stress concentrations are reduced by creep, resulting in a heterogeneous creep strain distribution. The transition from an elastic situation to creep loading can be described by the growth of a creep zone nearby the triple points (see section 3.1.6.1).
In all simulations presented in the following sections, stress versus time diagrams for a particular point within the microstructure are shown. To clarify for which specific element these curves are calculated, this particular element is always highlighted in green colour in the configuration overview.

To illustrate the stress-relaxing effect of creep, a simulation of a triple point within in a crystalline matrix is conducted. The grid contains 21x21 elements, the triple point has an opening angle of 90°. Again, a load resulting in an effective stress of 50 MPa is applied. The configuration is depicted in Fig. 80. Fig. 81 shows the initial, purely elastic situation containing a maximum stress concentration on the grain boundary oriented normally to the applied stress. Then, the sample is subjected to a creep load for an overall time of 10000 hours. The evolution of the von Mises stress distribution can be seen in Fig. 81 to Fig. 84. Fig. 82 shows the situation after t = 1000 hours, Fig. 83 after t = 4000 hours and Fig. 84 at the end of the interval. The relaxation of the initial stress concentration due to creep can be clearly seen.

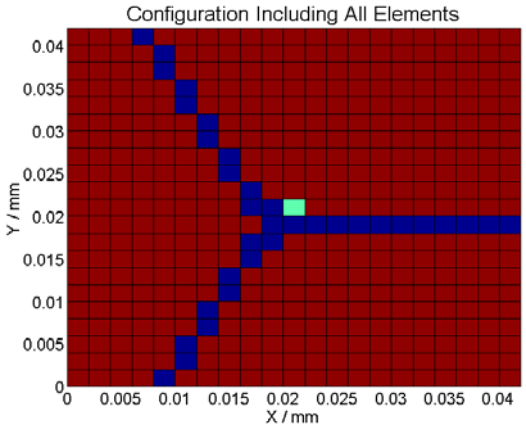

Fig. 80: Configuration for a triple point (blue) embedded in a homogeneous bulk material (red); the bulk material element for which particular stress graphs are presented in the following figures is highlighted in green.

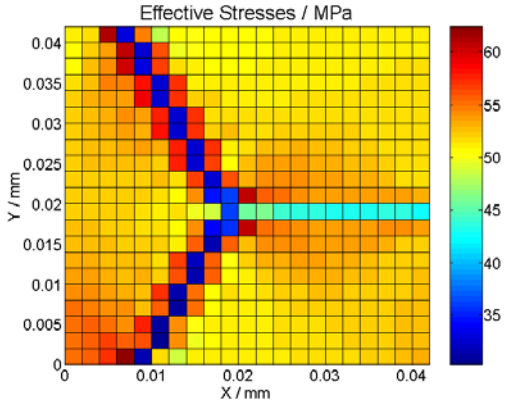

Fig. 81: Effective stress distribution in the vicinity of a triple point exposed to a creep load – initial stress distribution.

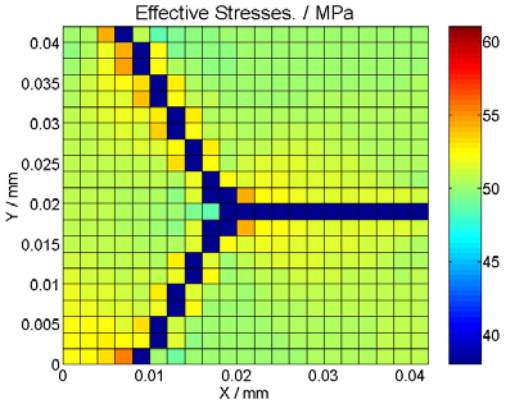

Fig. 82: Effective stress distribution after t = 1000h.

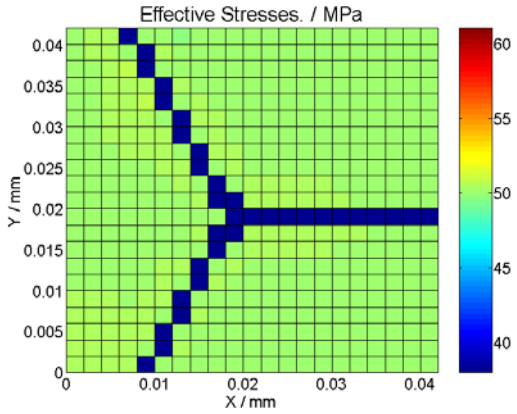

Fig. 83: Effective stress distribution after t = 4000h.

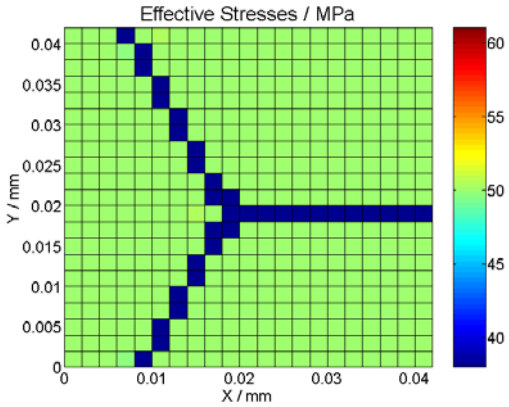

Fig. 84: Effective stress distribution after t = 10000h.

In Fig. 85, the evolution of the von Mises stress in the bulk element directly located at the triple point, as highlighted in Fig. 80 in green colour, is shown. The stress clearly decreases in

time during creep. The growth of the creep zone in the vicinity of the triple point and the grain boundaries, which again are marked in dark blue colour, can be seen in Fig. 86.

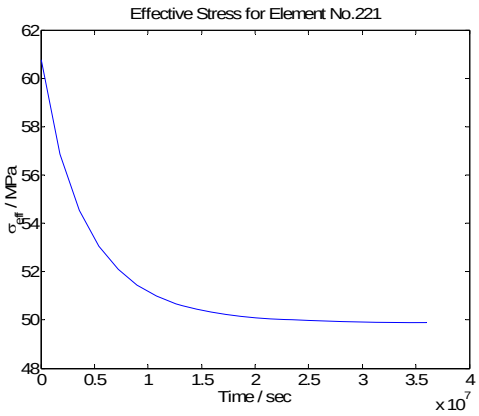

Fig. 85: Evolution of the effective stress vs. time in the bulk material located directly near the triple point for *t* = 10000h.

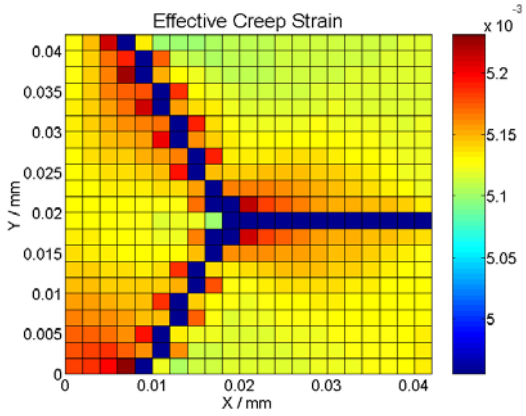

Fig. 86: Effective creep strain distribution after *t* = 10000h.

For comparison, the same sample with a diffusion coefficient ten times smaller then the previous one has been calculated. In Fig. 87 the stress decrease of the same element as in Fig. 85 is depicted. It can clearly be seen, that the relaxation takes longer, but has the same characteristics.

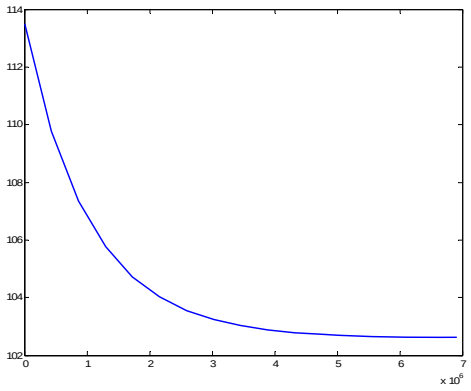

Fig. 87: Development of the effective stress vs. time in the bulk material located directly near the triple point for a diffusion coefficient ten time smaller than in all other calculations.

5.4.2 Creep of a Hexagonal Grain

In this example, the creep behaviour of a hexagonal grain exposed to creep is evaluated. The grid contains 21x21 elements. Again, a load of 50 MPa is applied. Fig. 88 depicts the initial, purely elastic situation with the maximum stress concentration near the grain boundaries oriented normally to the applied stress. The evolution of the von Mises stress distribution can be seen in Fig. 89 to Fig. 91 Fig. 89 shows the situation after *t* = 1000 hours, Fig. 90 after *t* =

4000 hours and Fig. 91 at t = 10000 hours. Again, the relaxation of the initial stress concentrations to long term behaviour can clearly be seen.

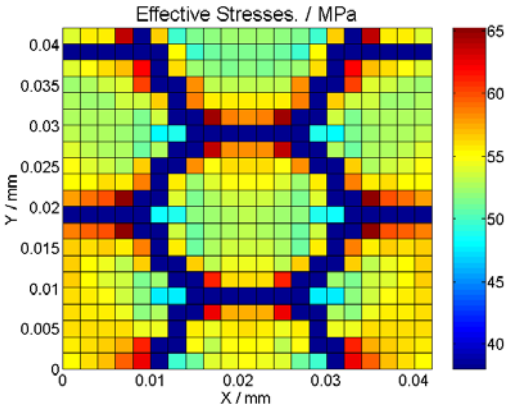

Fig. 88: Effective stress distribution for a hexagonal grain exposed to a creep load – initial stress distribution.

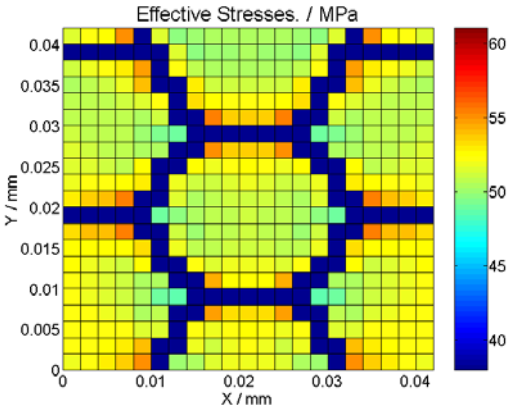

Fig. 89: Effective stress distribution after t = 1000h.

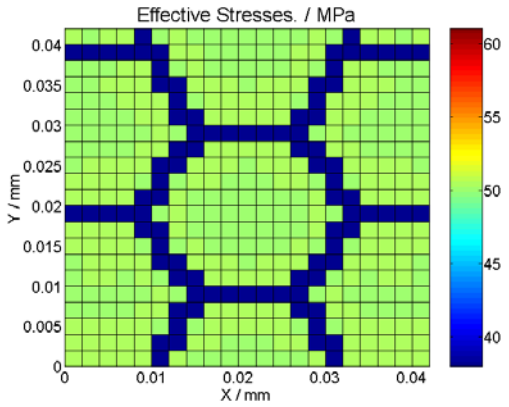

Fig. 90: Effective stress distribution after t = 4000h.

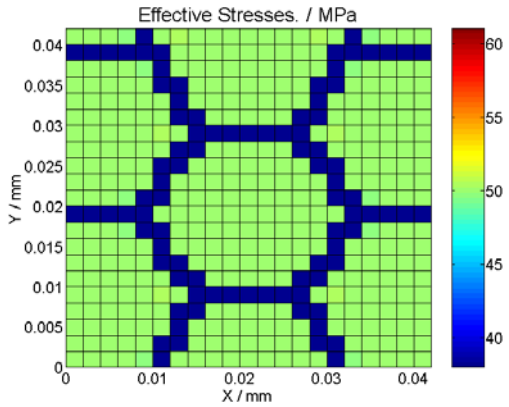

Fig. 91: Effective stress distribution after t = 10000h.

In Fig. 92, the creep strain of the specimen is shown. The creep strain again shows a locally differing distribution. Especially, the bulk material adjacent to the grain boundaries oriented normally to the applied stress is exposed to pronounced creep straining.

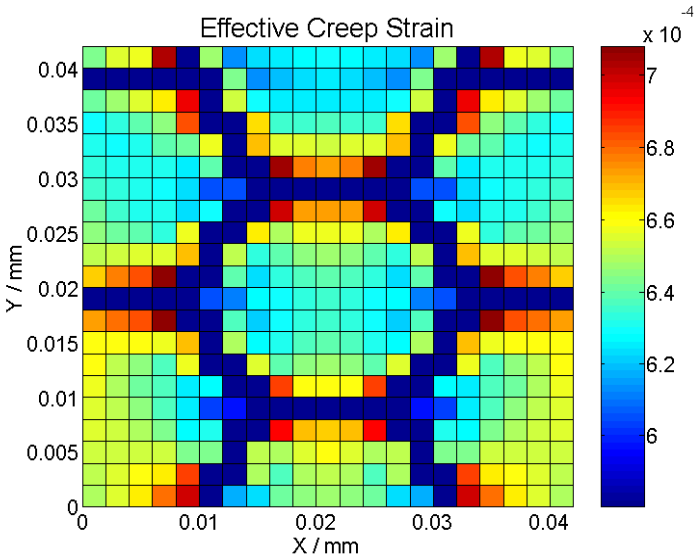

Fig. 92: Effective creep stain distribution for a hexagonal grain exposed to a creep load after t = 10 000 h.

5.4.3 Creep in the Presence of Hard Particles

Precipitates play an important role in microstructure evolution. One of these effects is their manifold influences in local creep behaviour. Thus, the creep behaviour of a matrix with two embedded hard particles is calculated. The parameters are the same as in the previous calculations. The hard particles clearly influence the straining behaviour of the sample. The creep deformation of the bulk material surrounding the particles clearly reduces the internal stresses, as is depicted in Fig. 94 to Fig. 97 for the effective stress distribution.

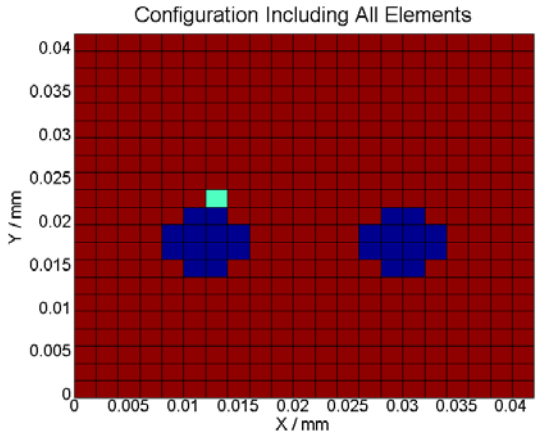

Fig. 93: Configuration for two particles (blue) embedded in a homogeneous bulk material (red); the bulk material element for which particular stress graphs are presented in the following figures is highlighted in green colour.

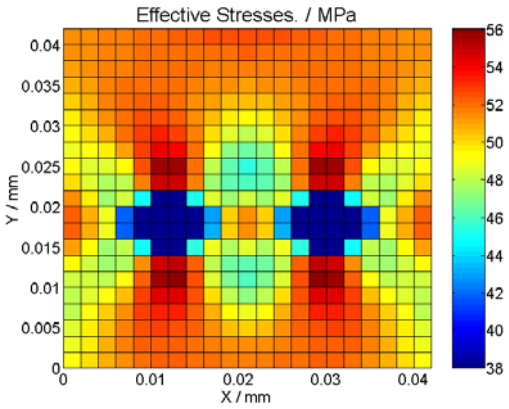

Fig. 94: Effective stress distribution in the vicinity of two hard particles – initial stress distribution.

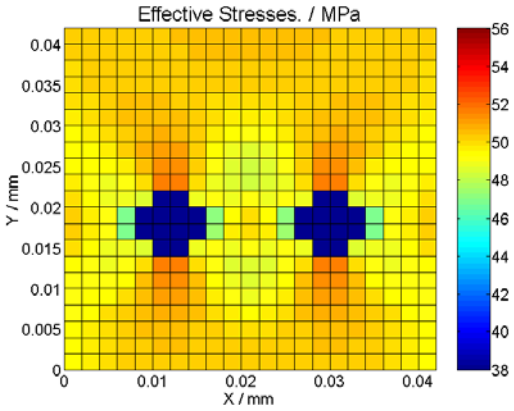

Fig. 95: Effective stress distribution after t = 1000h.

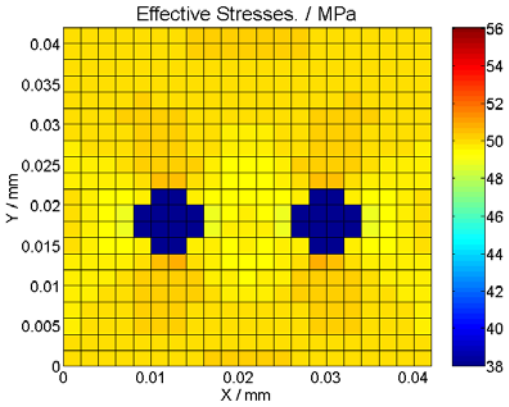

Fig. 96: Effective stress distribution after t = 2000h.

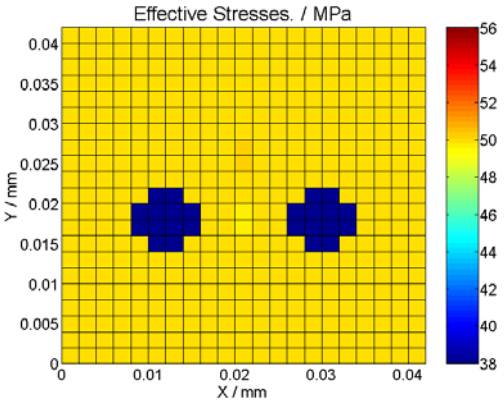

Fig. 97: Effective stress distribution after t = 6000h.

The evolution in time of the von Mises stresses in the vicinity of such a hard particle is depicted in Fig. 98. Again, creep straining decreases the initial elastic stresses in time. Furthermore, an inhomogeneous distribution of the actual creep strain evolves, as is shown in Fig. 99. Especially, at particle faces oriented normally to the applied stress, a significant accumulation of creep strain is calculated, whereas in areas between the particles, a smaller effective creep strain is predicted.

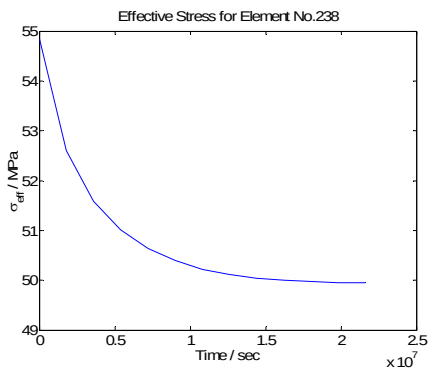

Fig. 98: Evolution of the effective stress vs. time in the bulk material located directly near one precipitate for t = 6000h.

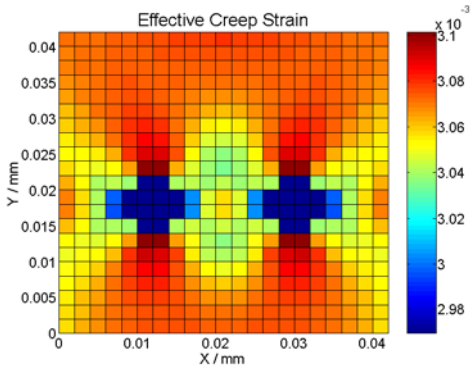

Fig. 99: Effective creep strain distribution after t = 6000h.

5.4.4 Hard Particles and Grain Boundaries

Triple points are causing stress singularities within the internal stress distribution. The same holds true for hard particles. To study possible interactions some examples for different configurations of both are calculated and presented in the next section.

5.4.4.1 Hard Particle on a Triple Point of a Grain Boundary

As first example, a hard particle, which is located directly on a triple point, is calculated. In Fig. 100, the configuration is depicted. In Fig. 101, the initial distribution of the effective stress is shown. The hard particle increases the stress singularity in the vicinity of the triple point. As in the previous examples, creep deformation leads to stress relaxation and the internal stresses are levelled out, as can be seen in Fig. 102 for t = 1000 hours and in Fig. 103 for t = 10000 hours.

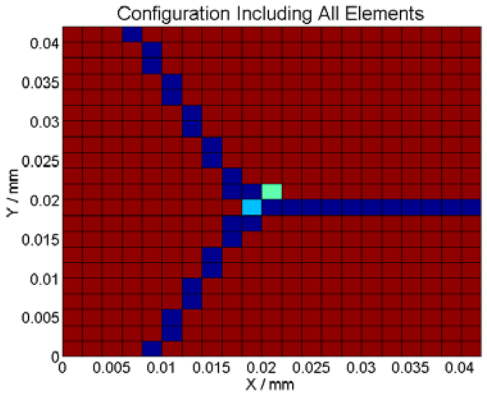

Fig. 100: Configuration for a triple point (dark blue) containing a hard particle (light blue) embedded in a homogeneous bulk material (red); one bulk material element is highlighted in green colour.

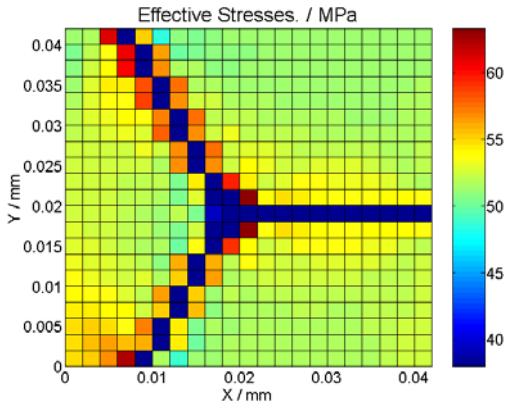

Fig. 101: Effective stress distribution in the vicinity of the triple point – initial stress distribution.

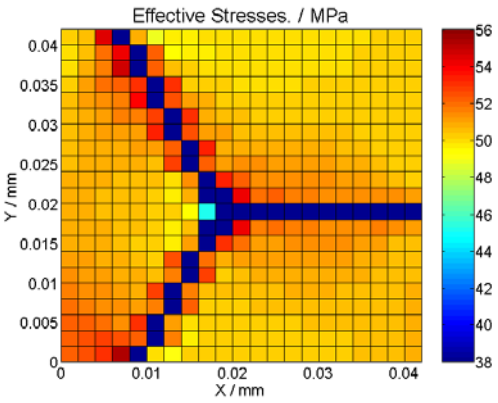

Fig. 102: Effective stress distribution after t = 1000h.

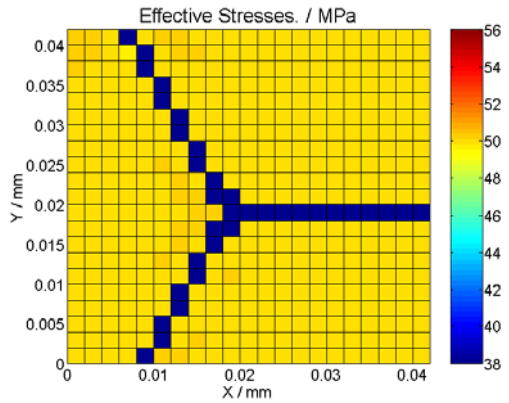

Fig. 103: Effective stress distribution after t = 10000h.

In Fig. 104, the stress relaxation for the element near the triple point (marked in green in Fig. 100) is depicted by the evolution of the effective stress versus time. The resulting creep strain can be seen in Fig. 105. Compared to the stress relaxation for a triple point containing no particles (see section 5.4.1), the effective stress right upon loading is increased by about 3%, whereas the stresses after relaxation reach the same equilibrium values.

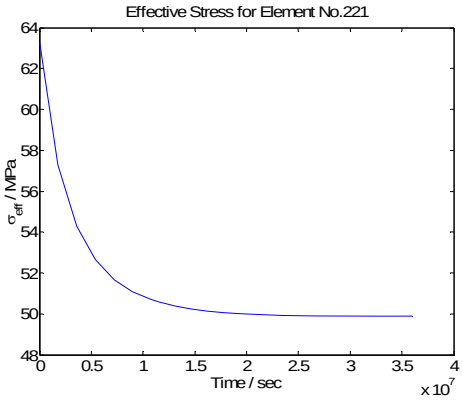

Fig. 104: Evolution of the effective stress vs. time in the bulk material located directly at the triple point for *t* = 10000h.

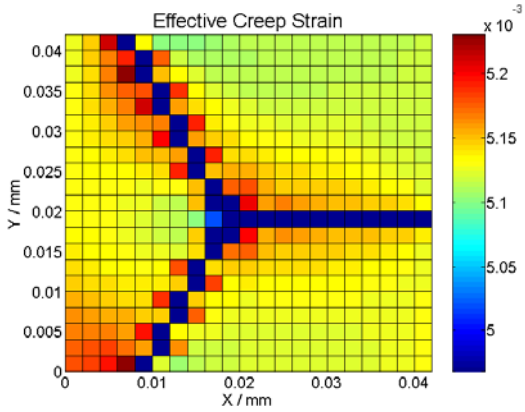

Fig. 105: Effective creep strain distribution after *t* = 10000h.

5.4.4.2 Hard Particle Near a Triple Point of a Grain Boundary

In contrast to the previous example, in this case, a hard particle is not located directly at the triple point, but in its nearby vicinity. In Fig. 106, the configuration is depicted. In Fig. 107, the initial distribution of the effective stress is shown. As in the previous examples, these stresses are relaxing in the same manner, leading to a homogeneous stress distribution as in the previous simulations and thus is not shown separately here. Again, the stress concentration in the nearby area is increased after load application, but the amount is smaller than in the case of a particle directly located at the triple point. The relaxation of this concentration versus time can be seen in Fig. 108. The resulting creep strain can be seen in Fig. 109. Remarkably, the creep strain in the vicinity of the particle is more pronounced than in the nearby vicinity of the triple point. In this case, especially the combination of a hard particle and the softer grain boundary can be held responsible for this effect.

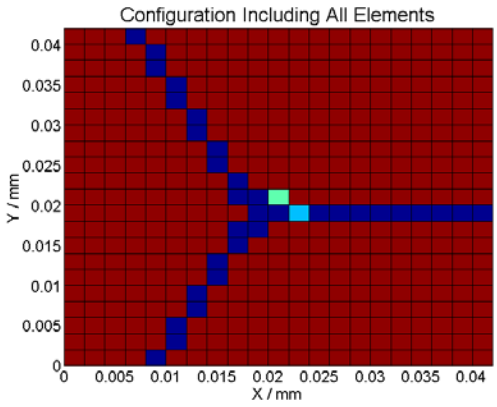

Fig. 106: Configuration for a triple point (dark blue) with a hard particle nearby (light blue) embedded in a homogeneous bulk material (red); one bulk material element is highlighted in green colour.

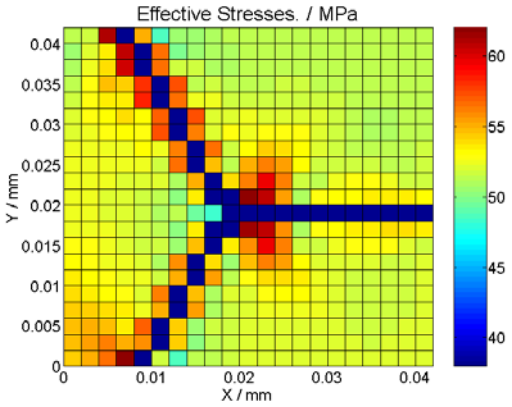

Fig. 107: Effective stress distribution in the vicinity of the triple point – initial stress distribution.

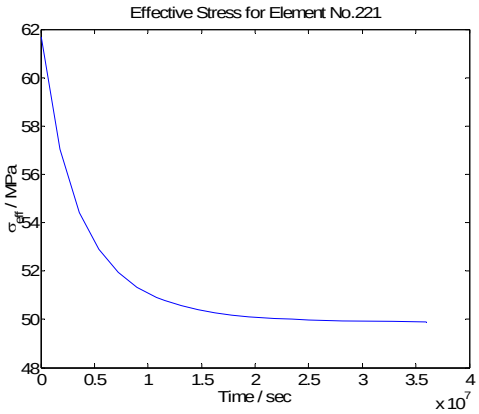

Fig. 108: Evolution of the effective stress vs. time in the bulk material located directly near the triple point for t = 10000h.

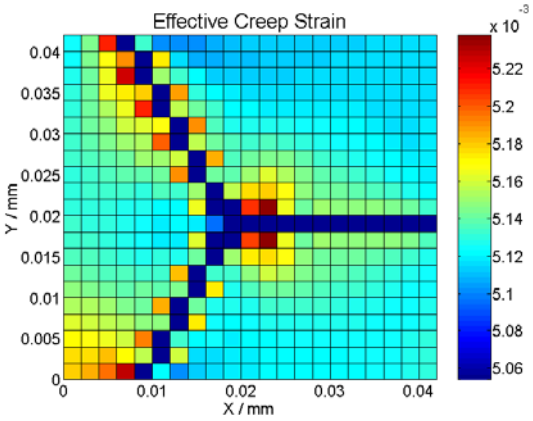

Fig. 109: Effective creep strain distribution after t = 10000h.

5.4.4.3 Hard Particle Near a Triple Point Within Larger Distance

As a third example, again, a triple point with a particle in its nearby area is considered, however, the distance between the particle and the triple point is increased. In Fig. 110, the configuration is depicted. In Fig. 111, the initial distribution of the effective stress is shown. As in the previous example, the evolution of stress distribution is not shown separately. In Fig. 112, the stress relaxation near the triple point is depicted by the evolution of the effective stress versus time. In this case, the hard particle does not increase the stress singularity. The influence is smaller due to the larger distance between the triple point and the particle. The behaviour of both microstructural elements can be regard as being independent. The resulting creep strain is shown in Fig. 113.

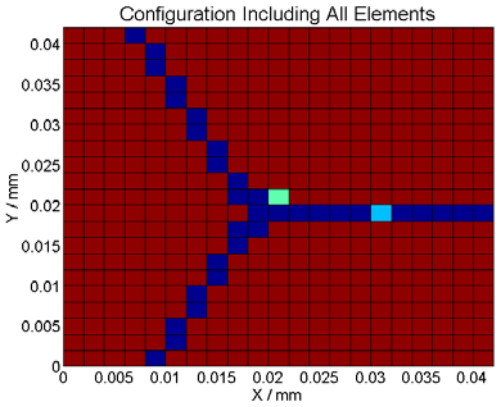

Fig. 110: Configuration for a triple point (dark blue) with a hard particle nearby (light blue) embedded in a homogeneous bulk material (red); one bulk material element is highlighted in green colour.

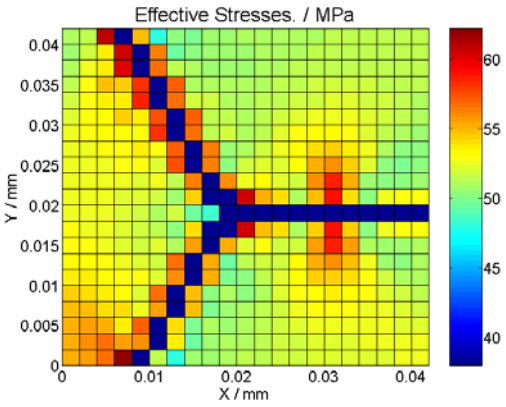

Fig. 111: Effective stress distribution in the vicinity of the triple point – initial stress distribution.

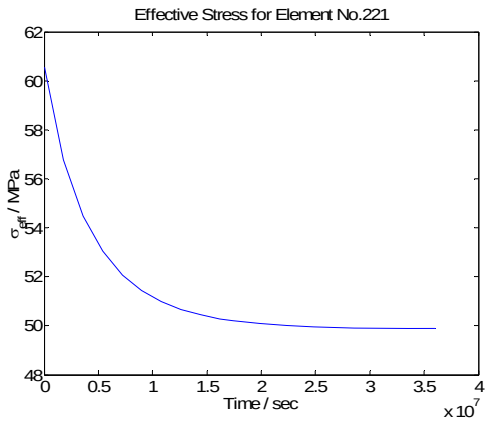

Fig. 112: Evolution of the effective stress vs. time in the bulk material located directly near the triple point for t = 10000h.

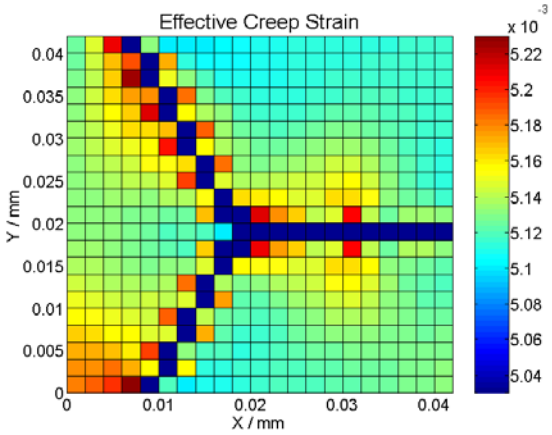

Fig. 113: Effective creep strain distribution after t = 10000h.

5.4.4.4 A Large Particle Near a Triple Point of a Grain Boundary

As another example, the influence of a triple point of a grain boundary and a large precipitate in its vicinity is studied. In Fig. 114, the configuration is shown. In Fig. 115, the initial distribution of the stresses is depicted.

In Fig. 116, the stress relaxation near the triple point is depicted by the evolution of the effective stress versus time. In this case, the hard particle even decreases the stress singularity near the triple point by a minor amount compared due to the same triple junction without any precipitates. The resulting creep strain is depicted in Fig. 117.

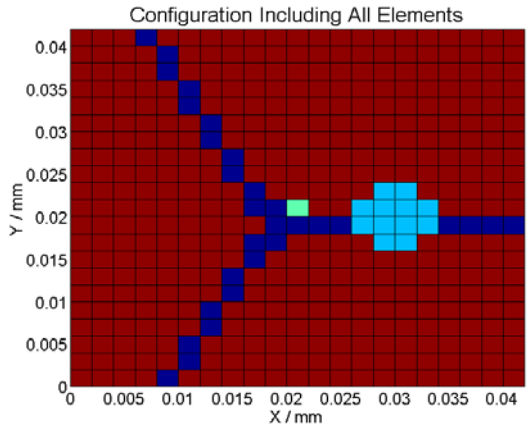

Fig. 114: Configuration for a triple point (dark blue) and a large hard particle (light blue) embedded in a homogeneous bulk material (red); one bulk material element is highlighted in green colour.

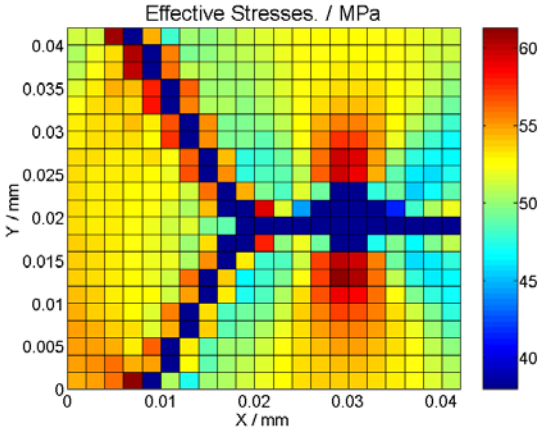

Fig. 115: Effective stress distribution in the vicinity of the triple point and the particle – initial stress distribution.

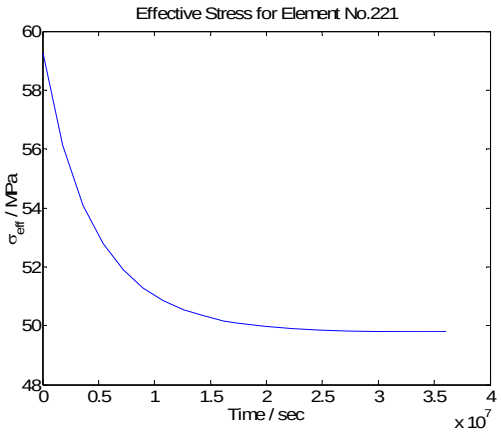

Fig. 116: Evolution of the effective stress vs. time in the bulk material located directly near the triple point for *t* = 10000h.

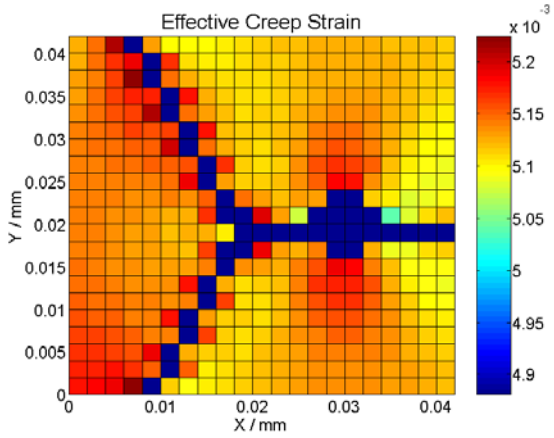

Fig. 117: Effective creep strain distribution after *t* = 10000h.

5.4.4.5 Creep of a Complex Microstructure

As a final example, the creep strains in a larger part of a microstructure are simulated. The structure contains several hexagonal grains separated by grain boundaries, as shown in Fig. 118. Additionally, hard particles of two different sizes are implanted. To show the various influences of all components, the grid is divided into different areas containing different elements of the above mentioned microstructural components. In the lower right part, only grain boundaries forming hexagonal grains are calculated. In the lower left part, some large particles are added. In the upper part of the figure, small particles can be seen, where, in the

upper left part, the particles are located at the grain boundaries, and, in the upper right part, they are embedded in the bulk material.

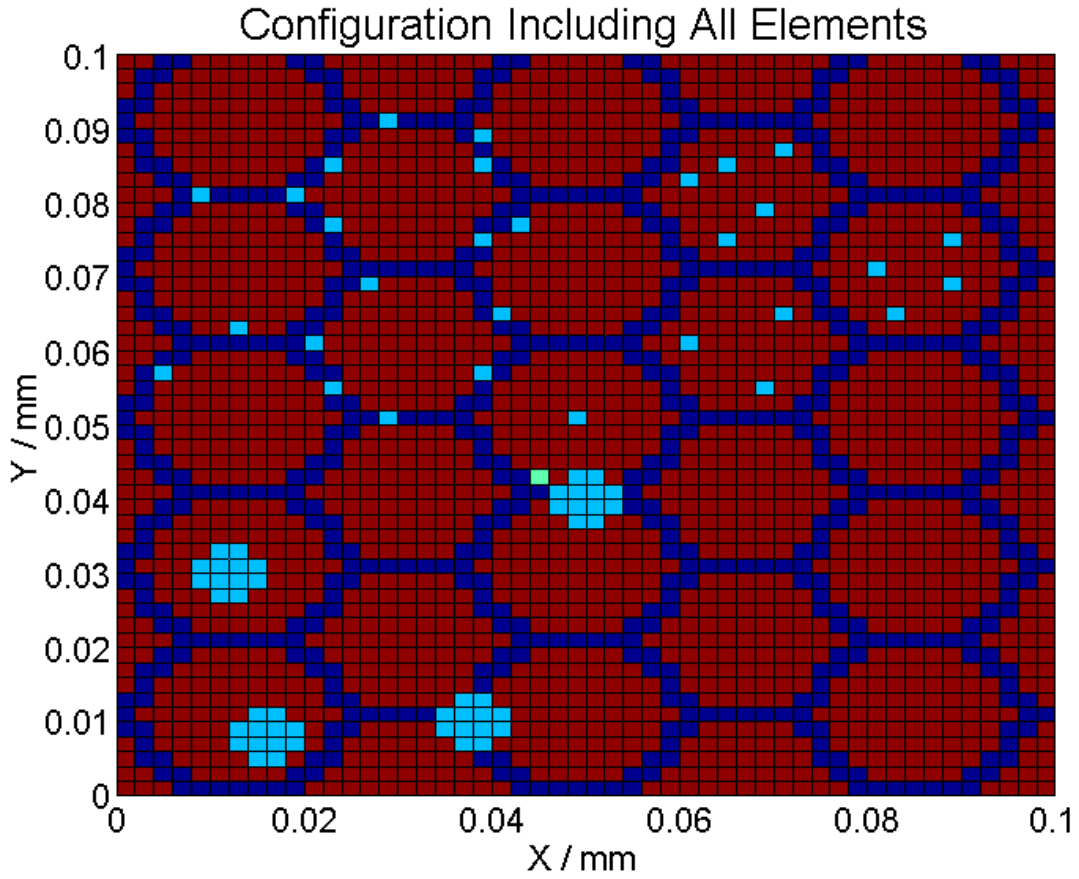

Fig. 118: Configuration for a structure consisting of hexagonal grains surrounded by grain boundaries (dark blue), small and large precipitates (light blue) and a homogeneous bulk material (red).

The result of the simulation in terms of creep strain is shown in Fig. 119. The different influences on creep behaviour can clearly be seen. Within the grains, the creep strain is pronounced at the grain boundaries oriented normally to the applied stress for all parts of the depicted microstructure. Thus, as expected for Nabarro Herring creep, these regions are the most important to be considered in analysing creep straining. Grain boundaries with other orientations versus the applied stress only are of minor importance during plastic straining. The influence of precipitates is determined by their size and exact position within the grain structure.

Large, extended precipitates clearly increase the inhomogeneities within a grain. Both, an increase and a decrease in the resulting creep strain can be observed. This effect is dependent on the orientation. Especially near precipitate-bulk transitions, which are oriented parallel to

the applied stress, a decrease in creep strain can be observed, whereas the creep zones near boundaries and triple points are enlarged clearly.

The small precipitates within the bulk material have a distinct, but small influence on creep straining. They increase the local stress concentrations in the local neighbourhood is only of minor extent compared to the stress increase caused by grain boundaries. In contrast, small precipitates located on the grain boundaries can increase existing concentrations significantly. This especially holds true for precipitates located in the vicinity of triple junctions. With this combination of two microstructural elements, the most pronounced local creep straining in the presented results have been calculated.

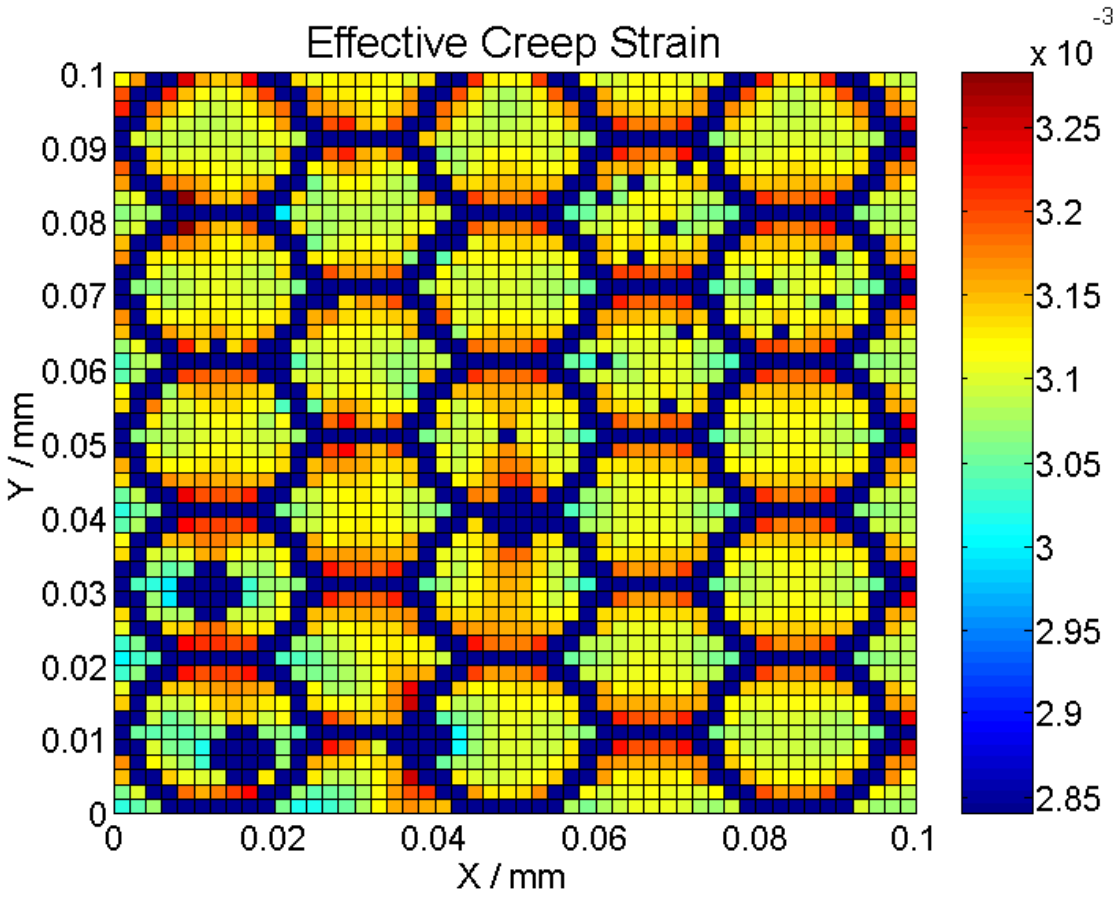

Fig. 119: Effective creep stain distribution for a structure consisting of hexagonal grain and precipitates exposed to a creep load after t = 6 000 h.

This simulation shows that the microstructural components and their actual configuration have major influence in diffusional creep and have to be studied extensively to model creep behaviour on a sound basis.

5.5 Conclusion

The results of the calculations presented in this chapter demonstrate that microstructural elements, such as grain boundaries, triple points and precipitates, are causing a spatially inhomogeneous internal stress distribution. These stress distributions, including stress singularities etc., can be further influenced by specific arrangements of some of these elements, e.g. as combination of hard particles, grain boundaries or triple points. Especially triple junctions of grain boundaries play an important role concerning stress inhomogeneities. These stress singularities within an otherwise homogeneous bulk material are further influenced by particles. The inhomogeneous stress distribution is levelled out by creep in the further evolution of the microstructure, which leads to a distinct, heterogeneous pattern of creep strain. Especially, on distinct sites of such a microstructure, this mechanism can lead to a pronounced local accumulation of creep strain.

6 Summary

In this work the local creep behaviour of a polycrystalline material is investigated. To do so, a spatially resolved model to simulate local creep deformation within a microstructure is presented.

This model is realized using the Finite Element Method as mathematical framework. The structure is discretisized in space using 2D quadrilateral elements, all necessary integrations are done by Gaussian quadrature, the solution of the system of equations is performed numerically by MATLAB routines.

The numerical algorithm to calculate creep deformation and stresses is implemented directly into the Finite Element framework. It is performed in discrete time steps and proves to be robust and efficient. The general form of the constitutive equation used here makes the model flexible and adaptable. A description of the code implementation is given as well.

The microstructure is introduced in terms of a spatially resolved structure where the microstructural components are comprised as distinct, separated elements that include bulk material, grain boundaries, triple points and small and large precipitates. All these constituents are described by different properties such as elastic modulus, poisons ratio and diffusion coefficients. Of the different physical mechanism operating during creep loading, Nabarro Herring creep, which is a creep mechanism operated by diffusion of vacancies, has been chosen to be studied in this work.

The results of the calculations demonstrate that the microstructural elements are causing a spatially inhomogeneous internal stress distribution. These stress distributions can be further influenced by specific arrangements of some of these components, e.g. as combination of hard particles, grain boundaries or triple points.

Due to the presence of grain boundaries, the internal stress distribution in an otherwise homogeneous grain will show a distinct, non-homogeneous pattern. Especially triple junctions of grain boundaries are a pronounced source for stress inhomogeneities, as is shown with the presented calculations. Thus, triple points play an important role for creep phenomena. The

resulting stress singularities are further influenced by hard particles. Depending on their position, these particles can further influence the maximum stress concentrations.

The inhomogeneous internal stress distribution, which acts as driving force for creep deformation, results in an inhomogeneous local creep deformation. The initial stress distribution is levelled out by creep straining, resulting in a local stress relaxation. This trend leads to a pronounced local accumulation of creep strain. These results show that creep can not be regarded solely as a macroscopic phenomenon, which can be comprised by mean values and statistical approaches, but has to be handled on a local resolved basis as is done in the present work.

Bibliography

[1] J. Čadek. Creep in Metallic Materials. Elsevier, 1988.

[2] H.J. Frost, M.F. Ashby. Deformation-Mechanism Maps: The Plasticity and Creep of Metals and Ceramics. Oxford: Pergamon Press, 1982.

[3] H. Mehrer (Editor). Landolt-Börnstein - Numerical Data and Functional Relationships in Science and Technology, Vol. 26, Diffusion in Solid Metals and Alloys. Berlin: Springer, 1990.

[4] J. Crank. The Mathematics of Diffusion. Oxford Science Publications, 1975.

[5] C. Herring. Diffusional Viscosity of a Polycrystalline Solid. Journal of Applied Physics Vol. 21, pp. 437-445, 1950.

[6] K.G.F. Janssens, D. Raabe, E. Kozeschnik, M.A. Miodownik, B. Nestler. Computational Materials Engineering. An Introduction to Microstructure Evolution. Elsevier, 2007.

[7] H. Mehrer. Diffusion in Solids. Fundamentals, Methods, Materials, Diffusion-Controlled Processes. Springer, 2007.

[8] J. Svoboda, F.D. Fischer, P. Fratzl. Diffusion and creep in multi-component alloys with non-ideal sources and sinks for vacancies. Acta Materialia, Vol. 54, pp. 3043–3053, 2006.

[9] K. Ralls, T. Courtney, J. Wulff. Introduction to Materials Science and Engineering. Wiley, 1976.

[10] A.G. Guy. Essentials of Materials Science. New York: McGraw-Hill, 1976.

[11] H. Riedel. Fracture at High Temperatures. Springer, 1987.

[12] M.E. Glicksman. Diffusion in solids.New York: Wiley, 2000.

[13] F.R.N. Nabarro. Deformation of Crystals by the Motion of Single Ions. Strength of Solids, pp. 75-90. London: The Physical Society, 1948.

[14] R.L. Coble. A Model for Boundary Diffusion Controlled Creep in Polycrystalline Materials. Journal of Applied Physics, Vol. 34(6), pp. 1679-1682. 1963.

[15] Luboš Kloc, Václav Skienička, Jiří Ventruba. Comparison of low stress creep properties of ferritic and austenitic creep resistant steels. Materials Science and Engineering A, Vol. 319–321, pp. 774–778, 2001.

[16] A. Inoue, H. Nitta, Y. Iijima. Grain boundary self-diffusion in high purity iron. Acta Materialia, Vol. 55, pp. 5910-5916, 2007.

[17] C. Leymonie, P. Lacombe. Les memoires scientifiques de la revue de metallurgie, pp. 57-285, 1960.

[18] V.T. Borisov, V.M. Golikov, G.V. Scherbedinskiy. Phys. Met. Metallogr. Vol. 17, pp 80, 1964.

[19] D.W. James, G.M. Leak. Grain boundary diffusion of iron, cobalt and nickel in alpha-iron and of iron in gamma-iron. Philosophical Magazine Vol. 12(17), pp. 491-503, 1965.

[20] J. Bernardini, P. Gas, E.D. Hondros, M.P. Seah. The Role of Solute Segregation in Grain Boundary Diffusion. Proceedings of the Royal Society A, Vol. 379(1776), pp. 159-178, 1982.

[21] H. Hänsel, L. Stratmann, H. Keller, H.J. Grabke. Effects of the grain boundary segregants P, S, C and N on the grain boundary self-diffusivity in α-iron. Acta Metallurgica, Vol. 33(4), pp. 659-665, 1985.

[22] Y. Shima, Y. Ishikawa, H. Nitta, Y. Yamazaki, K. Mimura, M. Isshiki, Y. Iijima. Self-Diffusion along Dislocations in Ultra High Purity Iron. Materials Transactions, Vol. 43(2), pp. 173-177, 2002.

[23] B. Burton, G.L. Reynolds. In defense of diffusional creep. Materials Science and Engineering A Vol. 191, pp. 135-141, 1995.

[24] V. Yamakov, D. Wolf, S.R. Phillpot, H. Gleiter. Grain-boundary diffusion creep in nanocrystalline palladium by molecular-dynamics simulation. Acta Materialia Vol. 50, pp. 61–73. 2002.

[25] F.R.N. Nabarro. Creep at Very Low Rates. Metallurgical and Materials Transactions A. Vol. 33A, pp. 213-218, 2002.

[26] S.S. Sahay, G.S. Murty. Uncertainty in separating the strain contributions of sliding and diffusion in diffusional creep. Scripta Materialia Vol. 44 pp. 841–845, 2001.

[27] S.S. Sahay, G.S. Murty. On the contributions of diffusion and sliding to the overall strain of diffusional creep. Journal of Nuclear Materials, Vol. 195, pp. 320-323, 1992.

[28] D.M. Owen, T.G. Langdon. Low stress creep behavior: an examination of Nabarro-Herring and Harper-Dorn creep. Materials Science and Engineering A, Vol. 216, pp. 20-29, 1996.

[29] M.F. Ashby. On interface-reaction control of Nabarro-Herring creep and sintering. Scripta Metallurgica, Vol 3(11), pp. 837-842, 1969.

[30] D.A. Smith, V. Vitek, R.C. Pond. Computer simulation of symmetrical high angle boundaries in aluminium. Acta Metallurgica, Vol. 25(5), pp. 475-483, 1977.

[31] H. Gleiter. Grain boundaries as point defect sources or sinks-Diffusional creep. Acta Metallurgica, Vol. 27(2), pp. 187-192, 1979.

[32] E. Arzt, M.F. Ashby, R.A. Verrall. Interface controlled diffusional creep. Acta Metallurgica, Vol. 31(12), pp. 1977-1989, 1983.

[33] K.A. Peterson, I. Dutta, M.W. Chen. Diffusionally accommodated interfacial sliding in metalsilicon systems. Acta Materialia, Vol. 51, pp. 2831–2846, 2003.

[34] K. Kuchařová, S.J. Zhu, J. Čadek. Creep in copper dispersion strengthened with alumina particles. Materials Science and Engineering A, Vol. 348, pp. 170-179, 2003.

[35] B. Cai, Q.P. Kong, L. Lu, K. Lu. Low temperature creep of nanocrystalline pure copper. Materials Science and Engineering A, Vol. 286, pp. 188–192, 2000.

[36] E. Arzt. Size effects in materials due to microstructural and dimensional constraints: a comparative review. Acta Materialia, Vol. 46(16), pp. 5611-5626, 1998.

[37] B. Burton. Interface reaction controlled diffusional creep: A consideration of grain boundary dislocation climb sources. Materials Science and Engineering, Vol. 10, pp. 9-14, 1972.

[38] M.J. Roddy, W.R. Cannon, G. Skandan, H. Hahn. Creep behavior of nanocrystalline monoclinic ZrO2. Journal of the European Ceramic Society, Vol. 22, pp. 2657–2662, 2002.

[39] J. Markmann, P. Bunzel, H. Rösner, K.W. Liu, K.A. Padmanabhan, R. Birringer, H. Gleiter, J. Weissmüller. Microstructure evolution during rolling of inert-gas condensed palladium. Scripta Materialia, Vol. 49, pp. 637–644, 2003.

[40] J. Fiala, J. Novotný, J. Čadek. Coble and Harper-Dorn creep in iron at homologous temperatures of 0.40-0.54. Materials Science and Engineering, Vol. 60(3), pp. 195-206, 1983.

[41] B. Burton, G.L. Reynolds. The diffusional creep of uranium dioxide: its limitation by interfacial processes. Acta Metallurgica, Vol. 21, pp. 1073-1078, 1973.

[42] J. Wolfenstine, O.A. Ruano, J. Wadsworth, O.D. Sherby. Refutation of the relationship between denuded zones and diffusional creep. Scripta Metallurgica et Materialia, Vol. 29(4), pp. 515-520, 1993.

[43] K.R. McNee, G.W. Greenwood, H. Jones. Observation and interpretation of some microstructural features of low stress creep. Scripta Materialia, Vol. 47, pp. 619–623, 2002.

[44] O.A. Ruano, O.D. Sherby, J. Wadsworth, J. Wolfenstine. Rebuttal to "In defense of diffusional creep". Materials Science and Engineering A, Vol. 211, pp. 66-71, 1996.

[45] K.R. McNee, G.W. Greenwood, H. Jones. Microstructural evidence for diffusional creep in copper using atomic force microscopy. Scripta materialia, Vol. 44, pp. 351–357, 2001.

[46] J.Harper, J.E. Dorn. Viscous creep of aluminum near its melting temperature. Acta metallurgica, Vol. 5, pp. 654-665, 1957.

[47] M.E. Kassner, M.T. Pérez-Prado. Fundamentals of creep in metals and alloys. Elsevier, 2004.

[48] M.E. Kassner, P. Kumar, W. Blum. Harper–Dorn creep. International Journal of Plasticity, Vol. 23, pp. 980–1000, 2007.

[49] A.J. Ardell. Harper-Dorn creep – Predictions of the dislocation network theory of high temperature deformation. Acta Metallurgica, Vol. 45, pp. 2971-2981, 1997.

[50] Y.C.Cheng, M. Chauhan, F.A. Mohamed. Uncovering the Mystery of Harper–Dorn Creep in Metals. Metallurgical and Materials Transactions A, Vol. 40A, pp. 80 – 90, 2009.

[51] W. Blum, W. Maier. Harper-Dorn Creep - a Myth? Physica Status Solidi (a), Vol. 171, pp. 467-474, 1999.

[52] P. Kumar, M.E. Kassner, T.G. Langdon. The role of Harper–Dorn creep at high temperatures and very low stresses. Journal of Materials Science, Vol. 43, pp. 4801–4810, 2008.

[53] P. Kumara, M.E. Kassner,W. Blum, P. Eisenlohrd, T.G. Langdon. New observations on high-temperature creep at very low stresses. Materials Science and Engineering A, Vol. 510–511, pp. 20–24, 2009.

[54] J.R. Mayeur, D.L. McDowell, R.W. Neu. Crystal plasticity simulations of fretting of Ti-6Al-4V in partial slip regime considering effects of texture. Computational Materials Science, Vol. 41, pp. 356–365, 2008.

[55] R.W. Cahn, P. Haasen. Physical Metallurgy. Amsterdam, 1983.

[56] M. Zhang, J. Zhang, D.L. McDowell. Microstructure-based crystal plasticity modeling of cyclic deformation of Ti–6Al–4V. International Journal of Plasticity, Vol. 23, pp. 1328–1348, 2007.

[57] D. McLean. Resistance to hot deformation. Transactions of the Metallurgical Society of AIME, Vol. 242, pp. 1193-&, 1968.

[58] R. Gasca-Neri, W.D. Nix. A model for the mobile dislocation density. Acta Metallurgica, Vol. 22, pp. 257 – 264, 1974.

[59] S. Takeuchi, A.S. Argon. Steady-state creep of single-phase crystalline matter at high temperature. Journal of Materials Science, Vol. 11, pp. 1542 – 1566, 1976.

[60] W.D. Nix, B.Ilschner. Mechanisms controlling creep of single phase metals and alloys. Proceedings of the Fifth International Conference Strength of Metals and Alloys, Vol. 3, pp. 1503 – 1530, 1980.

[61] M.M. Myshlyaev, D. Caillard, J.L. Martin. Creep at intermediate temperatures: An in situ study of the evolution of the cell boundaries in the high voltage electron microscope. Scripta Metallurgica, Vol. 12, pp. 157-160, 1978.

[62] T.G. Nieh, J. Wadsworth, O.D. Sherby. Superplastie Behavior of Metallic, Ceramic and lntermetallic Materials. Cambridge, 1995.

[63] A. Arieli, A.K. Mukherjee. A model for the rate-controlling mechanism in superplasticity. Materials Science and Engineering, Vol. 45, pp. 61-70, 1980.

[64] R.C. Gifkins. Grain-boundary sliding and its accommodation during creep and superplasticity. Metallurgical Transactions A, Vol. 7A, pp. 1225-1232, 1976.

[65] H. Fukuyo, H.C. Tsai, T. Oyama, O.D. Sherby. Superplasticity and Newtonian-viscous flow in fine-grained class I solid solution alloys. ISIJ International, Vol. 31, pp. 76-85, 1991.

[66] D. Raabe. Computational materials science - The simulation of materials, microstructures and properties. Weinheim, 1998.

[67] B. Sonderegger. Charakterisierung der Substruktur in modernen Kraftwerkswerkstoffen mittels der EBSD Methode. PhD Thesis, TU Graz, 2005.

[68]K.J. Kozaczek, A. Sinharoy, C.O. Ruud, A.R. McIlree. Modeling of stresses at grain boundaries with respect to occurrence of stress corrosion cracking. Conference: Improving the understanding and control of corrosion on the secondary side of steam generators. Airlie, 1995.

[69] F. Abe, T.-U. Kern, R. Viswanathan. Creep-resistant steels. Woodhead Publishing, Cambridge, 2008.

[70] J. Svoboda; E. Gamsjäger; F.D. Fischer. Relaxation of the elastic strain energy of misfitting inclusions due to diffusion of vacancies. Philosophical Magazine Letters, Vol. 85, pp. 473 – 479, 2005.

[71] J. Svoboda, E. Gamsjäger, F.D. Fischer. Influence of diffusional stress relaxation on growth of stoichiometric precipitates in binary systems. Acta Materialia, Vol. 54, pp. 4575–4581, 2006.

[72] P. Hofer. Mikrostrukturelle Analyse als Basis für die Entwicklung neuer Kraftwerkswerkstoffe am Beispiel von G-X12 CrMoWVNbN 10-1-1. PhD Thesis, TU Graz, 1999.

[73] H. Chilukuru, K. Durst, S. Wadekar, M. Schwienheer, A. Scholz, C. Berger, K.H. Mayer, W. Blum. Coarsening of precipitates and degradation of creep resistance in tempered martensite steels. Materials Science and Engineering A, Vol. 510-511, pp. 81-87, 2009.

[74] K. Janssens, D. Raabe, E. Kozeschnik, M. Miodownik, B. Nestler. Computational Materials Engineering - An Introduction to Microstructure Evolution. Academic Press, 2007.

[75] T.G. Langdon. Creep at Low Stresses: An Evaluation of Diffusion Creep and Harper–Dorn Creep as Viable Creep Mechanisms. Metallurgical and Materials Transactions A, Vol. 33A, pp. 249-259, 2002.

[76] F.R.N Nabarro. The mechanism of Harper-Dorn creep. Acta Metallurgica, Vol. 37, pp. 2217-2222, 1989.

[77] .N. Wang. On the transition from power law creep to Harper-Dorn creep. Scripta Metallurgica et Materialia, Vol. 29, pp. 733-736, 1993.

[78] J.N. Wang. Dependence of dislocation density in Harper-Dorn creep on the peierls stress. Scripta Metallurgica et Materialia, Vol. pp. 1505-1508, 1993.

[79] G. Schöck. The peierls stress and the flow stress in Fcc metals. Scripta Metallurgica et Materialia, Vol. 30, pp. 611-613, 1994.

[80] J.N. Wang, T.G. Langdon. An evaluation of the rate-controlling flow process in Harper-Dorn creep. Acta Metallurgica et Materialia, Vol. 42, pp. 2487-2492, 1994.

[81] J.N. Wang. A microphysical model of Harper-Dorn creep. Acta Materialia, Vol. 44, pp. 855-862, 1996.

[82] J. Weertman. Dislocation climb theory of steady-state creep. ASM Transactions, Vol. 61, pp. 681-&, 1968.

[83] J. Weertman. Steady-state creep through dislocation climb. Journal of Applied Physics, Vol. 28, pp. 362-364, 1957.

[84] J. Weertman, J.R. Weertman. In: Physical Metallurgy, Editor: R.W.Cahn, Amsterdam, p. 736, 1965.

[85] J. Weertman. In: Rate Processes in Plastic Deformation of Materials. Editor: J.C.M.L. Mukherjee. ASM, Ohio, pp. 315-336, 1975.

[86] L.I. Ivanov, V.A. Yanushkevich. High temperature mechanism of steady state creep in BCC metals: creep of zirconium. The Physics of Metals and Metallography (Fizika Metallov i Metallovedenie), Vol. 17, pp. 112-193, 1964.

[87] W. Blum. Role of dislocation annihilation during steady-state deformation. Physica Status Solidi, Vol. 45, pp. 561-571, 1971.

[88] J. Weertman. In: Creep and Fracture of Engineering Materials and Structures. Editors: B. Wilshire, D.R.J. Owen, Swansea, 1984.

[89] F.R.N. Nabarro. Steady-state diffusional creep. Philosophical Magazine, Vol. 16, pp. 231-&, 1967.

[90] N.F. Mott. In: Creep and Fracture of Metals at High Temperatures. HMSO, London, pp. 21-&, 1956.

[91] L. Raymond, J.E. Dorn. Recovery of creep-resistant substructures. Transactions of The Metallurgical Society of AIME, Vol. 230, pp. 560-&, 1964.

[92] C.R. Barrett, W.D. Nix. A model for steady state creep based on motion of jogged screw dislocations. Acta Metallurgica, Vol.13, pp. 1247-&, 1965.

[93] J. Friedel. Dislocations. Pergamon Press, Oxford, 1964.

[94] S. Takeuchi, A.S. Argon. Steady-state creep of alloys due to viscous motion of dislocations. Acta Metallurgica, Vol. 24, pp. 883-889, 1976.

[95] L.M. Brown, R.K. Ham. In: Strengthening methods in crystals. Editors: A. Kelly and R. B. Nicholson, Elsevier, 1971.

[96] R.S.W. Shewfelt, L.M. Brown. High-temperature strength of dispersion-hardened single-crystals .2. Theory. Philosophical Magazine, Vol. 35, pp. 945-962, 1977.

[97] R.A. Stevens, P.E.J. Flewitt. The dependence of creep rate on microstructure in a gamma'-strengthened super-alloy. Acta Metallurgica, Vol. 29, pp. 867-882, 1981.

[98] D. Raabe, R.C. Becker. Coupling of a crystal plasticity finite-element model with a probabilistic cellular automaton for simulating primary static recrystallization in aluminium. Modelling and Simulation in Materials Science and Engineering, Vol. 8, pp. 445–462, 2000.

[99] D.L. McDowell. Viscoplasticity of heterogeneous metallic materials. Materials Science and Engineering R, Vol. 62, pp. 67–123, 2008.

[100] J.R. Mayeur, D.L. McDowell. A three-dimensional crystal plasticity model for duplex Ti–6Al–4V. International Journal of Plasticity, Vol. 23, pp. 1457–1485, 2007.

[101] A. Ma, F. Roters, D. Raabe. A dislocation density based constitutive law for BCC materials in crystal plasticity FEM. Computational Materials Science, Vol. 39, pp. 91–95, 2007.

[102] A. Ma, F. Roters, D. Raabe. On the consideration of interactions between dislocations and grain boundaries in crystal plasticity finite element modeling – Theory, experiments, and simulations. Acta Materialia, Vol. 54, pp. 2181–2194, 2006.

[103] A. Ma, F. Roters, D. Raabe. A dislocation density based constitutive model for crystal plasticity FEM including geometrically necessary dislocations. Acta Materialia, Vol. 54, pp. 2169–2179, 2006.

[104] K.-S. Cheong, E.P. Busso. Discrete dislocation density modelling of single phase FCC polycrystal aggregates. Acta Materialia, Vol. 52, pp. 5665–5675, 2004.

[105] K.J. Bathe. Finite Element Procedures. Prentice Hall, New York, 1996..

[106] O.C Zienkiewicz, R.L. Taylor. The Finite Element Method. McGraw-Hill, 1991.

[107] Y. Wei, A.F. Bower, H. Gao. Recoverable creep deformation and transient local stress concentration due to heterogeneous grain-boundary diffusion and sliding in polycrystalline solids. Journal of the Mechanics and Physics of Solids, Vol. 56, pp. 1460–1483, 2008.

[108] H.S. Kim, M.B. Bush. The effects of grain size and porosity on the elastic modulus of nanocrystalline materials. NanoStructured Materials, Vol. 11, pp. 361–367, 1999.

[109] J.E. Carsley, J. Ning, W.W. Milligan, S.A. Hackney, E.C. Aifantis. A simple, mixtures-based model for the grain size dependence of strength in nanophase metals. NanoStructured Materials, Vol. 5, pp. 441-448, 1995.

[110] C.A. Schuh, T.C. Hufnagel, U. Ramamurty. Mechanical behavior of amorphous alloys. Acta Materialia, Vol. 55, pp. 4067–4109, 2007.

[111] D. Weaire, M.F. Ashby, J. Logan, M.J. Weins. Acta Metallurgica, Vol. 19, pp. 779, 1971.

[112] H.S. Kim, Y. Estrin, M.B. Bush. Plastic deformation behaviour of fine-grained materials. Acta Materialia, Vol. 48, pp. 493-504, 2000.

[113] V. Sklenička, K. Kuchařová, M. Svoboda, L. Kloc, J. Buršík, A. Kroupa. Long-term creep behavior of 9–12%Cr power plant steels. Materials Characterization, Vol. 51, pp. 35– 48, 2003.

[114] D. Fuks, J. Pelleg, S.N. Rashkeev, S. Dorfman. Anomalies of temperature dependences of the elastic moduli of steels of the austenitic and transition classes. Zeitschrift für Physik B, 1990.

[115] G. Totten (Edt.). Handbook of residual stress and deformation of steel. Hitchin, Herts, 2002.

[116] P. Weinert. Modellierung des Kriechens von ferritisch/martensitischen 9-12% Cr-Stählen auf mikrostruktureller Basis. PhD Thesis, TU Graz, 2001.

[117] R.G. Whirley, G.A. Henshall. Creep deformation structural analysis using an efficient numerical algorithm. International Journal for Numerical Methods in Engineering, Vol. 35, pp. 1427 – 1442, 1992.

[118] *in memoriam*: Marion Kögl. Total synthesis and configurational assignment of pasteurestin A and B. PhD Thesis, Universität Wien, 2008.